TARGETABLE MULTI-DRUG NANOPARTICLES FOR TREATMENT OF GLIOBLASTOMA WITH NEUROIMAGING ASSESSMENT

A Thesis

Submitted to the Faculty

of

Purdue University

by

Shelby B. Smiley

In Partial Fulfillment of the

Requirements for the Degree

of

Master of Science in Biomedical Engineering

May 2020

Purdue University

Indianapolis, Indiana

THE PURDUE UNIVERSITY GRADUATE SCHOOL
STATEMENT OF COMMITTEE APPROVAL

Dr. Chien-Chi Lin, Co-Chair

Department of Biomedical Engineering

Dr. Michael Veronesi, Co-Chair

Department of Radiology and Imaging Sciences

Dr. Mangilal Agarwal

Department of Mechanical and Energy Engineering

Approved by:

Dr. Julie Ji

Head of the Graduate Program

ACKNOWLEDGMENTS

I would like to thank my advisor Dr. Michael Veronesi for his continuous support throughout my graduate career. I appreciate the many professional and technical skills I have obtained working with him throughout this time.

I would also like to thank Dr. Sudip Das from Butler University. I am so thankful for the amount of times you made yourself available at any day of the week for helping me troubleshoot and help with experimental design. Thank you for your help with advancing my understanding of pharmaceutical drugs and nanoparticle formulations.

Thank you to my graduate committee Dr. Chien-Chi Lin and Dr. Mangilal Agarwal for their time spent on my thesis.

Thank you to Integrated Nanosystems Development Institute (INDI) for their use of instrumentation.

Thank you to Dr. Karen Pollok, Dr. Harlan Shannon, Barbara Bailey and the Indiana University Simon Cancer Center In Vivo Therapeutics Core for providing primary cells. Thank you Barbara for help with in vitro techniques and thank you Harlan for the time spent on teaching me the principles of combination drug analysis.

Thank you to my mentors, Dr. Yeonhee Yun and Dr. Mosa Alhamami, who were always available for research advice when needed. I cherish your hard work to support me as well as the friendships we've developed in our lab.

Thank you to Dr. Gary Hutchins and the Radiology and Imaging Sciences faculty for supporting me and allowing me to join your department and work alongside you.

A special thanks to Julia Payton for her help working in the Department of Radiology. Thank you to Sherry Clemens for her help with thesis formatting and guidance during the graduate process.

Finally, thank you to my parents and soon to be husband, Kendall Miedema. Completing this thesis could not have been achieved without your love and support.

TABLE OF CONTENTS

Page

Page

LIST OF TABLES

LIST OF FIGURES

Figure Page

Figure Page

LIST OF SYMBOLS

A	Adenine
β	Beta
β^+	Positron
C	Cytosine
$^\circ C$	Celsius
CI	Combination index
Ci	Curie
cP	Centipoise
D	Dose of drug to produce specific Fa
D_m	Median-effect dose
eV	Electron volt
Fa	Fraction affected
Fu	Fraction unaffected
G	Guanine
g	g-force
Gy	Gray
G_0	Resting phase of cell cycle
G_2	Period of cell cycle between DNA synthesis and prophase
IC_{50}	Half maximal inhibitory concentration
kDa	kilodalton
m	Shape of dose response curve
M	Metaphase
mV	Millivolt
NH_2	Amino group

o/w	Oil in water
r	Linear correllation coefficient
rcf	Relative centrifugal force
rpm	Revolutions per minute
U	Uracil
V	Volts
$w/o/w$	Water in oil in water
^{89}Zr	Zirconium-89
$^{89}Zr(HPO_4)_2$	Zirconium phosphate

LIST OF ABBREVIATIONS

ACN	Acetonitrile
AIC	5-aminoimidazole-4-carboxamide
BBB	Blood brain barrier
CBTRUS	Central Brain Tumor Registry of the United States
CO_2	Carbon dioxide
CSC	Cancer stem cell
CT	Computed tomography
DCM	Dichloromethane
DDR	DNA damage response
DFO	Deferoxamine
DFO-Bz-NCS	Deferoxamine benzyl isothiocyanate
DFOM	Deferoxamine mesylate
DL%	Drug loading percentage
DLS	Dynamic light scattering
DMEM	Dulbecco's Modified Eagle's Medium
DMSO	Dimethyl sulfoxide
DNA	Deoxyribonucleic acid
DSPE	Distearoylphosphatidyl ethanolamine
EDC	1-ethyl-3-(3-dimethyl aminopropyl) carbodiimide
EE%	Encapsulation efficiency
EMSA	Electrophoretic mobility shift assay
FACS	Fluorescence-activated cell sorting
FBS	Fetal bovine serum
FCS	Fluorescence correlation spectroscopy

FDA	Food and Drug Administration
GFAP	Glial fibrillary acidic protein
GBM	Glioblastoma
HCl	Hydrochloric acid
HPLC	High pressure liquid chromatography
IDH	Isocitrate dehydrogenase
INDD	Intranasal drug delivery
MDM2	Mouse double minute 2
MGMT	O^6-methylguanine methyltransferase
MRI	Magnetic resonance imaging
MTIC	5-(3-methyltriazen-1-yl) imidazole-4-carboxamide
NHS	N-hydroxysuccinimide
NP	Nanoparticle
PBS	Phosphate buffered saline
PCL	Polycaprolactone
PDI	Polydispersity index
PEG	Polyethylene glycol
PET	Positron emission tomography
PEO	Poly(ethylene oxide)
PGA	Polyglycolic acid
PLA	Polylactic acid
PLGA	Poly(lactic-*co*-glycolic) acid
PPO	Poly(propylene oxide)
PS	Polystyrene
PS-*b*-PEO	Poly(styrene-*b*-ethylene oxide)
PTX	Paclitaxel
PVA	Polyvinyl alcohol
RG7388	Idasanutlin
RNA	Ribonucleic acid

SEER	Surveillance Epidemiology and End Results
TAE	Tris-Acetate-EDTA
TEM	Transmission electron microscopy
TMZ	Temozolomide
VEGF	Vascular endothelial growth factor
WHO	World Health Organization

ABSTRACT

Smiley, Shelby B. M.S.B.M.E., Purdue University, May 2020. Targetable Multi-drug Nanoparticles for Treatment of Glioblastoma with Neuroimaging Assessment.
Major Professor: Michael C. Veronesi.

Glioblastoma (GBM) is a deadly, malignant brain tumor with a poor long-term prognosis. The current median survival is approximately fifteen to seventeen months with the standard of care therapy which includes surgery, radiation, and chemotherapy. An important factor contributing to recurrence of GBM is high resistance of GBM cancer stem cells (CSCs), for which a systemically delivered single drug approach will be unlikely to produce a viable cure. Therefore, multi-drug therapies are needed. Currently, only temozolomide (TMZ), which is a DNA alkylator, affects overall survival in GBM patients. CSCs regenerate rapidly and over-express a methyl transferase which overrides the DNA-alkylating mechanism of TMZ, leading to drug resistance. Idasanutlin (RG7388, R05503781) is a potent, selective MDM2 antagonist that additively kills GBM CSCs when combined with TMZ. By harnessing the strengths of nanotechnology, therapy can be combined with diagnostics in a truly theranostic manner for enhancing personalized medicine against GBM. The goal of this thesis was to develop a multi-drug therapy using multi-functional nanoparticles (NPs) that preferentially target the GBM CSC subpopulation and provide in vivo preclinical imaging capability. Polymer-micellar NPs composed of poly(styrene-*b*-ethylene oxide) (PS-*b*-PEO) and poly(lactic-*co*-glycolic) acid (PLGA) were developed investigating both single and double emulsion fabrication techniques as well as combinations of TMZ and RG7388. The NPs were covalently bound to a 15 base-pair CD133 aptamer in order to target a specific epitope on the CD133 antigen expressed on the surface of GBM CSC subpopulation. For theranostic functionality, the NPs were

also labelled with a positron emission tomography (PET) radiotracer, zirconium-89 (^{89}Zr). The NPs maintained a small size of less than 100 nm, a relatively neutral charge and exhibited the ability to produce a cytotoxic effect on CSCs. There was a slight increase in killing with the aptamer-bound NPs compared to those without a targeting agent. This work has provided a potentially therapeutic option for GBM specific for CSC targeting and future in vivo biodistribution studies.

1. INTRODUCTION

1.1 Glioblastoma overview

Gliomas are a group of primary, intrinsic brain tumors associated with limited therapy options and a poor long-term outcome. Glioblastoma (GBM) is the most malignant of the gliomas [1]. Affecting five to eight people per 100,000, GBM is one of the most common brain tumors [2] [3]. GBM is resistant to therapy largely because of an infiltrative nature and large genetic heterogeneity including multiple mutations. In addition, recurrence is contributed by a self-renewing population of cancer stem cells (CSCs) [4]. Development of new GBM therapies is an important area of research given the lack of progress for the past fifteen years and because of the profound impact of the disease on patients and society [1].

GBM affects approximately 14,000 people per year in the United States with a median age of sixty-four years old [3] [5]. GBM affects men slightly more than women according to the National Database of Central Brain Tumor Registry of the United States (CBTRUS) [6]. A study published in 2018 from the National Cancer Institute's Surveillance Epidemiology and End Results (SEER) determined that out of the 3,473 patients with first time diagnosis of GBM, 83.2% were White non-Hispanic [7]. It was also concluded that there was no statistical difference between the racial groups tested and three-year overall survival time [7].

Like many cancers, GBM results in high cost for the patient and the physicians and researchers working to treat the disease. Current treatments involve expensive technology and frequent hospital visits for the patient. The direct cost for a patient with GBM is estimated to be approximately $8,500 a month [8]. However, the total GBM market cost distributed equally across the United States, Europe, Asia, and

the rest of the world was approximately $465 million in 2016 and is expected to reach $1 billion in 2025 [8].

The presenting symptoms for GBM are relatively nonspecific and are often misdiagnosed initially. Severity and presence of symptoms correlate with the size of the tumor, location of the tumor, and whether eloquent areas of the brain are involved [3]. The most common presentation of a GBM is the presence of a focal, unilateral headache in about 50% of patients. [9]. Other presenting symptoms may include cognitive difficulties, ataxia, dizziness, and/or visual disturbance [10]. Seizures are another common presentation often presenting earlier on in the disease progression [11].

Once clinical exam findings suggest a central nervous system abnormality, including suspicion of a brain tumor, the primary initial workup includes contrast enhanced magnetic resonance imaging (MRI) of the brain. MRI is comprised of over 1,000 images and permits information such as tumor location, size, affect on normal structures and extent of associated edema. The average size of a GBM at diagnosis is approximately four-centimeters often indicating an advanced, incurable state once that large [10]. Most of the tumors diagnosed are located in the brain rather than the spinal cord and can occur in any location of the brain although they tend to involve the cerebral hemispheres including the frontal lobe (25%), temporal lobe (20%), parietal lobe (13%), and occipital lobe (3%) [3]. In addition to MRI, computed tomography (CT) may be used as a diagnostic tool to indicate a possible brain tumor [3]. However, CT lacks the high tissue contrast needed for complete characterization.

On histopathalogic diagnosis, specific markers are associated with the various cell types within a single glioma. Normal brain cells include neurons, glia, oligodendrocytes and immune cells, such as microglia. Glial cells provide essential nutrients and a supportive environment for the neuron. GBM is thought to arise from precursors to neurons and glia. Since GBM tumors are comprised of a heterogeneous number of cell types, clinicians look at a variety of markers during a biopsy for definitive diagnosis. For normal astrocytes, the most specific marker is the glial fibrillary acidic

protein (GFAP) [10]. Loss of the GFAP is a marker of increased malignancy of the tumor which aids in tumor grading. The World Health Organization (WHO) grades tumors from I-IV based on various histologic parameters [10]. GBM is a grade IV tumor, which is the most malignant tumor type, and has the highest degree of GFAP loss. Cell irregularity is due to polymorphism (genetic variation within a population), anaplasia (poor cellular differentiation), and anisokaryosis (larger than normal variation). A biopsy of the tumor can also provide additional morphologic information such as calcification, necrosis, and microcystic change [12] [13]. Other important markers involved in treating GBM include isocitrate dehydrogenase (IDH) and O^6-methylguanine methyltransferase (MGMT). Briefly, the presence of a mutated IDH corresponds to a longer survival time. In addition, it is typically found that patients will have better prognosis when the MGMT promoter is methylated [14]. These will be discussed later in further detail. Despite all that is known about the histology of gliomas, there is still often no clear consensus amongst pathologists for adult glioma diagnosis [15].

Cancer stem cells (CSCs) are believed to be an important contributing factor in tumor recurrence. CSCs are thought to originate from within the subventricular zone, which is located next to the ventricles of the brain. Glioma CSCs with certain driver mutations may be the cells from which GBM originates. These special mutated stem cells migrate away from the subventricular zones into the deeper brain regions and mutate further, leading to the development of a glioma [16]. CSCs create an extracellular tumor microenvironment that promotes GBM growth and maintains the aggressiveness of the tumor [17]. Over time, these cells can help the tumor adapt to conditions such as high lactic acidosis and hypoxia [17].

CSCs express several proteins that indicate stemness. For instance, CD133 (also known as AC133 and prominin-1) is a 97 kDa transmembrane glycoprotein whose function is not well known [18]. However, due to its typical location in plasma membrane protrusions and microvilli, it is thought to be involved in membrane organization [18]. CD133 is an important biomarker used to identify the CSC population

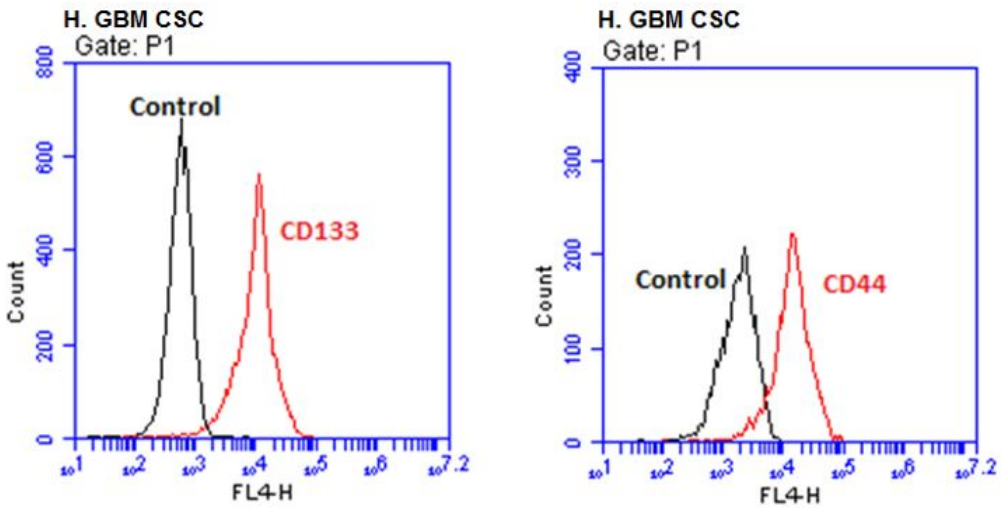

Fig. 1.1 Stem Cell Marker Profile. This figure represents data provided by Celprogen on the CSC markers used during their quality analysis. On the left shows the fluorescence achieved from selecting for CD133 while the right shows the fluorescence achieved when selecting for CD44.

within various tumor types. Data provided by Celprogen analyzed CSCs based on their presence of the CD133 marker alongside CD44 using flow cytommetry (Figure 1.1). CD44 is a cell glycoprotein responsible for cell interactions, migration, as well as adhesion. While this information does not present quantitative information regarding the amount of CD133 present on the CSCs, it does validate our purchase of CSCs.

However, not all tumor cells express the CD133 cell surface ligand [4]. The amount of CSCs containing the CD133 marker is also not consistent. One study analyzed three different primary GBM tumor cell lines and found the following percentages of CD133+ cells by analysis of flow cytommetry amongst the cultures: 10.2%, 69.7%, and 27.5% [19]. It is thought that the CD133+ cell population is one of select cell populations that are responsible for the tumor recurrence based on a study by Singh et al. who analyzed the ability of CD133+ and CD133- GBM CSCs to form tumors in mouse in vivo models [4]. As few as 100 CD133+ CSCs were sufficient to form tumors, yet up to 100,000 CD133- CSCs did not form tumors [4]. Therefore, a tumor

hierarchy likely exists within a single tumor that may start with the CD133+ cells for certain tumor types.

1.2 Glioblastoma standard of care

Treatment of GBM initially begins with surgical resection [12]. Complete resection is rarely attained because the highly infiltrative margins of the tumor are not visible on conventional MR imaging [3]. The decision of how much to resect is based on assessment of morbidity verses mortality when operating near eloquent areas. After surgery, radiation combined with chemotherapy are then initiated as soon as possible, but begins anywhere from one to four weeks later [3]. All patients are administered the chemotherapy drug temozolomide (TMZ) sold as Temodar with the chemical name 3-methyl-4-oxoimidazo[5,1-d][1,2,3,5]tetrazine-8-carboxamide] [20]. TMZ is given orally according to the Stupp regimen at a dose of 75 mg/m^2 daily for six weeks concurrently with radiation [21]. The focal radiation is given in fractions of 2 Gy for five days a week to total 60 Gy. After a one month rest, the patient is then started on six cycles of adjunvant TMZ at a dose of 150 to 200 mg/m^2 for five days every twenty-eight days [21]. TMZ was initially approved by the US Food and Drug Administration (FDA) for its treatment of adult GBM patients in 2005 and remains the first-line chemotherapy drug [20].

During or following therapy, the tumor initially responds, but often recurs. The standard of care is well-defined after the initial diagnosis, but after recurrence the standards are much less defined [22]. Serial MRI is conducted for continuous monitoring of the treatment course. Figure 1.2 represents a typical progression through treatment and diagnosis for a GBM patient [3]. MRI is the standard of care imaging modality; however, it is important to note that there are limitations because it can be difficult to differentiate between a rapidly progressing tumor and radiation-induced necrosis for many patients [23]. Differentiating tumor progression from treatment related change would benefit greatly from ongoing treatment decisions. Tumor re-

currence, from the subset population of CSCs, are difficult to differentiate from the abnormal inflammation induced by radiation damage [24].

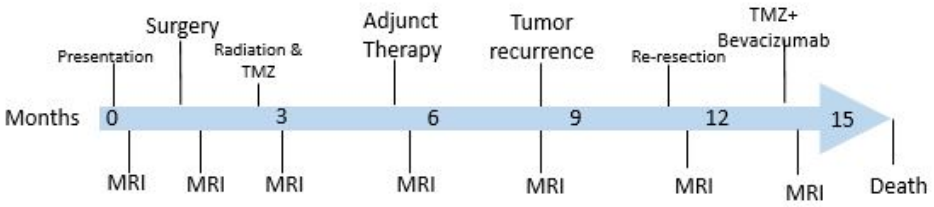

Fig. 1.2 Treatment tumor timeline. The above figure demonstrates a representative timeline of events a patient diagnosed with GBM would undergo during their course of treatment.

1.3 Temozolomide

TMZ is a deoxyribonucleic acid (DNA) alkylator, which nonspecifically methylates DNA [20]. There are two types of DNA alkylation. The first is monofunctional, which forms an adduct with DNA as it binds. The second is a biphasic process resulting in cross-linking of DNA [25]. TMZ is monofunctional and is rapidly converted into its active metabolite 5-(3-methyltriazen-1-yl) imidazole-4-carboxamide (MTIC) at physiological pH. MTIC is unstable at both low and high pH and rapidly converts to 5-amino-imidazole-4-carboxamide (AIC) and methyldiazonium ions [25].

Methyldiazonium ions work as electrophiles to alkylate the DNA in a monofunctional manner. TMZ methylates at N^3-adenine, N^7-guanine, and O^6-guanine sites, arresting the cell at the G_2/M phase [20]. As a DNA alkylator, TMZ not only arrests the cell cycle of tumor cells, but also non-specifically alkylates normal hematopoietic stem cells causing an unwanted side effect [5]. TMZ has poor serum stability with a short half-life of 1.8 hours, necessitating multiple doses [26]. Tighter control of the treatment regimen is required to prevent systemic side effects since TMZ is known to

cause lymphopenia, thrombocytopenia, and myelodysplasia [27]. Even though TMZ is used as the standard of care therapy, there are a variety of reasons why GBM becomes resistant to TMZ over time. First, GBM tumors have infiltrative properties which allow the tumor cells to extend deep into brain tissue often in a manner beyond that which can be seen with contrast enhanced imaging making complete surgical resection difficult [12]. Another challenge is the presence of the blood brain barrier (BBB) which is a highly restrictive barrier to protect the brain from the outside environment. The BBB comprise endothelial cells that form tight junctions to separate the brain from the circulatory system [17] [28]. The BBB likely restricts passage of 100% of large molecules and 98% of small molecules [17]. For TMZ delivery, 100% of the drug is absorbed with oral delivery, but only 17% of the administered drug makes it to the target location into the brain interstitium [29]. The BBB contains many *p*-glycoprotein pumps that act as gatekeepers to prevent entry of chemotherapy drugs by pumping TMZ back out of the brain [30]. Once TMZ converts to MTIC, the compound is rapidly degraded into its byproduts that facilitate DNA alkylation; therefore, the implementation of a delivery vehicle could potentially prolong the circulation time of TMZ to prevent alkylation prior to its delivery to the GBM tumor site.

Temozolomide resistance

TMZ in conjunction with radiation is usually successful initially, but the majority of GBM recurs in the first year [3] [17]. Within the genome of a GBM cell, the IDH gene leads to treatment resistance and the presence of wild-type IDH is a predictor of a poor response to a high dose of TMZ [31]. IDH is involved in many cellular processes including the citric acid cycle [32]. Patients with normal or wild-type IDH-1 correlate to a shorter survival, compared to those with IDH-1 mutations [15]. IDH-1 and IDH-2 both work to block stem cell differentiation and increase both vascular endothelial growth factor (VEGF) and hypoxia within the tumor environment [32].

All are contributing factors to TMZ resistance. In addition, IDH mutations are not present in the majority of GBM tumors and occur more commonly in grade II or III gliomas [33].

The high rate of GBM recurrence is in part due to the presence of a highly resistance population of GBM CSCs that lie within the tumor [34]. CSCs can readily generate both proliferating progenitor-like and differentiated tumor cells amid microenvironment cues; therefore, a small population of CSCs can potentially lead to complete regrowth of the tumor which adds to the high probability of recurrence and poor prognosis [35]. CSCs have a highly developed DNA damage response (DDR) system which can repair DNA damage caused by TMZ and other chemotherapeutic drugs and avoid apoptosis. From CSCs, resistance is thought to be due to either increased expression of MGMT, which can reverse the TMZ-induced methylation, or from reduced expression of tumor suppressor p53 as a result of high inhibition [20].

The MGMT gene encodes a DNA-repair protein to fix any DNA alkylation from TMZ [36]. When the promoter for this gene is methylated, it leads to a more positive prognosis because MGMT is unable to be over-produced [14]. CSCs typically have an over-expression of MGMT leading to rapid DNA repair after TMZ alkylation.

In addition, the tumor suppressor p53 is negatively regulated by mouse double minute 2 (MDM2). Over-expression of MDM2 inhibits p53's ability to reduce the tumor's oncogenic effects and send the cell down the apoptotic pathway [37].

1.3.1 Combination therapy

Because of high TMZ resistance as a result of the upregulated DDR system, TMZ itself is not a viable long term treatment option for GBM. Therefore, development of combination therapies are critical to treatment of GBM. For instance, an MDM2 inhibitor could provide the additional treatment to overcome TMZ resistance and eliminate residual CSCs. As discussed previously, MDM2 inhibits p53. Figure 1.3

represents a schematic showing that if MDM2 were inhibited by an antagonist, p53 would have the opportunity to accumulate and begin tumor suppression [38].

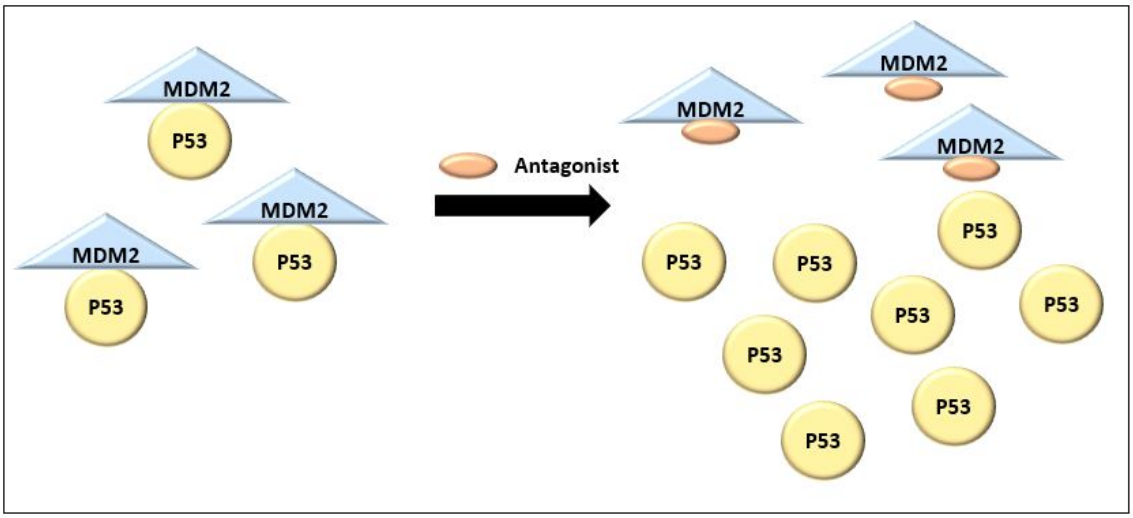

Fig. 1.3 Small-molecule inhibition of MDM2. An MDM2 antagonist can bind to MDM2 which will prevent the inhibition of p53. This would serve as an attempt to stabilize the p53 tumor suppression pathway.

Idasanutlin (RG7388, R05503781) is of the nutlin class of MDM2 inhibitors and possesses enhanced binding specificity, as well as more than 100-fold selectivity compared to its predecessor, RG7122 [39]. RG7388 has good systemic exposure, is metabolically stable in vivo, BBB permeable, and non-genotoxic [39] [40]. Preliminary data from Wang et al. has shown that both TMZ and RG7388 in combination produce a greater than expected, or a synergistic effect, in a primary GBM10 cell line and RG7388 is a viable treatment option in wild-type p53 GBM cell lines [37]. Therefore, TMZ and RG7388 provide a promising option for a combination therapy. Both of their mechanisms are outlined in Figure 1.4. As shown in Figure 1.4.A, TMZ enters the cell and converts to MTIC. The resulting methyldiazonium ions alkylate the DNA in the nucleus to send the cell towards apoptosis. Because of the increased DDR in the tumor, the cells become TMZ resistant. RG7388, as shown in Figure 1.4.B, also enters the cell and inhibits MDM2 in the nucleus. This results in the

accumulation of p53. P53 is involved in many cellular processes. Loss of p53 allows expansion of the cells and in normal cells its presence will halt the cell cycle to allow time for repair [41] [42]. An outline of the total result of these drugs in combination is seen in Figure 1.4.C.

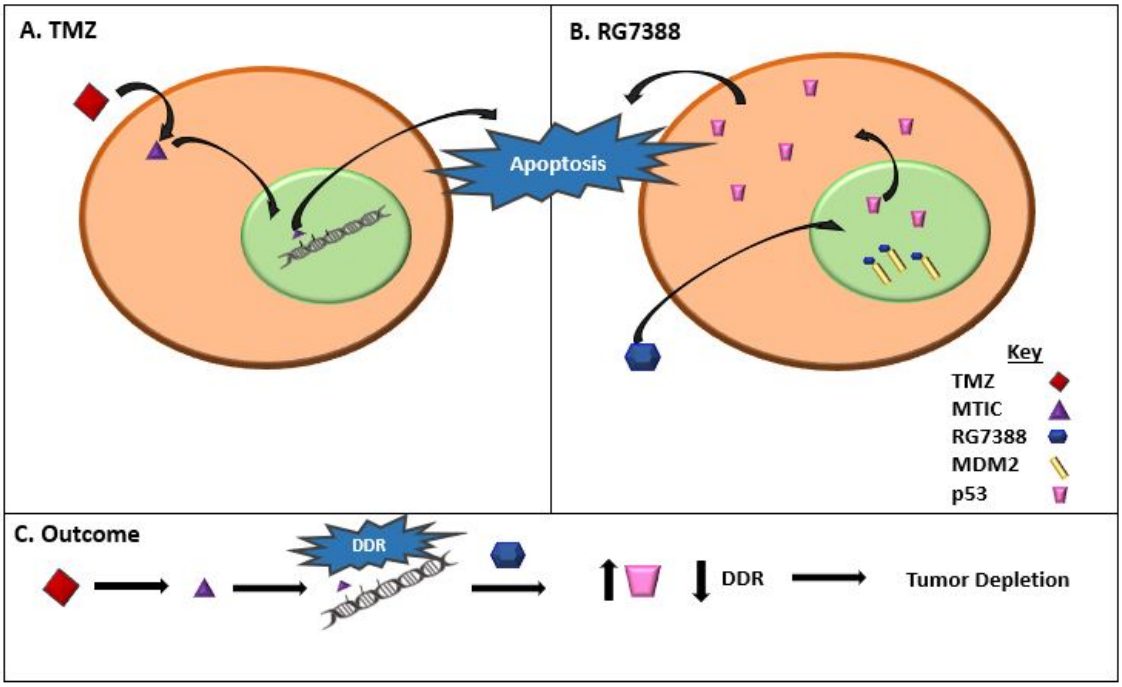

Fig. 1.4 TMZ/RG7388 combination therapy mechanism. (A) represents the mechanism that TMZ undergoes to send the cell towards apoptosis. (B) represents the mechanism RG7388 undergoes to kick start the p53 tumor suppression pathway. (C) represents the overall result of the two drugs in combination.

Paclitaxel (PTX) is another promising chemotherapeutic agent with many important characteristics to provide a powerful combination therapy with TMZ. PTX is an anti-microtubule agent, which binds to the β-tubulin subunit and stabilizes microtubules, resulting in disruption of microtubule dynamics and mitotic apparatus during cell division [43] [44] [45]. A recent study also found that PTX can stimulate autophagy and induce apoptosis [46]. However, PTX is a strong p-glycoprotein sub-

strate, and thus has limited distribution across the BBB [47]. Since TMZ and PTX inhibit the proliferation of tumor cells through different mechanisms, cross-resistance can be minimized. TMZ and PTX are chosen as a second option for combination therapy. Their mechanisms are outlined in Figure 1.5. In Figure 1.5.A, the same mechanism of TMZ occurs as was described previously. PTX works as a second hit to the tumor cells, potentially removing those that are TMZ resistant. In Figure 1.5.B, PTX enters the cell and binds to the β-tubulin. This suppresses microtubule detachement from centrosomes during mitosis and leads to a failure in cell division and ultimately further expansion of the tumor.

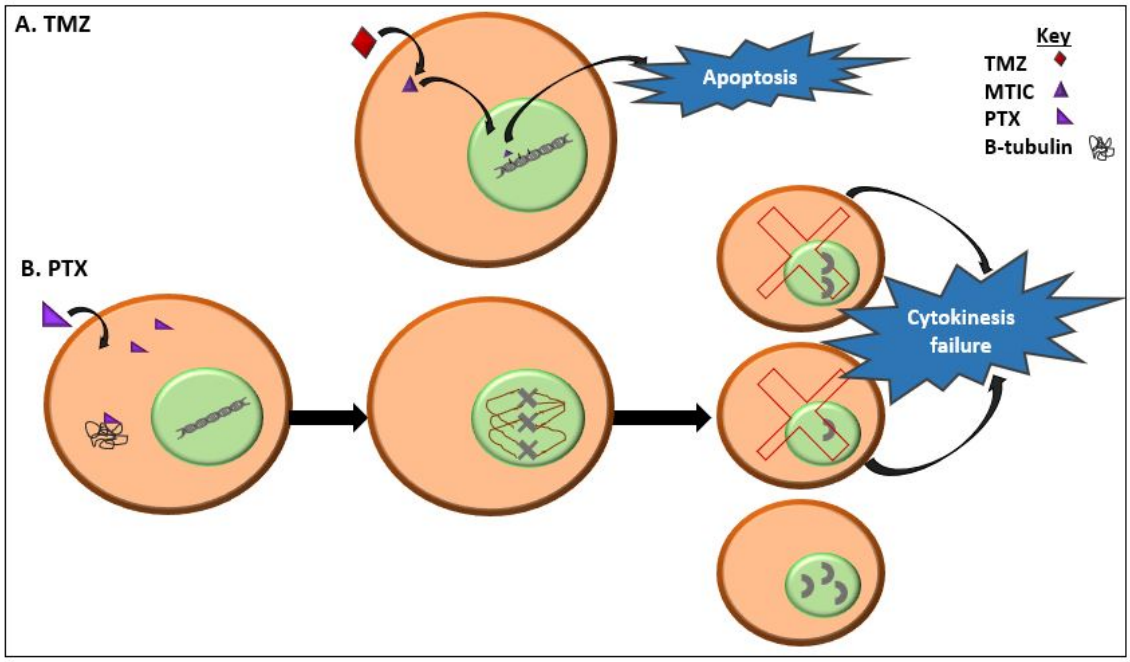

Fig. 1.5 TMZ/PTX combination therapy mechanism. (A) represents the mechanism TMZ undergoes to induce apoptosis in tumor cells. (B) shows the mechanism PTX uses during a tumor cell's mitosis that induces apoptosis.

1.4 Nanosystems

To date, single drug therapies have largely failed against GBM. Delivery systems at the nanometer level that allow therapeutic multi-drug combinations would potentially overcome this limitation. NPs have unique characteristics that can be developed toward this aim to increase concentration levels at the tumor site. If a potentially highly therapeutic drug cannot cross the BBB, the drug often must be abandoned in favor of drugs that can cross, even if less potent. Therefore, any nanosystem developed to treat GBM will need to facilitate passage through or around the BBB. While many small molecules are unable to cross the BBB, nanosystems may overcome challenges by eliminating potential interactions along the drug delivery route or containing molecules that provide a stealth component to decrease recognition by macrophages. Nanosystems can be further enhanced with disease-specific ligands that target biomarkers of interest to improve the biodistribution profile. Nanosystems encompass a variety of specific types including nanogels, nanosuspensions, nanoemulsions, and NPs [48]. Micelles, polymeric NPs and hybrid polymer-micellar NPs will be further discussed.

NPs are compact particles with diameters ranging from 1 to 1,000 nm and are actively being developed for both therapy and diagnostics [49]. NPs less than 100 nm have many advantages including enhanced solubility, increased bioavailability, increased surface area, and a potential decrease in dose required [50]. NPs may be composed of biodegradable and non-biodegradable constituents and are further categorized as polymeric, polymeric micelles, and inorganic, among others [51]. NPs are composed of three different layers: the outer layer for surface functionalization, the middle shell containing the NP materials, and the inner core important for encapsulating drugs [52]. NP size and surface characteristics can be easily manipulated for passive or active drug targeting [49]. Other advantages include the ability for site-specific targeting, ability to utilize various delivery routes, and ability for a more controlled and longer sustained release of drugs at the target site [49]. There are a

few disadvantages, however, such that small size and large surface area can lead to particle-particle degradation and drug loading may be limited with a burst release [49]. To construct a NP, the appropriate method must be chosen based on the materials and drugs used. Important considerations include the degree of biodegradability of the NP, desired size, surface characteristics, and drug solubility and stability [50].

While there are many methods of NP fabrication, including solvent evaporation, ionic gelation, or nanoprecipitation, solvent evaporation will be discussed in detail as it is most frequently used [53] [54]. Solvent evaporation can be split into single and double emulsions as shown in Figure 1.6. A single emulsion is chosen typically for encapsulation of hydrophobic drugs. This type would be characterized by an oil in water (o/w) emulsion and involves dissolving both drug and polymers into an organic solvent and emulsifying them, using ultrasonication, in an aqueous medium (Figure 1.6.A) [50]. A double emulsion can be used to encapsulate hydrophilic drugs or both hydrophilic and hydrophobic drugs. Traditionally, a hydrophilic drug is dissolved in an aqueous medium that is then emulsified into an oil solution containing the hydrophobic drug and polymers. The resulting solution is then emulsified into an aqueous medium, characterized by a water in oil in water (w/o/w) emulsion (Figure 1.6.B). With each emulsion it is required that each solution is completely immiscible with each other to allow the solvents to disperse evenly into a continuous phase and form the NP layers [55].

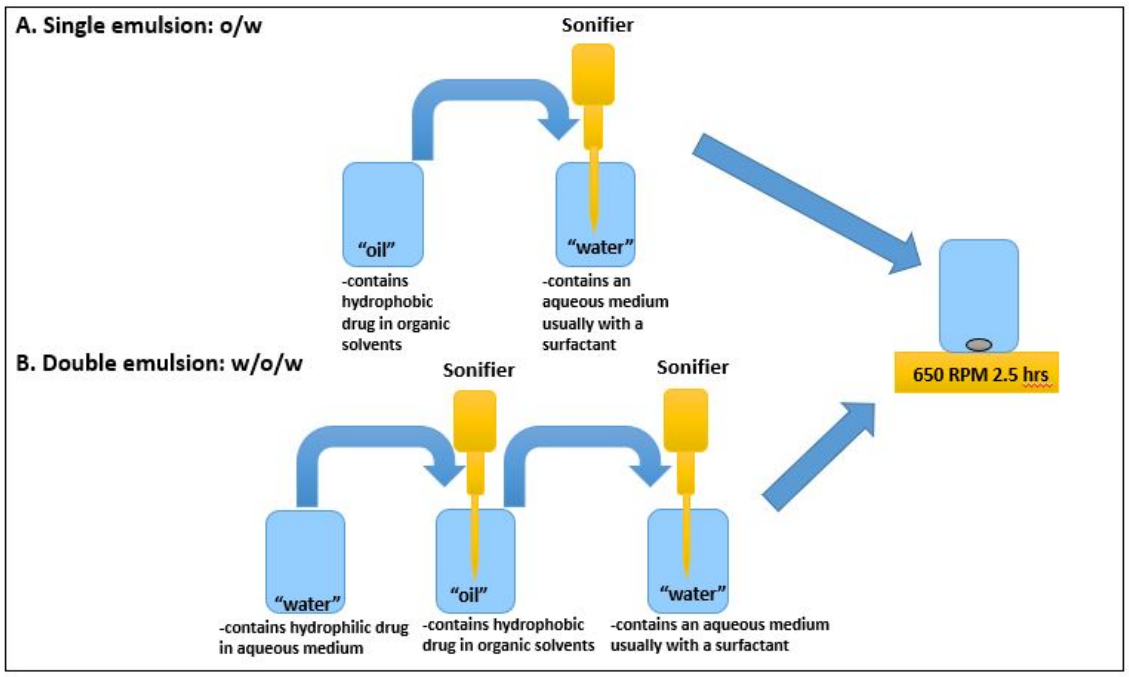

Fig. 1.6 Single and double emulsion scheme. The above scheme represents the steps taken during the solvent evaporation method for both a single (A) and double (B) emulsion.

A surfactant can be used to improve stability of the NPs, increase circulation blood in vivo, and prevent the NPs from combining together and forming larger particles [49] [56]. Selection of surfactant concentration is important because a low concentration of surfactant leads to an increased polydispersity and particle aggregation, while a high concentration can decrease drug loading [57].

1.4.1 Polymeric nanoparticles

Polymeric NPs are made of organic materials that can become multifunctional because of further conjugation after NP formation [52]. Polymeric NPs are also the simplest type often using single-chain polymers [48]. Many polymer chains contain groups such as carboxylic acids or amino groups that allow molecules to be conjugated to them for various applications. In addition, polymers can be chosen depending on

the time needed to release a drug from the system. Polymers with more organic material, such as methyl groups, will slowly hydrolyze in the body, hence slowing the release. Some polymer examples used include polylactic acid (PLA), polyethylene glycol (PEG), polycaprolactone (PCL) and chitosan. Poly(lactic-*co*-glycolic) acid (PLGA) is a common polymer used in the fabrication of polymeric NPs and combines both PLA and PGA. It is advantageous because it is biodegradable by hydrolysis and is also biocompatible. Varying the ratio of PLA to PGA allows for fine tuning of drug release, compared to each polymer alone, because as the ratio of PLA:PGA increases, the rate of hydrolysis decreases, slowing the release of drug. PLGA is also amphiphilic and spontaneously creates NPs for drug delivery. Chu et al. utilized PLGA NPs for the delivery of a TMZ-ester for increased drug delivery for GBM [2]. The PLGA NPs were constructed using an emulsion-solvent evaporation technique. PLGA and the TMZ-ester were dissolved in acetone and dicholormethane (DCM) and then added to a 1% polyvinyl alcohol (PVA) for sonication. These NPs were then conjugated to an anti-human ephrin type-A receptor 3 tyrosine kinase antibody to target GBM intranasally. This antibody was used to target the ephrin type-A recpetor 3 membrane-associated receptor over-expressed in the vasculature in GBM tumors. The conjugated NPs were approximately 146 nm and targeted the brain more effectively than unlabelled NPs as measured by fluorescence imaging in the in vivo rat models. Traditionally PLGA NPs are used because they are generally regarded as safe [58]. While Chu et al. was able to deliver the PLGA NPs intranasally, it has been shown that polymer NP size can be reduced through combination with micelles [58]. Although there is no known ideal size for brain delivery, it is generally thought that smaller is better.

1.4.2 Micellar nanoparticles

Micelles are amphiphilic surfactant molecules that spontaneously aggregate into spherical NPs [59]. In an aqueous environment, the hydrophobic head group of mi-

celles collects towards the center of the spherical particle and the hydrophilic tail group of the micelles collects towards the outer edges of the particle. Compared to liposomes, micelles are formed in a similar manner by self-assembly through the hydrophobic and hydrophilic groups. However, liposomes form a bilayer, similar to a cell membrane, and have the capability to contain both hydrophilic and hydrophobic drugs [59]. Also, liposomes tend to encapsulate smaller micelles on the inside to create the liposomal structure. One example of liposomes for the treatment of GBM comes from the fabrication of polyethyleneglycol-carbamyl distearoylphosphatidylethanolamine (DSPE-$PEG_{(2000)}$-NHS) loaded with chemotherapeutic drugs doxorubicin and erlotinib, then further conjugated with transferrin for mediated transcytosis and and penetratin for enhanced cell penetration [60]. These NPs were fabricated using a thin film hydration, but compared to micelle formation with solvent evaporation, this method was more laborious. For instance, they used three different phospholipids with DSPE-$PEG_{(2000)}$-penetratin, a pH gradient to encapsulate doxorubicin and a G100 sephadex column [60]. This fabrication resulted in a particle size greater than 150 nm and a polydispersity index (PDI) of 0.193. While this construct was effective at decreasing tumor volume over time in mouse in vivo models, the synthesis of such a construct can take time and be quite costly with the materials needed. In addition, this construct lacked a targeting moiety to effectively target the GBM tumor directly. This resulted in offsite binding in other organs such as the spleen and heart [60].

Micelles are chosen for our NP construct because of their small size. They also can be integrated into polymers and provide a simpler assembly as opposed to liposomes. Micelles rely on the principle of self-assembly. One method of inducing self-assembly involves dissolving block copolymer micelles into water-immiscible solvents. This solution is then dispersed amongst a continuous aqueous environment [55]. As the water-immiscible content exits the micelle, the self-assembly occurs to increase the surface area of the particle [55]. Micelles are beneficial because of their advantages in delivering hydrophobic drugs as well as their small size. Some examples of poly-

mers that have been incorporated into micelles include poly(ethylene oxide) (PEO), poly(propylene oxide) (PPO), polystyrene (PS), and PCL [59] [55]. One example of micelles utilized for the treatment of GBM inlcudes the use of PCL and methoxy-PEG copolymer [61]. Methoxy-PEG-PCL encapsulated both doxorubicin and honokiol for co-delivery. PCL formed the hydrophobic core while PEG was effective at stabilizing the shell of the NP in an aqueous environment. The NP size was 34 nm and showed strong anti-cancer effects such as tumor cell apoptosis, decreasing cell proliferation and tumor angiogenesis compared to single drug micelles [61]. While these NPs were effective at treating the tumor, they lacked functional groups to provide a theranostic approach. Micelles are effective delivery vehicles. However, their small size may lead to rapid clearance and may suffer from low drug-loading capacity [49] [58]. In addition, compared to polymer NPs, micelles lack strong intermolecular interactions with the encapsulated drug causing premature leakage [58].

1.4.3 Polymer-micellar nanoparticles

Polymer-micellar NPs have the opportunity to combine many of the advantages of polymer NPs and micelles while potentially avoiding some of their respective disadvantages. For instance, the polymer component provides structural stability while the micelle component allows decreased size [59] [58]. In addition, compared with traditional micelles, the combination of both components escapes rapid excretion, seen with micelles, as polymeric NPs have the ability to sustain drug relesase over time. Micelles are known to clear because they have hydrodynamic diameters similar to globular proteins and it has been shown that globular proteins of approximately 5-6 nm are associated with the ability to clear via renal filtration or urinary excretion [62]. The larger size of polymer-micelles prevents the rapid clearance. Nabar et al. produced polymer-micellar NPs containing both PLGA and poly(styrene-*block*-ethylene oxide) (PS-*b*-PEO) [58]. PLGA/PS-*b*-PEO particles with a polymer:micelle ratio equal to five achieved a particle size of about 50 nm. These particles achieved

a sustainable drug release characteristic across 25 days. However, the NPs lacked functional characteristics such as the ability to target a specific tissue or disease or to track via imaging. Based on many proposed advantages of polymer-micellar NPs, we chose this nanosystem for combination therapy.

1.4.4 Targeting cancer stem cells with nanoparticles

While CSCs appear to be a driver of GBM tumor recurrence and drug resistance, they may also hold the key to improved therapy, if not a cure, if they can be selectively targeted. Along with CD133, glioma CSCs also express other biomarkers including CD44, CD95, Nestin, and GFAP, which provides additional potential options for glioma CSC targeting [63]. Recent studies have shown the AC133 epitope on CD133 is a more specific marker for CSCs [4]. During CSC differentiation, the AC133 epitope becomes sequestered, which is therefore only present during its undifferentiated state. This provides an important opportunity for targeting the undifferentiated CSCs in a selective manner. Given the difficulties associated with developing antibodies to the AC133 epitope, aptamers are instead being developed because of their ability to conform to any three-dimensional shape to reproduce the active binding site of the target ligand. Additional advantages of aptamers include reduced immunogenicity which prevents premature clearance, high reproducibility, stable conformation, and much smaller size compared to antibodies, which may increase the likelihood of crossing cellular barriers. Figure 1.7 shows a representation of the potential size increase when conjugating an antibody to the NPs. Figure 1.7.A shows the 120 kDa antibody with the aptamer embedded to specifically target the CD133 epitope. Conjugating the entire antibody may result in an increase in size. Figure 1.7.B shows the fifteen base pair aptamer specific to the epitope that can be conjugated to the NPs and potentially maintain similiar size.

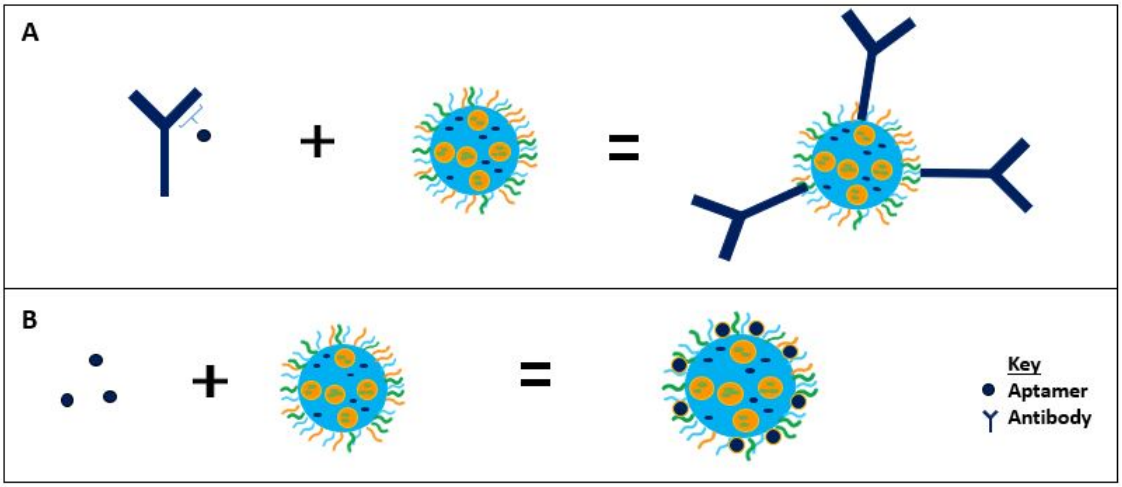

Fig. 1.7 Conjugation of aptamer compared to antibody. (A) represents the antibody being conjugated to the nanoparticles, potentially increasing size. (B) represents the aptamer being conjugated to the nanoparticles, potentially maintaining size.

Aptamers have been previously conjugated and used as a targeting agent in drug delivery via nanosystems. Gui et al. used an aptamer for CD133 to conjugate lipid-polymer NPs for drug delivery to osteosarcoma initiating cells [64]. Addition of the aptamer increased the size of NPs by only 7 nm. In an in vivo model of BALB/c nude mice bearing an osteosarcoma xenograft of $Saos^{-2}$ cells, the targeted particles reduced tumor size more avidly compared to nontargeted NPs [64]. Shigdar et al. identified and produced a 15 nucleotide RNA aptamer (5'-CCCUCCUACAUAGGG-3') conformation that binds to the CD133 epitope for greater penetration and more stable uptake into tumorspheres generated by either colorectal cancer cells or embryonic kidney cells [65]. Therefore, using this aptamer in a drug delivery system can potentially enable a highly efficacious, site-specific therapy, thereby reducing unintended side effects.

1.4.5 Modifiying nanoparticles

NPs can be modified to carry a variety of different molecules for both targeting and imaging. Targeting agents include proteins, peptides, nucleic acids, and small molecules [66]. One way to conjugate an aptamer to NPs is through an N-hydroxysuccinimide (NHS) and 1-ethyl-3-(3-dimethylaminopropyl) carbodiimide (EDC) reaction. NPs containing polymers like PLGA contain a carboxylic acid at its end and EDC is used to activate the carboxylic acid group to facilitate binding to NHS. This then allows the covalent bonding of primary amines found on aptamers to the NHS group. EDC reacts with the carboxylic acid and forms an O-acylisourea intermediate that is displaced by the primary amine. NHS is used to improve the efficiency of the binding by forming a more stable intermediate (Figure 1.8).

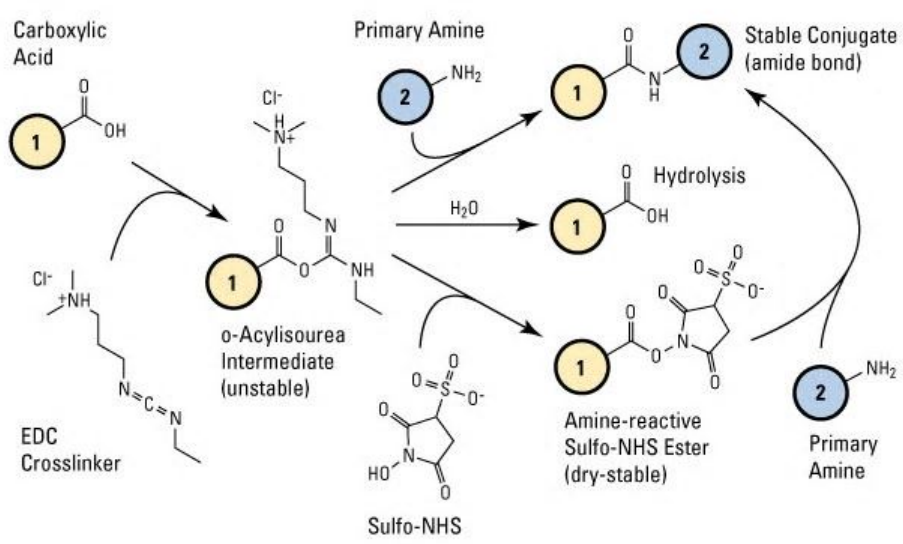

Fig. 1.8 The above figure represents the chemical pathway followed during an NHS/EDC reaction to form a covalent bond between a carboxylic acid on NPs and a primary amine on aptamers.

We can use a PLGA that contains an NHS group as opposed to a carboxylic acid. Because the amine reactive NHS ester is already within the NPs, this eliminates the

need for the use of EDC which may provide toxicity to in vitro studies if not fully removed.

The versatility of NPs allows a vast array of options for developing imaging-based contrast agents. One example is through the use of zirconium-89 (^{89}Zr) for positron emission tomography (PET) imaging given its high 511 keV gamma emission [51]. ^{89}Zr was originally utilized for antibody labelling because its longer half-life of 78 hours corresponds with the three day half-life of circulating therapeutic antibodies. This allows an optimal amount of time for labeling the NPs and the ability to monitor the biodistribution of NPs in vivo over time. To effectively chelate the ^{89}Zr to the NPs, deferoxamine (DFO) is used as a chelating agent. DFO is a hexadentate siderophore that has the ability to chelate metals through three hydroxamate groups [67]. First, the DFO is covalently conjugated to an amino group on the NPs through amide formation. The ^{89}Zr is then contained on the inside of the DFO in a ring-like structure to allow for imaging of the NPs. The goal is to maintain the ^{89}Zr covalent bond to the NPs throughout their time travelling to the tumor and this can modelled with labelling efficiency studies. Using this process, Veronesi et al. was able to achieve a 60% binding efficiency when labelling polymer micellar NPs using DFO [68].

1.4.6 In vitro analysis

The in vitro setting is important for testing the effectiveness of new therapies. When testing multi-drug delivery vehicles, it is important to understand the cytotoxity of the encapsulated drugs alone, in combination and packaged in the vehicle. To determine the cytotoxic effect of the various treatment groups, the Chou-Talalay method outlined by Chou et al. and is used to predict drug cytotoxicity and the effects of combining therapeutic agents during in vitro studies [69]. In combination, cytotoxic drugs can produce three different effects: an additive effect, a synergistic effect or an antagonistic effect. An additive effect is the effect that would be produced if the fractional effect of each drug in combination is equal to one as if the

two drugs were the same. A synergistic effect is when two drugs produce an effect greater than an additive effect, while an antagonistic effect is an effect less than an additive effect [69]. Drugs in combination can be analyzed using a combination index (CI) rather than assessing for statistical difference in cytotoxicity to depict synergism (CI<1), additive effect (CI=1), or antagonism (CI>1) [70]. The median effect or the IC_{50} value represents the predicted drug concentration where 50% cell killing is expected, which we can assess with the mathematical software CalcuSyn 2.0. The Chou-Talalay method is used in the analysis by CalcuSyn 2.0, but some background information is needed. First, drug potency and the shape of the dose curve (m) is considered in the mathematical analysis. The fractional product concept is based on the idea that a drug alone produces a sigmoidal or flat sigmoidal curve of effect. During a dose curve analysis, the fraction of cells killed is the fraction of cells affected (Fa). The fraction unaffected (Fu) is determined by the following equation:

$$Fu = 1 - Fa \tag{1.1}$$

The median-effect equation is used to describe the dose-effect relationship [69]:

$$\frac{Fa}{Fu} = (\frac{D}{D_{\mathrm{m}}})^{\mathrm{m}} \tag{1.2}$$

In this equation, D is the dose of drug given to produce a specific Fa and D_m is the median-effect dose or the IC_{50}. The sigmoidal curve can be linearized by rewriting Equation 1.2 in the following form [69]:

$$log(\frac{Fa}{Fu}) = mlog(D) - mlog(D_{\mathrm{m}}) \tag{1.3}$$

When plotting dose-effect curves in such a manner, the conformity of the plot can be manipulated by adjusting the value of the linear correlation coefficient (r). For this study, a correlation coefficient ≥ 0.95 is generated. By this method, every treatment dose may not be included for the analysis as they may not fit in the empirical curve; however, the empirical curve that will provide the best analysis for the IC_{50}. To determine the CI values, Calcusyn 2.0 uses the following equations from the analysis

of two drugs alone to determine if they are additive, synergistic, or antagonistic at each effect [69]:

$$CI = \frac{(D)_1}{(D_x)_1} + \frac{(D)_2}{(D_x)_2} \tag{1.4}$$

In this equation, $(D)_1$ and $(D)_2$ refer to the dose of drug 1 and 2 alone that inhibit the cell system at x% and $(D_x)_1$ and $(D_x)_2$ refer to the dose of drug 1 and 2 in combination that inhibit the cell system at the same x%. This analysis is important to consider when encapsulating drugs as a preliminary step because single drugs may produce a certain potent cytotoxicity, but may be inhibitory when administered in combination.

1.4.7 In vivo imaging

PET is a highly quantitative and sensitive tool that has the ability to depict the distribution of positron (β^+ particle)-emitting radionuclides such as ^{89}Zr [51]. As the positrons are emitted, they collide with free electons in the body emitting kinetic energy in the form of two 511 keV gamma photons and this pair is detected by a PET scanner [51].

While PET is extremely useful in quantitatively and specifically analyzing distribution of radionuclides, it lacks anatomical features. By coupling images from MRI with images from PET, we have the ability to determine the biodistribution of radionuclides bound to NPs in an animal model. To image the biodistribution or treatment progression of the NPs, combining both MRI and PET can be used. MRI is a non-ionizing imaging technology that uses a magnet to produce three-dimensional images [51]. MRI can be used to determine an anatomical layout and can also be used for determining presence of tumor in the brain.

1.4.8 Intranasal delivery

In addition to potentially improving GBM therapy through combination treatment and through the use of polymer-micellar NPs, an alternative route may also improve treatment distribution to the brain. As discussed, the BBB has a barrier composed of

tight endothelial cells that prevent the passing of most small molecules. Circumventing the BBB through an alternative route of intranasal drug delivery (INDD) may at the very least be equivalent to intravenous administration, if not better. When drugs travel intranasally, they avoid the BBB and rather cross into the brain along a perineuronal/perivascular route to the brain including across the cribriform plate (Figure 1.9) [51]. The topic of nose-to-brain delivery and imaging techniques to monitor therapy is extensively being developed, which we have reviewed and published recently (Appendix 1) [51]. Overall, designing a drug delivery system that has the potential to be distributed both intravenously and intranasally would increase delivery route options when conducting in vivo studies.

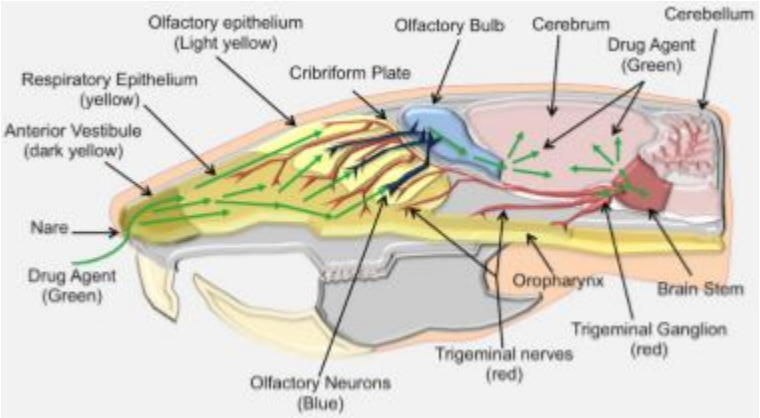

Fig. 1.9 Rat nose-to-brain anatomy. The nose-to-brain anatomy of the rat highlights the potential routes NPs would take in order to cross into the brain [51].

2. OBJECTIVES

1. Produce a polymer-micellar nanoparticles less than 100 nm in size (Figure 2.1.1)

2. Encapsulate both TMZ and RG7388 into the nanoparticles (Figure 2.1.2)

3. Conjugate an aptamer to the nanoparticles to target the CD133 epitope of the CSC population (Figure 2.1.3)

4. Label a PET radiotracer, ^{89}Zr, to the nanoparticle for future in vivo studies (Figure 2.1.4)

5. Perform in vitro analysis on the nanoparticles in the CSC population and compare to free drugs (Figure 2.1.5)

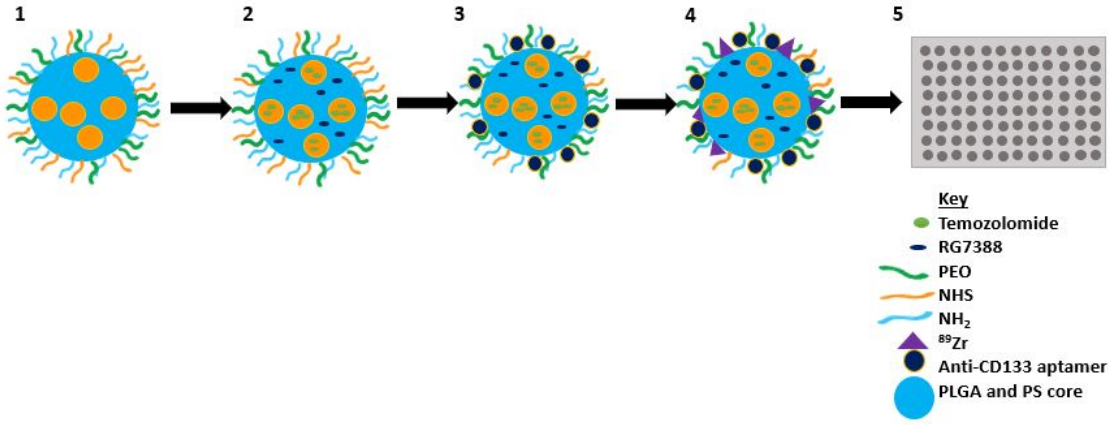

Fig. 2.1 List of nanoparticle objectives.

3. MATERIALS AND METHODS

3.1 Materials

3.1.1 Nanoparticle fabrication

Carboxyl-terminated PS-*b*-PEO (molecular weight 5,000-*b*-2,200, Cat No P4090-SEOCOOH) and carboxyl-terminated PS-*b*-PEO (molecular weight 9,500-*b*-18000 Da, Cat No P18154-SEOCOOH) were purchased from Polymer Source Inc. (Montreal, QC, Canada). PLGA (molecular wieght 73,000 Da, Cat No APO60), PLGA-NH_2 (diamine) (PLGA-NH_2) (molecular weight 30,000-40,000 Da, Cat No AI062) and PLGA-N-hydroxysuccinimide (PLGA-NHS) (molecular weight 50,000-80,000 Da, Cat No AI116) were purchased from PolySciTech (West Lafayette, IN). Poly(vinyl alcohol) (PVA) (molecular weight 13,000-23,000 Da, Cat No 348406) and PVA (molecular weight 31000-50000, Cat No 363138) were purchased from Sigma Aldrich (St. Louis, MO). Pluoronic F-68 Prill 188 (Material 30085243) was purchased from BASF (Mount Olive, NJ). Temozolomide (TMZ) (Cat No T2577) was purchased from Sigma Aldrich (St. Louis, MO). RG7388 (Cat NO HY-15676/Cs-1473) was purchased from MedChem Express (Monmouth Junction, NJ). Paclitaxel (PTX) (Cat No A10689) was purchased from AdooQ Bioscience (Irvine, CA). Hydrochloric acid (HCl) (0.1N, Cat No S25354) was purchased from Fisher Scientific (Waltham, MA). Dichloromethane (DCM) (Cat No AC406920010) was purchased from Fisher Scientific (Waltham, MA). Formic acid ($\leq$95%, Cat No F0507-500mL) was purchased from Sigma Aldrich (St. Louis, MO). Acetonitrile (ACN) (Cat No A996-4) was purchaseed form Fisher Scientific (Waltham, MA). Ethyl acetate (Cat No 035909) was purchased from Oakwood Chemical (Estill, SC).

3.1.2 Nanoparticle conjugation

Non-fluorescent CD133 aptamer (5'(C6-NH_2) CCC UCC UAC AUA GGG 3' PO RNA) (Cat No O-5100) was purchased from TriLink Biotechnologies (San Diego, CA). Fluorescein amidite (FAM)-azide labelled CD133 aptamer (5' C6-NH_2) CCC UCC UAC AUA GGG (FAM-Azide) 3') was purchased from Integrated DNA Technologies, INC. Water (for RNA work) (Cat No BP561-1) was purchased from Fisher Scientific (Waltham, MA). Tris-Acetate-EDTA (TAE) (10X solution, Cat No BP1335-1) was purchased from Fisher Scientific (Waltham, MA). $^{89}Zr(HPO_4)_2$ solution was from Washington University (St. Louis, MO). Deferoxamine mesylate salt, the mesylate salt of DFO, (DFOM) ($\leq$92.5% (TLC) Cat No D9533) was purchased from Sigma Aldrich (St. Louis, MO).

3.1.3 Cell studies

Human GBM43 cells were kindly donated from the Simon Cancer Center at Indiana University. Culture media was Gibco Dulbecco's Modified Eagle Medium (DMEM) with 4.5 g/L D-Glucose, L-Glutamine and was purchased from Life-Technologies (Grand Island, NY) with 10% Fetal bovine serum (FBS) (Cat No 35-016-CV) from Corning Inc. (Corning, NY) and 1% HEPES buffer (1M pH 7.3, Cat No 118-089-721) was purchased from Quality Biological (Gaithersburg, MD). Methylene blue (1% in ethanol, Cat No LC169201) was purchased from LabChem (Zelienople, PA). Human GBM cancer stem cells (CSCs) (Cat No 36104-41) were purchased from Celprogen (Torrance, CA). Culture media was Human Glioma Cancer Stem Cells Media with Serum (Cat No M36104-40S) requested without antibiotics and was purchased from Celprogen (Torrance, CA). Methylene blue (1% in ethanol, Cat No LC169201) was purchased from LabChem (Zelienople, PA).

3.2 Methods

3.2.1 Particle constituent analysis

Determination of 0.5% 13k polyvinyl alcohol viscosity

To determine the viscosity of 0.5% 13k PVA, the Bohlin CVO 100 Rheometer from Malvern Panalytical (Malvern, UK) was used. The viscosity of the solution was measured in triplicate and was collected as an average value of the instantaneous velocity once the instrument levelled off in values.

Analysis of TMZ by UV-Vis spectroscopy

For analysis of NPs encapsulating multiple drugs, methods were developed to analyze drug content. To analyze TMZ by UV-Vis for the single emulsion NPs, absorbance was measured at 325 nm, comparable to the literature maximum of 328 nm [5]. A standard curve was made in triplicate.

To improve measurement by UV-Vis spectroscopy, prior to beginning double emulsion fabrication of NPs, the maximum wavelength was determined on the UV-Vis spectrophotometer. A scan from 270 nm to 380 nm was conducted to determine the maximum TMZ absorption wavelength in dimethyl sulfoxide (DMSO). A standard curve was generated reading at 332 nm and was prepared in triplicate to measure drug content.

Analysis of polymers by UV-Vis spectroscopy

To determine if polymers interfere with UV-Vis analysis of TMZ content, absorbance scans of each polymer dissolved in DMSO was conducted.

TMZ stability

Because TMZ hydrolyzes at physiologic pH, it was necessary to determine the stability of TMZ in aqueous solutions at various pH to improve the formulation of the NPs. TMZ was dissolved in deionized water at pH 3.48 (pH 4), pH 4.87 (pH 5), pH 6.88 (pH 7) and analyzed by UV-Vis spectroscopy scanning from 220 nm to 370 nm to monitor for degradation or the presence of new peaks as an indication of conversion to MTIC/AIC. Measurements were conducted in triplicate over the course of two weeks.

Method determination for HPLC drug analysis

High pressure liquid chromatography (HPLC) was used as a quantitative method for the determination of drug content on an Agilent 1200 Dual-Loop Series Autosampler from Agilent Technologies (Santa Clara, CA). A novel method was developed for the separation of TMZ and RG7388. TMZ and RG7388 were dissolved in ACN and were separated using a mobile phase of water and ACN. The samples were injected through a Zorbax Eclipse C8 4.6 x 150 mm 5 μm column from Agilent Technologies (Santa Clara, CA). Reference wavelengths for all three methods were set to 332 nm for TMZ, 273 nm for RG7388, and 227 nm for PTX. Important criteria was that between each drug component, a flat baseline needed to be established in order to accurately measure concentration. The first method to separate the two drugs was using a 50:50 ratio of water and ACN. The injection volume was 3 μL, flow rate was 1 mL/min and the temperature was 40 °C. The next method to separate the drugs used solvent ratios that can be seen in Table 3.2. However, the water was not mixed with formic acid initially and the flow rate was 1 mL/min with an injection volume of 3 μL.

3.3 Nanoparticle fabrication

3.3.1 Single emulsion nanoparticles

A solvent emulsion evaporation system was adapted from previous work of Nabar et al. to initially fabricate the NPs [58]. To form the oil phase for TMZ-loaded NPs, 200 μL of either 0.1% PS(5.0k)-*b*-PEO(2.2k) or 0.1% PS(9.5k)-*b*-PEO(18k) dissolved in DCM and 20 μL of 5% 50:50 73k PLGA dissolved in DCM were combined with 500 μL of 0.1% TMZ dissolved in 135 μL of DMSO and 2.865 mL of DCM. The organic phase was vortexed for 30 seconds and added dropwise to 8 mL of 0.5% 13k PVA. During addition of the organic phase, the solution was sonicated using a Branson 250 probe sonicator from Branson Ultrasonics (Danbury, CT) at constant duty cycle for five minutes at 20% power over ice. After sonication, the emulsions were stirred at 650 rpm for 2.5 hours to allow the organic solvents to completely evaporate. Figure 1.6.A outlines the process described above for single emulsion fabrication of NPs. Each sample, unless otherwise noted, was prepared in triplicate. TMZ+RG7388 NPs were fabricated using the same method, however, the 500 μL of drug added contained 0.1% solution of TMZ and 0.1% RG7388 dissolved in 225 μL of DMSO and 2.775 mL of DCM. Control NPs were fabricated the same way without the drugs added and consisted of empty PLGA-PS-*b*-PEO particles, PLGA particles, and PS-*b*-PEO particles. PS-*b*-PEO control micelles were fabricated using 800 μL of 0.1% of PS-*b*-PEO to improve polymer concentration.

To purify the NPs, a similar method to Nabar et al. was used [58]. The NPs were filtered using a 0.45 μm filter to remove any aggregates. NPs were centrifuged at 2,300 rcf for one hour. The supernatant was then removed and replaced with MilliQ water. This process was then repeated two more times for thirty-minute cycles each. These low speeds were used for purification in order to prevent aggregation of the NPs [58].

3.3.2 Double emulsion nanoparticles

A double emulsification solvent evaporation technique adapted from Xu et al. was used to prepare the next set of NPs [71]. Prior to choosing a final method for the double emulsion NPs, many combinations and techniques were tested including sonication time, molecular weight of PLGA, surfactant type, surfactant molecular weight, surfactant concentration, technique of transfer and organic to aqueous phase volume ratios. Table 3.1 outlines the different methods tested during the preliminary discovery stages. The size of the NPs were the determining factor in selecting the final method.

The final method for double-emulsion NPs maintained the same PLGA:PS-*b*-PEO weight ratio of 1:5 as used in the single-emulsion NPs [58]. To synthesize NPs with TMZ only, 389 μL of 0.3% PS(9.5k)-*b*-PEO(18k) was dissolved in DCM for at least 30 minutes and combined with either 324 μL of 1.8% 50:50 73k PLGA or 162 μL of 1.8% 50:50 50k PLGA-NHS and 162 μL of 1.8% 50:50 30k PLGA-NH_2 dissolved in DCM for about 30 minutes. The organic phase was vortexed for 30 seconds. This organic phase was sonicated over ice using the Branson 250 probe sonicator at constant duty cycle for 2 minutes at 20% power. Immediately after starting the sonication, 80 μL of 0.4% TMZ in 0.1N HCl, which had been thoroughly dissolved using bath sonication and applying heat, was added dropwise to form the first emulsion. Once completed, the first emulsion was added dropwise to 4 mL 0.5% 13k PVA at pH 4 for a second emulsion at constant duty cycle for 5 minutes at 20% power. An additional 1 mL of PVA was used to wash the remaining particles from the first emulsion into the second emulsion. After sonication, the NPs were left to stir for 2.5 hours at 650 rpm for evaporation of the organic solvents. To fabricate dual-drug NPs, either 43 μL of 0.2% RG7388 dissolved in ethyl acetate or 23 μL of 0.4% PTX dissolved in DCM was added to the initial organic phase after the 30 second polymer vortex. The entire organic phase was then vortexed for an additional 30 seconds.

Table 3.1

Double emulsion discovery stages. This table describes the steps taken in order to finalize a method for double emulsion fabrication of NPs prior to adding combination therapy

Formulation	**Micelle**	**Polymer**	**Oil Phase**	**TMZ**	**Surfactant**	**Emulsion Times (1,2)**	**Comments**
A	PS-*b*-PEO (0.3%, 389 μL)	73k PLGA (1.8%, 324 μL)	DCM	0.5%, 80 μL	13k PVA (5%, 5 mL)	2 min, 2 min	n/a
B	PS-*b*-PEO (0.3%, 389 μL)	73k PLGA (1.8%, 324 μL)	DCM	0.5%, 80 μL	F-68 (5%, 5 mL)	2 min, 2min	n/a
C	PS-*b*-PEO (0.3%, 389 μL)	73k PLGA (1.9%, 324 μL)	DCM	0.5%, 80 μL	13k PVA (5%, 5 mL)	2 min, 5 min	n/a
D	PS-*b*-PEO (0.3%, 389 μL)	73k PLGA (1.8%, 324 μL)	DCM	0.5%, 80 μL	13k PVA (0.5%, 5 mL)	2 min, 5 min	n/a
E	PS-*b*-PEO (0.3%, 389 μL)	73k PLGA (1.8%, 324 μL)	DCM	0.5%, 80 μL	13k PVA (1%, 5 mL)	2 min, 5 min	n/a
F	PS-*b*-PEO (0.3%, 436 μL)	73k PLGA (1.8%, 364 μL)	DCM	0.5%, 80 μL	13k PVA (0.5%, 3 mL)	2 min, 5 min	Solvent ratio - 1:10:35
G	PS-*b*-PEO (0.3%, 436 μL)	73k PLGA (1.8%, 364 μL)	DCM (w/ 7% Tween)	0.5%, 80 μL	13k PVA (0.5%, 5 mL)	2 min, 5 min	n/a
H	PS-*b*-PEO (0.1%, 400 μL)	73k PLGA (5%, 40 μL)	DCM	0.5%, 80 μL	13k PVA (0.5%, 8 mL)	2 min, 5 min	Additional 200 μL DCM added to oil phase
I	PS-*b*-PEO (0.1%, 400 μL)	73k pLGA (5%, 40 μL)	Chloroform	0.5%, 80 μL	13k PVA (0.5%, 8 mL)	2 min, 5 min	Additional 200 μL chloroform added to oil phase

For this method, the NPs were filtered using the 0.45 μm filter and then were collected using an Amicon Ultra-15 centrifugal filter from Millipore Sigma (Burlington, MA) with a 100 kDa molecular weight cut off. NPs were added to the filter and centrifuged at 5,000 rcf for 20 minutes. The NPs were washed with deionized water pH 4 twice for 15 minutes at 5,000 rcf and for a final wash and centrifugation of 40 minutes at 5,000 rcf. The remaining suspended NPs were then either used immediately or lyophilized in a Labconco freeze dry system, Freezone 4.5 from Labconco Corporation (Kansas City, MO) until further use.

3.4 Nanoparticle characterization

3.4.1 Size, PDI, and charge by dynamic light scattering

A Malvern Panalytical Zetasizer (Malvern Panalytical, Malvern, UK) was used to measure the hydrodynamic diameters of the particles through dynamic light scattering (DLS). Particles were dropped into either water or 0.5% 13k PVA with viscosity values set to 0.8872 cPs or 2.78 cPs, respectively. The viscosity for 0.5% 13k PVA was used after the initial discovery stages of double emulsion particle fabrication. The particle concentration was adjusted in order to maintain a scattered light intensity between 100 and 200 kilocounts per second. Laser illumination was applied at 633 nm and the detector was set to 90°. This measurement determined the PDI to serve as a quantitative analysis of uniformity within the NP sample.

The Malvern Panalytical Zetasizer was also used to measure the zeta-potential or surface charge of the NPs. Laser illumination was applied at 633 nm and the detector was set to 90°. Particle size and zeta-potential were measured prior to collection.

3.4.2 Size and PDI stability of NPs

TMZ-loaded PS-*b*-PEO+PLGA-NHS/PLGA-NH_2 NPs were measured at various time points in order to assess size and PDI stability when the NPs are stored at 4°C

in the 0.5% 13k PVA solution at a pH$\leq$4. Size and PDI were measured with DLS at time zero, 24 hours, and 8 days.

3.4.3 Transmission electron microscopy

NPs were placed on a formvar/carbon-coated 200 mesh grid from Electron Microscopy Sciences (Hatfield, PA) and allowed to absorb for three minutes after which the remaining solution was wicked away. The grid was then placed on a drop of 1% uranyl acetate in distilled water for three minutes. The grid was allowed to dry on filter paper. It was then viewed on a ThermoFisher Spirit Transmission Electron Microscope (Hillsboro, OR), and images were taken with a CCD Camera from Advanced Microscopy Techniques (Danvers, MA).

3.4.4 Drug encapsulation and drug-loading percentage by UV-Vis spectroscopy

The TMZ-loaded NPs were fabricated using the same methods, however, for single emulsion NPs, five times the initial concentration of TMZ stock was made (0.5% instead of 0.1%). The evaporated NPs for single and double emulsion were purified to remove un-encapsulated TMZ using their respective methods. The washed pellets were dried under vacuum. For measurement of single emulsion NPs, the pellets were dissolved into a known volume of DMSO and were measured according to a literature value for the maximum absorbance of TMZ, 325 nm, and were compared to a standard curve. For measurement of double emulsion NPs, additional steps were taken to remove absorption interference from PS-*b*-PEO. The pellets were dissolved in DMSO to release the encapsulated TMZ into solution. Then, the PS-*b*-PEO was precipitated with 0.1N HCl and filterd with 0.22 μm filter. TMZ was then measured by UV-Vis

spectroscopy at 332 nm and compared to a standard curve. Drug encapsulation efficiency was determined by the following equation:

$$EE\% = \frac{Drug_{\text{Encapsulated}}\,(mg)}{Drug_{\text{Added}}\,(mg)}\,x\,100 \tag{3.1}$$

Drug loading percentage was determined by the following equation:

$$DL\% = \frac{Drug_{\text{Encapsulated}}\,(mg)}{Nanoparticle Weight\,(mg)}\,x\,100 \tag{3.2}$$

3.4.5 Drug encapsulation and drug-loading percentage by HPLC

A standard curve of either TMZ or both TMZ and RG7388 dissolved in ACN was measured with HPLC on the same day as the analysis to avoid any environmental changes from day to day measurements. The standard curve was made starting with 54 μg/mL of TMZ and 51.6 μg/mL of RG7388 and diluted to make at least five standards. These were plotted by comparing concentration to area under the curve. Standards and unknowns were injected at a volume of 100 μL through a Zorbax Eclipse C8 4.6 x 150 mm 5 μm column. Mobile phase consisted of ACN and water adjusted to pH 4 using formic acid and the samples were analyzed according to the following method in Table 3.2.

Table 3.2
Method for HPLC separation of TMZ and RG7388

Time (min)	Water (%)	ACN (%)	Flow (mL/min)
0.0	20.0	80.0	0.8
2.0	20.0	80.0	0.8
7.0	5.0	95.0	0.8
10.0	0.0	100.0	0.8
12.0	0.0	100.0	0.8
13.0	20.0	80.0	0.8

3.4.6 Conjugation of anti-CD133 aptamer

To conjugate the aptamer to the NPs containing PLGA-NHS, the NHS to amine reaction was employed following click chemistry. One batch of NPs, containing approximately 7 mg of NPs were suspended in DNAse and RNAse free PBS at pH 5. Next, 20 μL of the anti-CD133 aptamer, either fluorescent or non-fluorescent, was added from a stock solution of 100 μM. The NPs were then protected from light and stirred at room temperature at 600 rpm for 2 hours. After stirring, the NPs were collected by ultra-centrifugation using a Centriprep-10 with a molecular weight cut off of 10 kDa for 20 minutes at 3,000 g. The filtrate contained the free, unbound aptamer while the substrate contained the NPs bound to the aptamer. The NPs were then washed using DNAse and RNAse free water and ultra-centrifuged for 15 minutes at 3,000 g.

To measure the efficiency of the aptamer, the fluorescent anti-CD133 aptamer with the FAM linker was conjugated. A standard curve consisting of six known standards was made and measured each time using a Victor 3V 1420 Multilabel Counter from Perkin Elmer (Waltham, MA). Fluorescence was measured by using an excitation wavelength of 485 nm and an emission wavelength of 535 nm. The fluorescence of the aptamer bound to the NPs was then compared to the standard curve. Binding efficiency was determined by the following equation:

$$Binding\ Efficiency = \frac{Bound\ Aptamer\ (\mu moles)}{Initial\ Aptamer\ (\mu moles)}\ x\ 100 \tag{3.3}$$

3.4.7 Stability of anti-CD133 aptamer

Preliminary studies were conducted to analyze the stability of the aptamer bound to the NPs. To analyze whether or not the aptamer was stably bound to the NPs, an electrophoretic mobility shift assay (EMSA) was conducted. NPs were conjugated to the anti-CD133 aptamer. NPs were ran on a horizontal 1.5% agarose gel for forty minutes at 150 V in 1X TAE buffer. Lane 1 consisted of 10 μL from a stock solution

of trypan blue (10 μL), DNAse/RNAse free water (90 μL), and glycerol (2 μL). Lane 2 contained 10 μL of a stock solution containing free fluorescent aptamer (1 μL), glycerol (20 μL), and DNAse/RNAse free water (179 μL). Lanes 3-5 contained different batches of conjugated NPs. These lanes were loaded with 10 μL of solution from a stock that contained 10 μL of aptamer bound NPs and 2 μL of glycerol. The gel system was placed in ice and protected from light.

To analyze the binding stability over time, the binding efficiency of the aptamer was measured using the same method as above. The sample was then placed in the 37 °C incubator to mimic in vitro conditions. At various time points, the NPs were centrifuged in a Centriprep-10 centrifugal filter with a molecular weight cut off of 10 kDa for 15 minutes at 3,000 g. The time points were 0 hours, 0.5 hours, 1 hour, 3 hours, and 24 hours. A known volume of NPs with the bound aptamer was collected and compared against a standard curve by analyzing with the plate reader under the same conditions previously listed. Due to constraints of time available in the lab, this experiment was conducted with a sample size of one.

3.4.8 Conjugation of ^{89}Zr

To conjugate ^{89}Zr to the NPs, two different methods were explored for determining an optimum binding efficiency. First, 1.5 mg of aptamer-conjugated NPs were dispersed in 2 mL HEPES buffer to neutralize any acidity. The NPs used were washed with HEPES buffer after conjugation to the aptamer. This was then added to 1 mL of 20 mM deferoxamine mesylate (DFOM) in water, the mesylate salt of DFO. The NPs were then stirred for one hour at room temperature to conjugate the amine group and DFOM. Excess DFOM was then removed by ultra-centrifugation for 40 minutes at 5,000 g using an Amicon Ultra-15 with a molecular weight cut off of 100 kDa. The NPs were washed with HEPES buffer for an additional spin of 40 minutes at 5,000 g. ^{89}Zr oxalate was neutralized using 60 μL of HEPES buffer and 60 μL of potassium carbonate (K_2CO_3). 200 μCi of ^{89}Zr was added to the NPs, mixed and then incubated

for 1 hour at 37°C. NPs were then added to HEPES buffer and centrifuged under the same conditions. This method was conducted in triplicate.

The second method was similar with slight modifications. An entire batch of aptamer-conjugated NPs containing approximately 7 mg of NPs were washed with HEPES buffer and suspended in 2 mL of 20 mM DFOM in water. This solution was stirred overnight at room temperature to conjugate the amine group to the DFOM. NPs were collected after adding the solution to 10 mL of HEPES buffer with the same method. NPs were collected from the filter using 7 mL of HEPES buffer and 0.5 mL of the solution, containing approximately 0.5 mg of NPs, was mixed with 1 mCi of ^{89}Zr and incubated for 2 hours at 37°C. NPs were then added to HEPES buffer to neutralize the reaction and were centrifuged under the same conditions. This method was conducted in triplicate.

3.4.9 Binding efficiency and stability of ^{89}Zr

To determine the binding efficiency of the ^{89}Zr to the NPs, the radioactivity was measured using a dose calibrator from Biodex Medical Systems (Shirley, NY). The radioactivity of the NP pellet, the NPs remaining in initial vial, and the supernatant were all measured to account for all traces of ^{89}Zr. The efficiency was determined by importing the radioactivity of the following samples:

$$Binding\ Efficiency = \left(\frac{Labelled\ ^{89}Zr}{Labelled\ ^{89}Zr\ +\ Free\ ^{89}Zr}\right) x\ 100 \tag{3.4}$$

Stability of ^{89}Zr bound to the NPs was only conducted using the first method. After measuring binding efficiency, the NP pellet was added to HEPES buffer and allowed to stir in 37 °C for 24 hours. The NPs were then collected using the ultra-centrifugation method previously described and the radioactivity was measured. To account for radioactive decay, the radioactivity of the entire solution was measured prior to collection.

3.5 In vitro analysis

GBM43 cells were cultured with DMEM and supplemented with 10% FBS and 1% HEPES buffer. These cells could be seeded for testing in 96-well plates at approximatley 85% to 90% confluency. GBM CSCs were cultured using the Human Glioma Cancer Stem Cells Media described above and could be seeded for testing in 96-well plates at approximately 60% to 80% confluency according to the Celprogen Human Glioblastoma Cancer Stem Cell seeding protocol. Both cell lines were cultured at 37°C in a humidified atmosphere containing 5% carbon dioxide (CO_2).

3.5.1 Determination of optimal cancer stem cell seeding number

Prior to performing cytotoxicity studies of both free drugs and NPs, a cell seeding number for the study in 96-well plates was first optimized. To determine the optimal cell seeding number for CSCs, cells were treated with RG7388. Cells were plated in triplicate at concentrations of 100 cells/well, 50 cells/well, and 25 cells/well and left to culture overnight. Cells were then treated with RG7388 at concentrations of 50 μM, 37.5 μM, 28.13 μM, 21.09 μM, 15.82 μM, 11.87 μM, 8.90 μM, and 6.67 μM. Cytotoxicity was analyzed by the methylene blue assay listed in the following subsection. The dose curves were then compared to determine the optimal cell seeding number.

3.5.2 Determination of IC_{50} Values

To determine the IC_{50} value for each drug, a methylene blue assay determined the cytotoxicity at varying doses. GBM CSCs were plated in a 96-well plate at 25 cells/well in a volume of 100 μL and cultured overnight. Media was adjusted to a series of single drug concentrations as seen in Table 3.3. A vehicle treatment was also used that obtained the maximum DMSO concentration used. DMSO concentration

was maintained ≤0.1% of the total media concentration. In addition, studies were conducted with media controls on each plate.

Table 3.3
Single drug doses

Cell Line	Drug	Doses
GBM43	TMZ (μM)	3400, 1700, 850, 425, 212.5, 106.3, 56.1, 26.6
	PTX (nM)	18.75, 14.06, 7.91, 5.93, 4.45, 3.33, 2.50
CSCs	TMZ (μM)	2000, 1000, 500, 250, 125, 62.5, 31.3, 15.6
	RG7388 (μM)	40, 30, 22.5, 16.9, 12.7, 9.5, 7.1, 5.3
	PTX (μM)	1600, 800, 400, 200, 100, 50, 25, 12.5

Combination treatments were conducted next. TMZ and RG7388 were combined for CSC treatment at ratios of 15:1, 50:1 and 500:1 starting with starting TMZ concentrations of 600 μM, 500 μM and 500 μM, respectively.

Treatment groups of NPs were empty non-targeted NPs, non-targeted TMZ-loaded NPs, non-targeted TMZ+RG7388-loaded NPs, and targeted TMZ+RG7388-loaded NPs in CSCs. The NPs used for in vitro studies were the final formulation of NPs seen in Table 4.3. The highest treatment for each of the four groups contained 714 μg of NPs and were diluted by half for a total of nine treatments.

Cells were incubated with the treatments for five days. After, the media was aspirated and the cells were fixed with 100% methanol for 5 to 10 minutes. Methanol was disposed of and allowed to dry completely. The remaining viable cells were stained with 70 μL 0.05% methylene blue for 30 to 60 minutes. The plates were then shaken into the sink, dipped into deionized water to rinse three times, and the water was flicked out. The remaining water was shaken out onto a paper towel and the plates were allowed to dry completely. Next, 100 μL 0.5M hydrochloric acid (HCl) was added using a multi-channel pipette. The plates were mixed by gently tapping

and read at 600 nm on the plate reader described above. Treatment amounts will be listed with the results, but goal treatment duration was three trials in three different cell populations to account for population differences.

To determine the cytotoxicity, Fa and Fu values were determined by Equation 1.1 and the following:

$$Fa = 1 - (\frac{Abs_{\text{Sample}}}{Abs_{\text{Media}}}) \tag{3.5}$$

These values were then plotted and analyzed in CalcuSyn 2.0 to determine an IC_{50} value.

3.6 Statistics

Unless otherwise stated, experiments were conducted in at least triplicate and a standard error of the mean was used. Statistics were conducted with a confidence value of 95%. A students t-test was used to conduct comparison between groups. All data was analyzed using a two-tailed, unpaired analysis with the assumption of unequal variances. The only test that included a paired analysis was that of the size stability of NPs.

4. RESULTS

4.1 Particle constituent analysis

4.1.1 Determination of 0.5% 13k polyvinyl alcohol viscosity

Viscosity was measured by averaging the values of the instantaneous viscosity after the instrument levelled off at a value for viscosity. These levelled values can be seen in Figure 4.1. An average of the three trials produced a viscosity measurement of $1.59*10^{-7}$ Pa*s or $2.788 \pm 2.37*10^{-5}$ cPs.

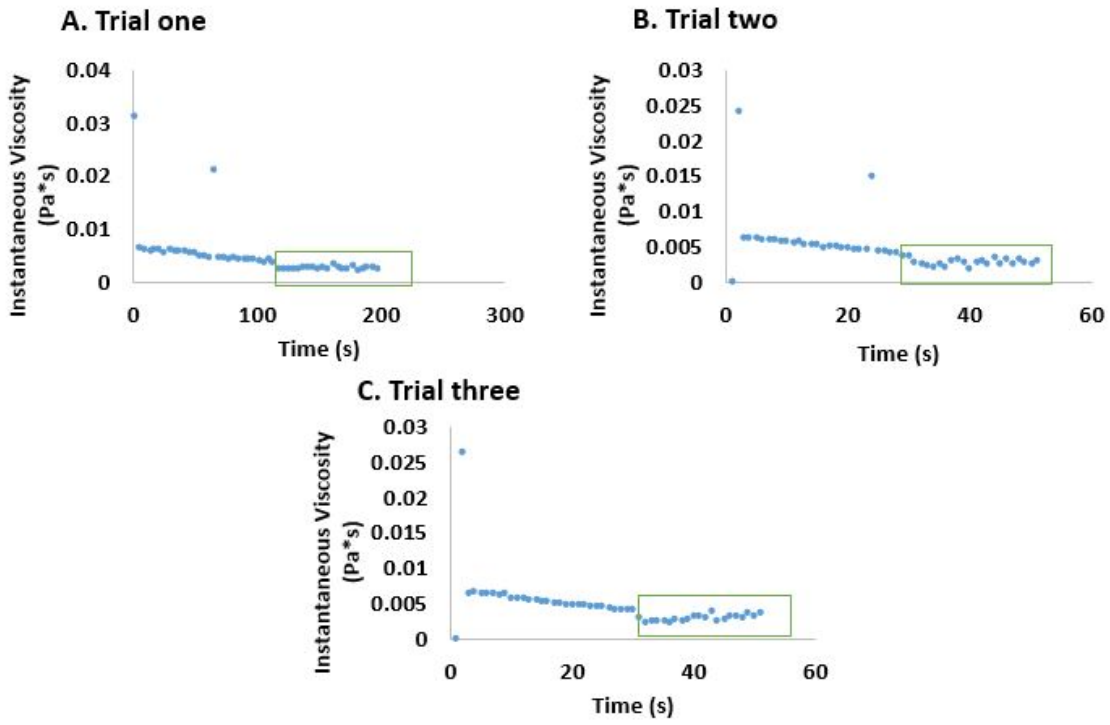

Fig. 4.1 Determination of surfactant viscosity. Above represents the three trials of the measurement of viscosity for 0.5% 13k PVA with a rheometer. The data set that is used in viscosity determination is boxed in green.

4.1.2 Analysis of TMZ by UV-Vis spectroscopy

TMZ in DMSO was analyzed by UV-Vis. For measurement of drug content in single emulsion NPs, a standard curve was made by measuring the absorbance of known TMZ concentrations at 325 nm as seen in Figure 4.2.

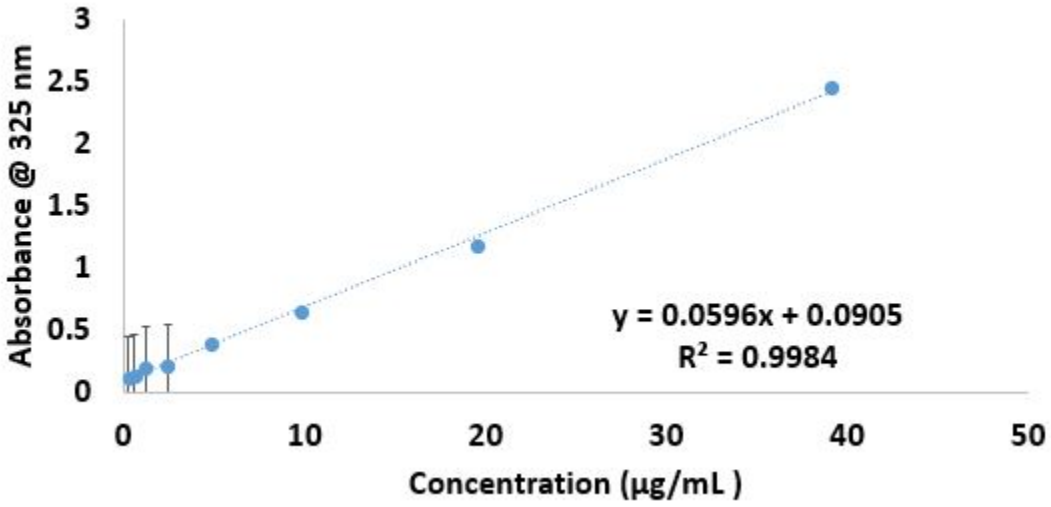

Fig. 4.2 TMZ standard curve at 325 nm. This standard curve was made by UV-Vis spectroscopy and was used for analysis of the drug content in single emulsion NPs.

To determine the maximum wavelength of TMZ in DMSO by UV-Vis, a scan from 270 nm to 380 nm determined that the maximum wavelength of TMZ in DMSO is 332 nm. A standard curve was generated at 332 nm and can be seen in Figure 4.3.

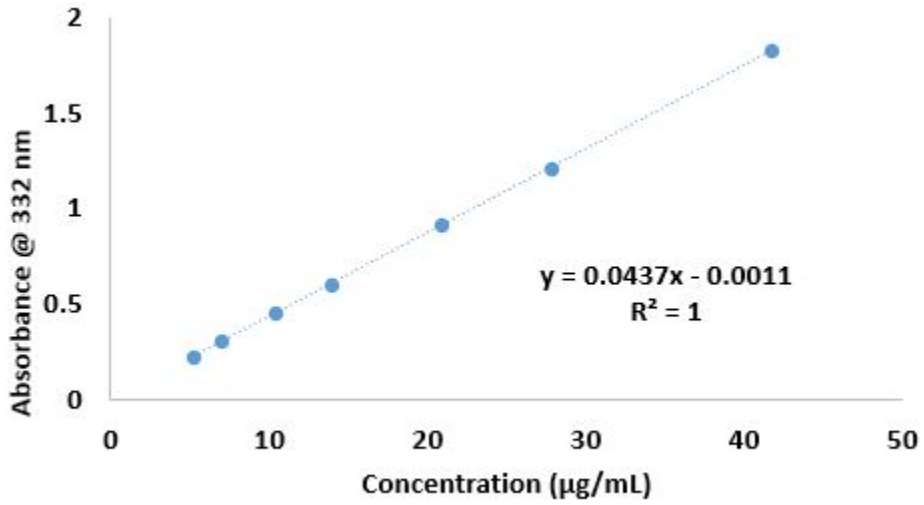

Fig. 4.3 TMZ standard curve at 332 nm. This standard curve was made by UV-Vis spectroscopy and was used for analysis of the drug content in single emulsion NPs.

4.1.3 Analysis of polymers by UV-Vis spectroscopy

To determine if the polymers interfere with analysis by UV-Vis spectroscopy at 332 nm, absorbance scans were measured. It was determined from Figure 4.4 that PS-*b*-PEO has absorbance around the region similar to TMZ, while PLGA does not.

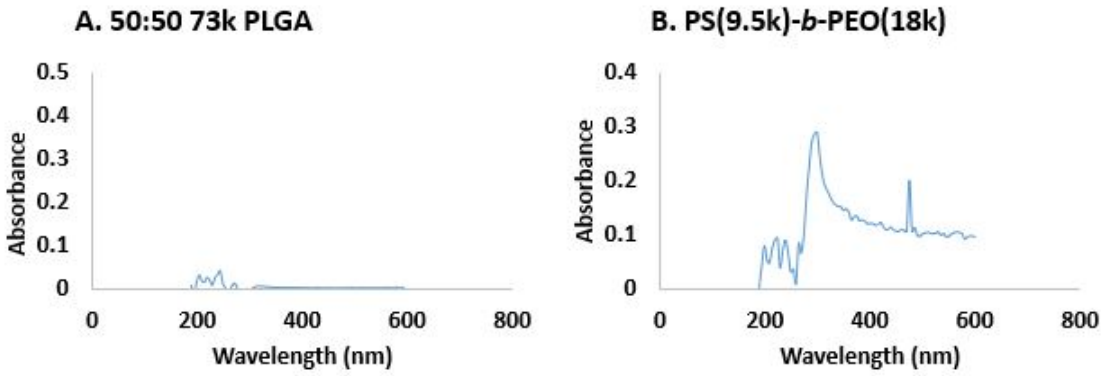

Fig. 4.4 Polymer absorbance scans in DMSO. These polymer scans were conducted by UV-Vis spectroscopy to determine if either 50:50 73k PLGA or PS(9.5k)-*b*-PEO(18k) have absorbance in the same regions as TMZ.

4.1.4 TMZ stability

Scans of TMZ at various pH of aqueous solutions were analyzd by UV-Vis over time. These scans can be seen in Figure 4.5. The slopes from these curves in order of increasing pH are -0.0037 nm per day, -0.0057 nm per day and -0.0077 nm per day.

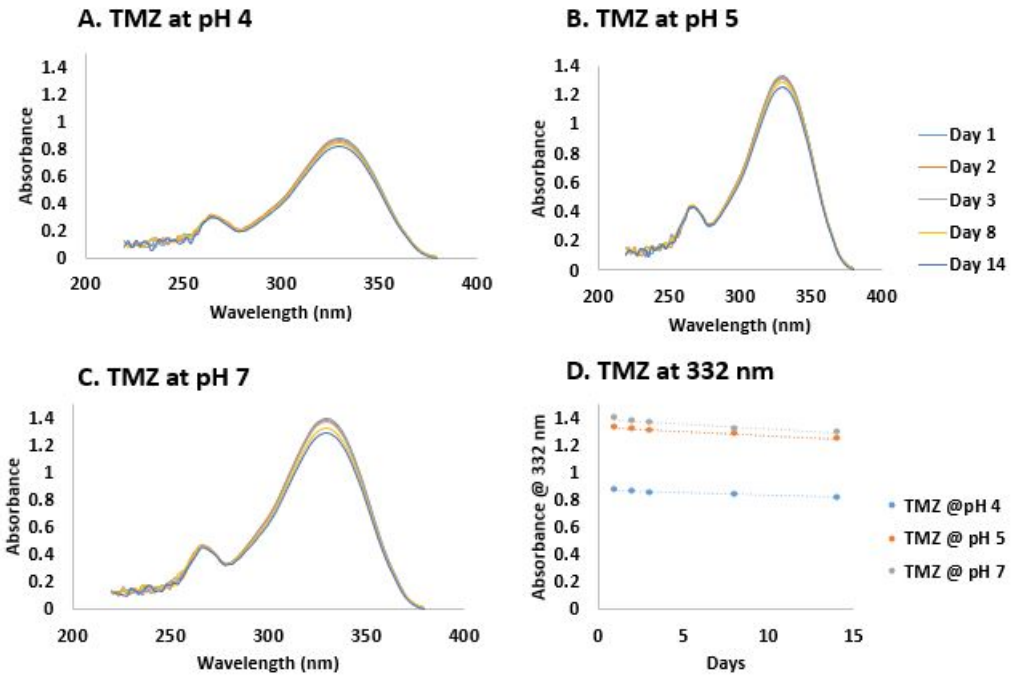

Fig. 4.5 The above figure represents the stability of TMZ at pH 4 (A), pH 5 (B), pH 7 (C), as well as a linear regression at maximum absorbance of 332 nm (D).

4.1.5 Method determination for HPLC drug analysis

Two different methods were investigated to separate TMZ from RG7388 and TMZ from PTX. For the first isocratic method, the release times for the TMZ, RG7388 and PTX were approximately 3.00 min, 1.81 min, and 4.10 minutes respectively. The release times for the three drugs using the second method were approximately 3.09, 6.31 and 3.48 minutes, respectively. The final method used for drug quantification shortened the release times of TMZ and RG7388 to 1.9 minutes and 3.8 minutes respectively while a baseline was established between the two drugs. TMZ eluted with a sharp peak and RG7388 eluted with a much broader peak (Figure 4.6). The top portion of the figure shows how TMZ releases with a reference wavelength of 332 nm. The bottom half of the figure shows that TMZ can be seen at the same time

with a reference wavelength of 273 nm, but is at a much lower intensity. RG7388 could only be detected with the reference wavelength of 273 nm.

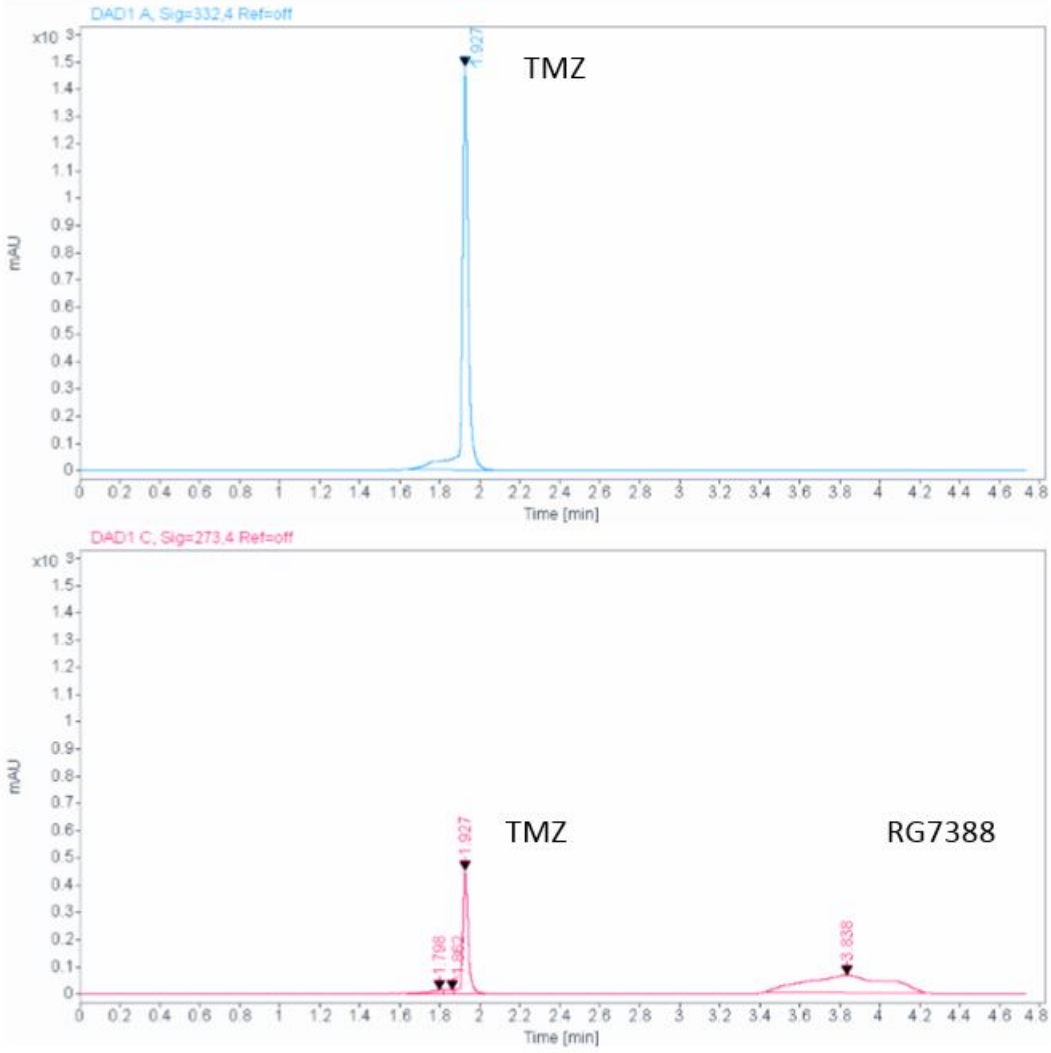

Fig. 4.6 HPLC of TMZ and RG7388. The above figure represents the separation of TMZ and RG7388 via HPLC. After TMZ ellutes the baseline is established and RG7388 ellutes.

4.2 Single emulsion nanoparticles

4.2.1 Size, charge, and PDI by dynamic light scattering

During the first experiments, TMZ-loaded NPs were made with PS(5k)-*b*-PEO(2.2k). Drug-loaded polymer-micellar NPs with this micelle component had approximate volume distributed hydrodynamic diameters of 152 nm after two trials. After, single emulsion NPs were made with PS(9.5k)-*b*-PEO(18k) and led to a significant decrease in size for TMZ-loaded NPs to 66 nm. Data acquired from DLS measurements for single emulsion NPs can be seen in Table 4.1. There was a significant increase in size when comparing empty polymer-micellar particles and empty PLGA particles. There was also a significant increase in size when TMZ was added into the particles and again when RG7388 was added into the particles. There was a significant decrease in PDI when comparing empty micelles to empty polymer-micellar NPs. When comparing zeta-potential measurements, there was a significant decrease in charge when PLGA was included into the particles as zeta-potential decreased from -9.5 mV to -29.5 mV.

Table 4.1
PDI and Zeta-Potential Values of Single-Emulsion Particles

Particle Description	Size (nm)	PDI	Zeta-Potential (mV)
PS-*b*-PEO (control)	22±10	0.385	-9.5 ±1.0
PS-*b*-PEO + PLGA (no drug)	49±1	0.222	-29.5±0.9
PS-*b*-PEO + PLGA + TMZ	66±2	0.204	-20.4±1.1
PS-*b*-PEO + PLGA + TMZ + RG7388	259±3	0.188	N/A
PLGA (control)	221±0	0.155	-20.4±1.1

4.2.2 Transmission electron microscopy

TEM was used to determine the morphology of the NP samples. Figure 4.7 displays images of blank PS-*b*-PEO micelles (A) and PS-*b*-PEO + PLGA polymer micelle NP (B). Next the morphology of the drug-loaded NPs was analyzed and

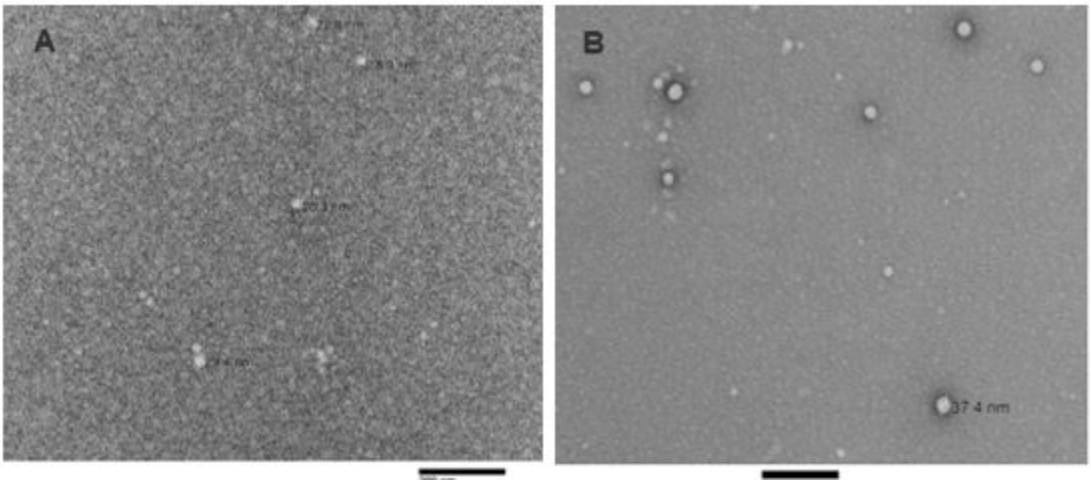

Fig. 4.7 Representative TEM images of PS-*b*-PEO micelles (A) and PS-*b*-PEO + PLGA polymer micelle NPs (B). Each mag bar correlates to the above image and is 200 nm.

representative images of TMZ-loaded NPs (A) and TMZ+RG7388-loaded NPs (B) are shown in Figure 4.8.

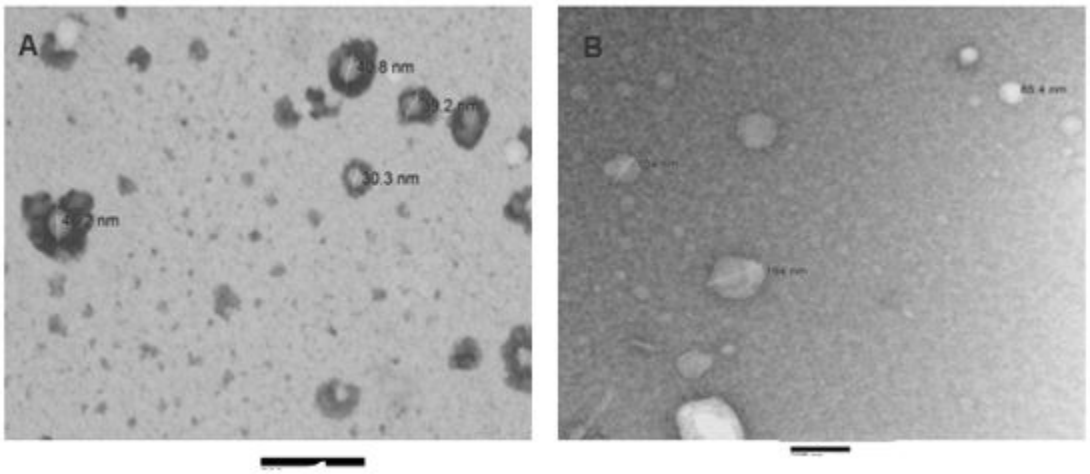

Fig. 4.8 Representative TEM images of TMZ-loaded NPs (A) and TMZ+RG7388 NPs (B). Each mag bar correlates to the above image and is 200 nm.

4.2.3 Drug encapsulation and drug-loading percentage by UV-Vis spectroscopy

The TMZ-loaded NPs were investigated by UV-Vis spectroscopy to determine the amount of TMZ in the NPs. First, a standard curve for TMZ at 325 nm was determined (Figure 4.2). This resulted in a linear equation of y=0.0596x+0.0905. Three samples of NPs resulted in an average encapsulation efficiency of 0.03% and a negligible drug-loading percentage.

4.3 Double emulsion nanoparticles

4.3.1 Size, charge, and PDI by dynamic light scattering

Size and PDI were measured by DLS and are reported in Table 3.1. These results are the sizes and PDI values that are associated with the initial formulation development stages for double emulsion NPs. Size was determined by an average volume distribution. The table labels correlate to the table in the methods where each letter

description has a particle formulation that is further detailed above. Because the viscosity value of water was used during measurement of DLS, these results are unable to be compared statistically or to the final formulation. However, sizes between the groups can be compared. It was determined that increasing the concentration of the PVA surfactant, results in a decrease in hydrodynamic diameter and reduction of PDI. In addition, swapping PVA for F-68 resulted in an increase in particle size. An increase in sonication time slightly reduces the size of NPs, but might not have a great effect. In addition, the use of Tween in the organic layer did not reduce the size of the particles, but reduced the PDI.

Table 4.2
Size and PDI Values of Initial Formulation Double-Emulsion Particles

Particle Description	Size (nm)	PDI
A	195±9	0.103
B	380±4	0.111
C	142±7	0.179
D	141±15	0.086
E	263±6	0.128
F	204±6	0.127
G	210±4	0.108
H	225±11	0.152
I	210±11	0.211
J	207±2	0.161
K	169±13	0.185

A final formulation of NPs was selected by choosing the smallest size and a size that was less than 100 nm set by the initial size objective. These results were conducted after the initial formulation development in the preceding paragraph and were used for the rest of the thesis work. Characteristics of these NPs can be seen in Table 4.3

to accomplish our first objective (Figure 2.1.1). Empty polymer-micellar NPs had a size of 95 nm and there was a significant decrease in size to 82 nm upon the addition of TMZ. When both RG7388 and PTX were loaded into the NPs, there was not a significant change in size. There was a significant decrease in zeta-potential from -7.1 mV to -9.9 mV when RG7388 was added into the TMZ-loaded NPs.

Table 4.3
Characteristics of final double emulsion NP formulation

Particle Description	Size (nm)	PDI	Charge (mV)
PS-*b*-PEO+PLGA-NHS/PLGA-NH_2	95±3	0.126	-8.0±1.0
PS-*b*-PEO+PLGA-NHS/PLGA-NH_2+TMZ	82±3	0.175	-7.1 ±0.4
PS-*b*-PEO+PLGA-NHS/PLGA-NH_2+TMZ+RG7388	87±2	0.138	-9.9±0.7
PS-*b*-PEO+PLGA-NHS/PLGA-NH_2+TMZ+PTX	83±6	0.140	-9.7±1.9

4.3.2 Size and PDI stability of NPs

TMZ-loaded PS-*b*-PEO+PLGA-NHS/PLGA-NH_2 NPs were measured over time to determine size and PDI stability. Size increased over time, but there was only a significant increase of size between 0 and 24 hours. PDI did not show a trend and there was no significant change.

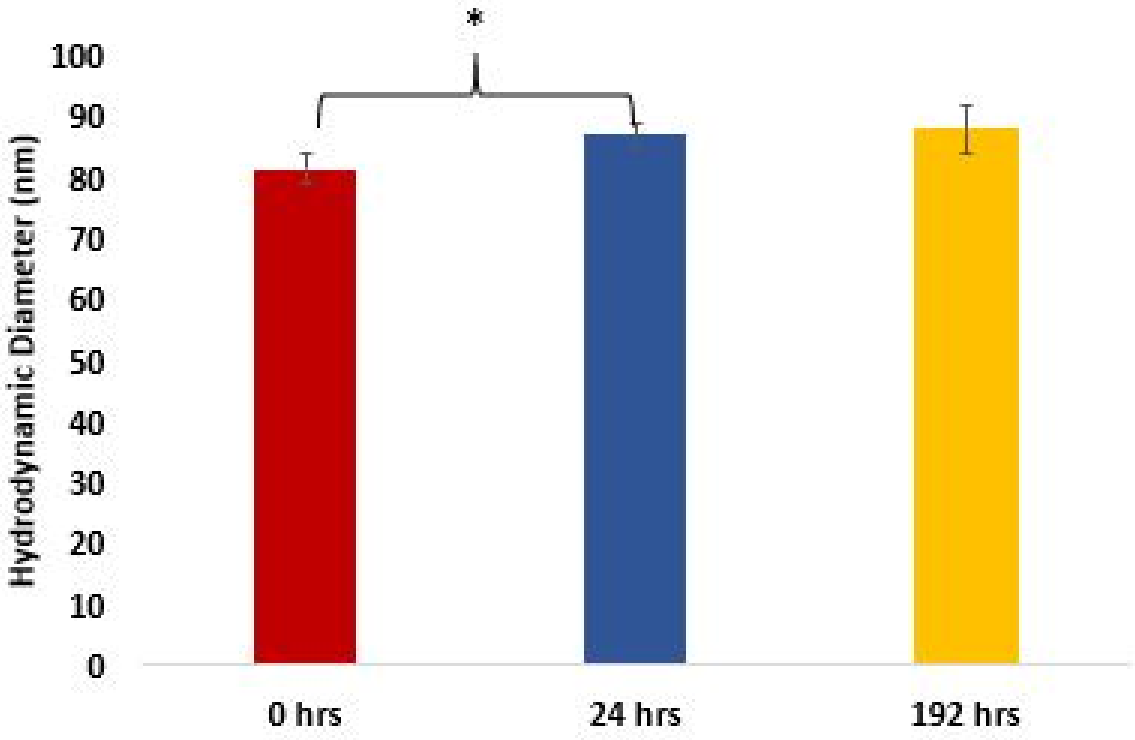

Fig. 4.9 Size stability of NPs over time. Size of NPs were measured at each time point. Each bar corresponds with the PDI results seen in Figure 4.10. Significance is represented by an (*).

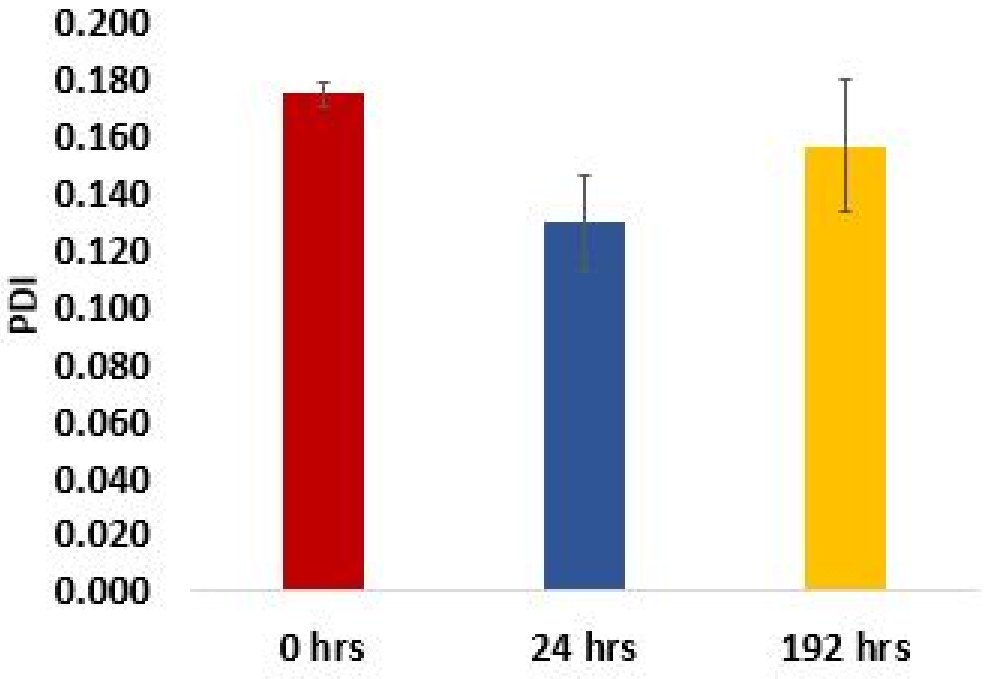

Fig. 4.10 PDI stability of NPs over time. PDI of NPs were measured at each time point. Each bar corresponds with the size results seen in Figure 4.9.

4.3.3 Transmission electron microscopy

TEM was used to determine the morphology of the NP samples. Figure 4.11 displays representative images of the empty and TMZ-loaded double emulsion PS-*b*-PEO+PLGA nanoparticles prepared with functional PLGA in the form of PLGA-NHS and PLGA-NH_2. Next the morphology of the dual drug-loaded NPs were analyzed and representative images of TMZ+RG7388-loaded NPs (A) and TMZ+PTX-loaded NPs (B) are shown in Figure 4.12.

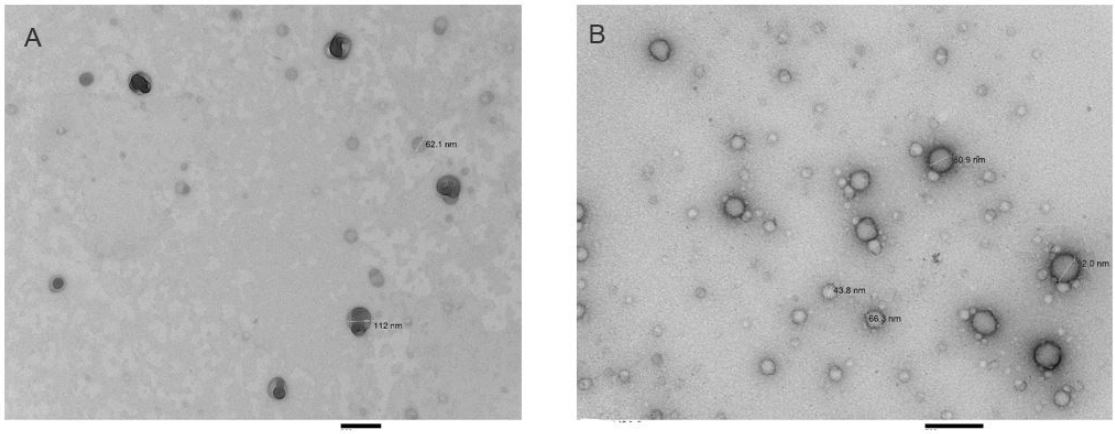

Fig. 4.11 TEM images of control and TMZ-loaded NPs. Above are representative TEM images of empty functional NPs (A) and TMZ-loaded functional NPs fabricated by a double emulsion protocol (B). Each mag bar correlates to the above image and is 200 nm.

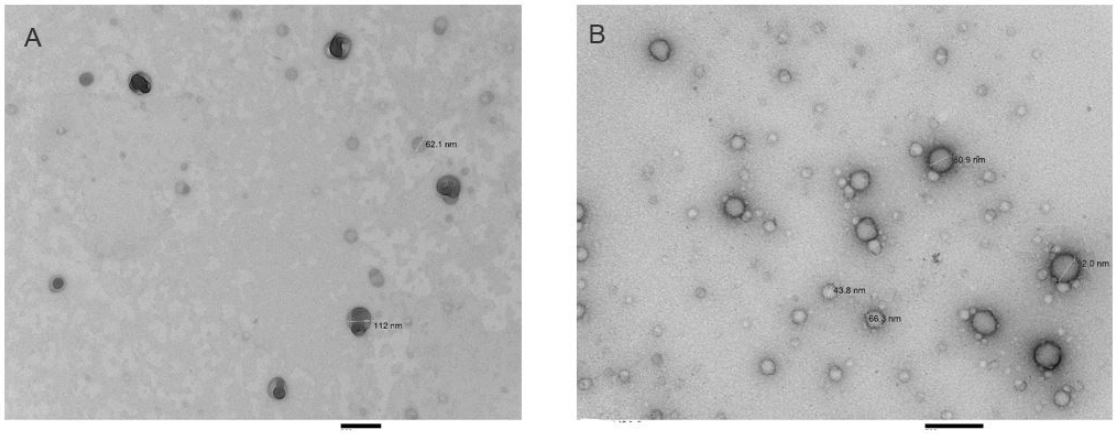

Fig. 4.12 TEM images of TMZ+RG7388 NPs and TMZ+PTX NPs. Above are representative TEM images of TMZ+RG7388-loaded NPs (A) and TMZ+PTX-loaded NPs (B). Eahc mag bar correlates to the above image and is 200 nm.

4.3.4 Drug encapsulation and drug-loading percentage by UV-Vis spectroscopy

Double emulsion NPs containing 50:50 PLGA-NHS/PLGA-NH_2 were investigated initially by UV-Vis to see the potential increase in TMZ encapsulation compared to the single emulsion method. The NPs had an EE% of 14.20%±3.23% and a DL% of 1.17%±0.46%.

4.3.5 Drug encapsulation and drug-loading percentage by HPLC

Encapsulation efficiency and drug loading percentage were confirmed by HPLC because of the increased sensitivity over UV-Vis spectroscopy to achieve our second objective (Figure 2.1.2). A method to separate TMZ and RG7388 was successfully developed. A representative standard curve for each drug can be seen in Figure 4.13. By HPLC, the encapsulation efficiency and drug loading percentage of TMZ-loaded NPs was determined to be 4% ±6.7 and 0.12% ±0.19, respectively. For TMZ+RG7388-loaded NPs, the encapsulation efficiency was 1.6% for TMZ and 52.8% for RG7388. The drug loading percentage was 0.07% for TMZ and 0.66% for RG7388.

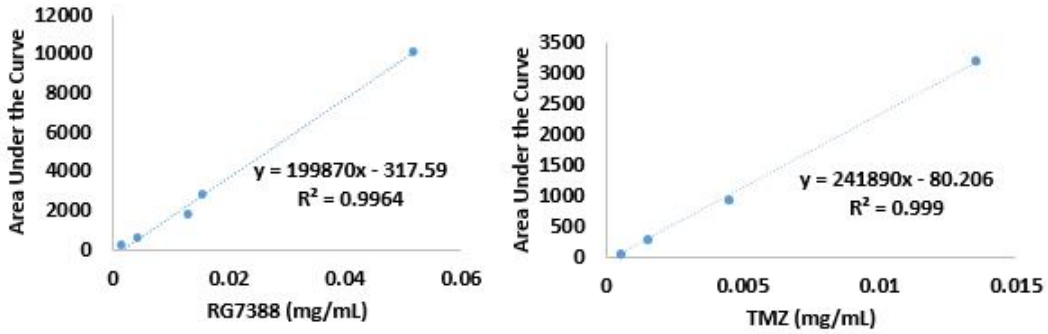

Fig. 4.13 The above figure contains a representative standard curve for determining the concentration of RG7388 (left) and TMZ (right) by HPLC.

4.3.6 Conjugation of CD133 aptamer

The aptamer was bound to the NPs and achieved a conjugation efficiency of 86.3% ± 7.4%. This was conducted to achieve our third objective (Figure 2.1.3) The EMSA assay was the first method used to determine if the NPs were stably bound to the NPs. According to Figure 4.14, the free aptamer and aptamer conjugated NPs all shifted approximately the same distance. Once the aptamer was conjugated to TMZ+RG7388-loaded NPs, the size of the NPs were 85±3 nm (n=2). In addition, these NPs had a PDI of 0.113±0.011. These final NPs had a zeta-potential of -25.3±0.3 mV. This zeta-potential was significantly more negative than the TMZ+RG7388-loaded NPs without the conjugated aptamer.

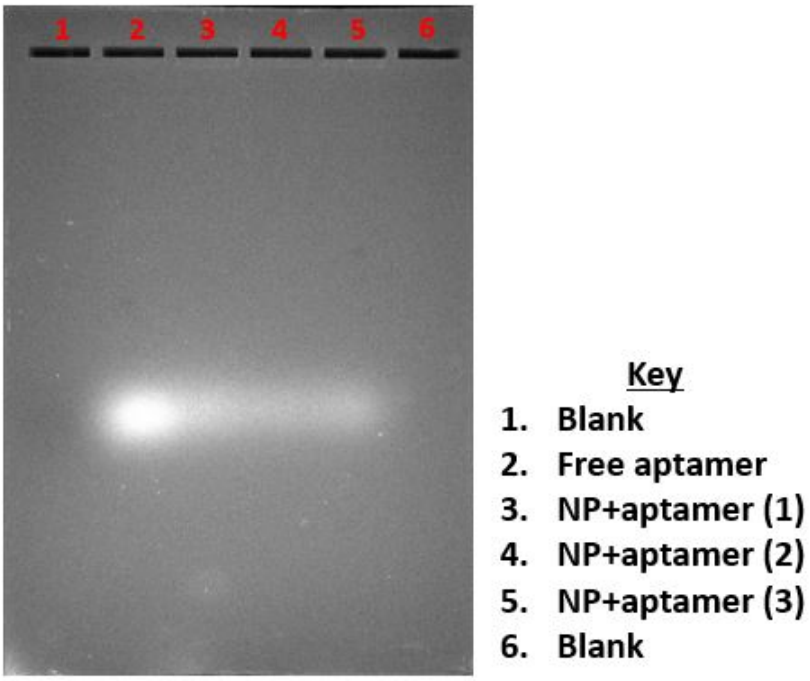

Fig. 4.14 EMSA assay for aptamer bound to NPs. The above figure represents the EMSA assay for NPs bound to aptamers.

The stability of the binding of the aptamer to the NPs was analyzed over a course of 24 hours. The binding efficiency decreased from 94% to 68% within one hour of

conjugation. After 3 hours, the binding efficiency was about 50%. From the 3 hour time point to the end of the 24 hours, the binding efficiency increased to 70%.

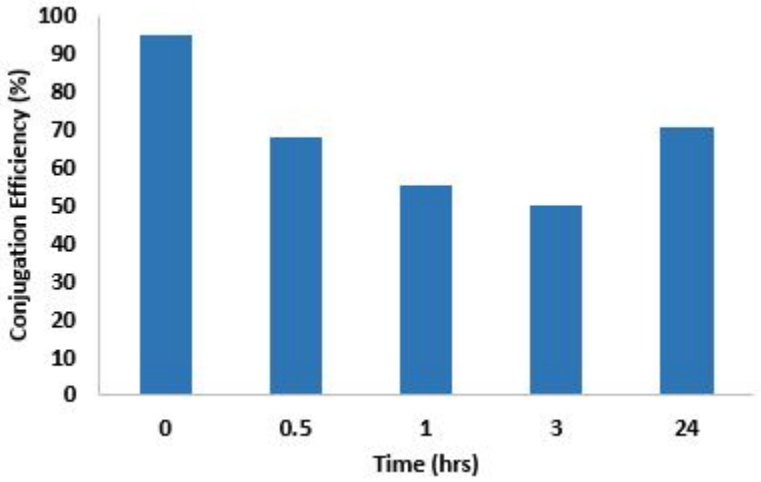

Fig. 4.15 Aptamer stability. The above figure represents the stability of the conjugated aptamer at 37 °C over a course of 24 hours.

4.3.7 Conjugation of ^{89}Zr

The first method to conjugate ^{89}Zr to the NPs had a labeling efficiency of 29% ± 2.56% and an average radioactivity of 158.5 μCi. After 24 hours, approximately 46.8% ± 1.6% of the ^{89}Zr released from the NPs. The second method achieved a significant decrease in binding efficiency to 14% ± 0.9% with an average radioactivity of 127.7 μCi. This was conducted to achieve our fourth objective (Figure 2.1.4).

4.4 In vitro analysis

4.4.1 Single drug analysis

TMZ and RG7388 single drug analysis was conducted with an n=3 in three different cell populations to achieve one part of our fifth objective (Figure 2.1.5). Dose

response curves can be seen in Figure 4.16. The Fa and Fu values from these dose responses can be seen in Table 4.4. These Fa values were plotted using a logarithmic analysis to determine the most linear region. These plots can be seen in Figure 4.17. These most linear regions were entered into CalcuSyn 2.0 and produced an IC_{50} value for TMZ was determined to be 270.02 μM with a lower 95% confidence limit of 214.64 μM and an upper confidence limit of 339.69 μM. The IC_{50} for RG7388 was determined to be 16.14 μM with a lower 95% confidence limit of 14.58 μM and an upper confidence limit of 17.86 μM.

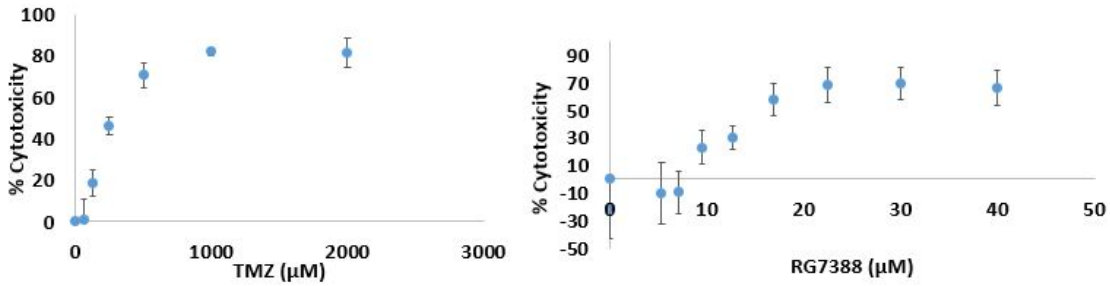

Fig. 4.16 TMZ and RG7388 alone in CSCs. The above figure represents the analysis of single drugs in glioma CSCs. The left represents the dose curve from TMZ alone and the right represents the dose curve of RG7388 alone.

Table 4.4
Single Drug Dose Responses

TMZ			RG7388		
Dose	Fa	Fu	Dose	Fa	Fu
0	0	1	0	0	1
15.63	-0.12	1.12	5.34	-0.10	1.10
31.25	-0.18	1.18	7.12	-0.09	1.09
62.5	0.01	0.99	9.49	0.23	0.77
125	0.19	0.81	12.66	0.30	0.70
250	0.46	0.54	16.88	0.58	0.42
500	0.71	0.29	22.5	0.68	0.32
1000	0.82	0.18	30	0.69	0.31
2000	0.82	0.18	40	0.66	0.34

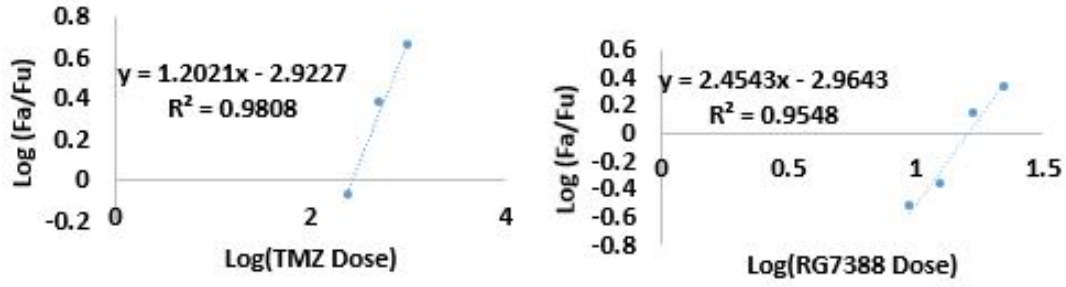

Fig. 4.17 Linear plots for TMZ and RG7388 dose responses. The left represents the most linear region from the TMZ dose response curve. The right represents the most linear region from the RG7388 dose response curve.

A PTX dose curve was conducted with an n=3 in one cell population. This dose curve can be seen in Figure 4.18. An IC_{50} value was not determined for this drug, but can be estimated as approximately around 100 nM.

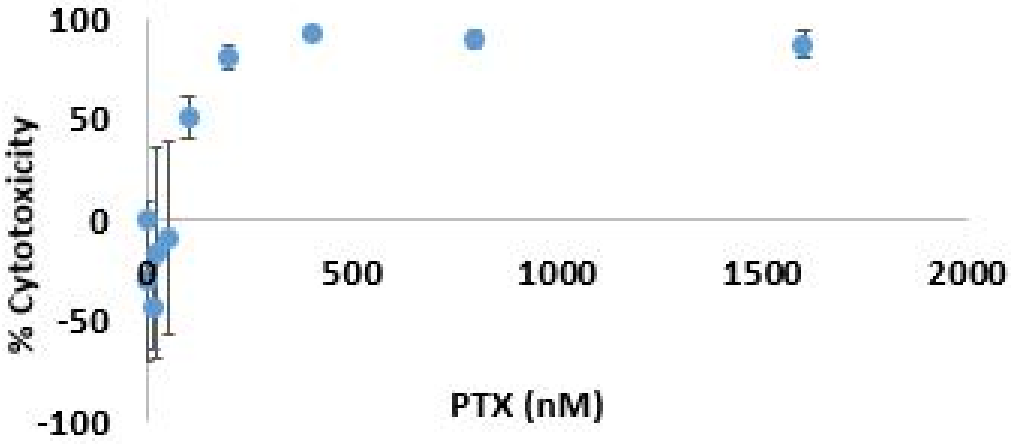

Fig. 4.18 PTX dose curve in CSCs.

A TMZ dose curve was conducted with an n=3 in three cell populations of GBM43 cells. This dose curve can be seen in Figure 4.19. This was unable to be analyzed via CalcuSyn, but produced an approximate IC_{50} value of 338 μM. A PTX dose curve was conducted with an n=3 in four cell populations of GBM43 cells. This dose curve can be seen in Figure 4.19. This was unable to be analyzed via CalcuSyn, but produced an approximate IC_{50} value of 11 nM.

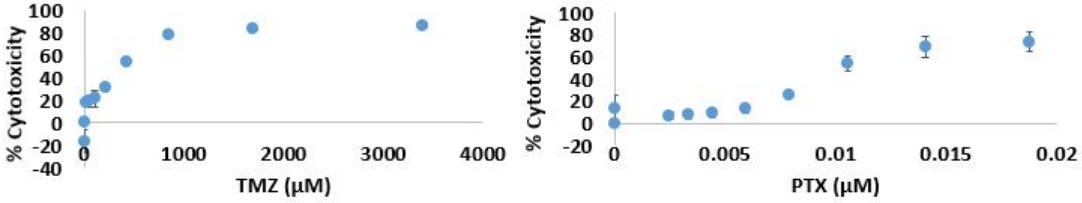

Fig. 4.19 TMZ and PTX single drug dose curve in GBM43 cells.

4.4.2 Combination drug analysis

TMZ and RG7388 was given in combination to the CSCs. Ratios of RG7388 to TMZ that were 1:15 and 1:100 were analyzed with an n=3 in three different cell populations. The ratio of 1:50 was only given to an n=3 in one population.

Table 4.5
Combination Drug Dose Responses

Ratio of 1:15		Ratio of 1:50		Ratio of 1:100	
TMZ (μM)	Fa	TMZ (μM)	Fa	TMZ (μ)	Fa
0	-0.23	0	-0.01	0	0.13
4.69	-0.16	3.91	0.19	3.91	0.19
9.38	0.10	7.81	0.08	7.81	0.15
18.75	0.16	15.63	-0.06	15.63	0.28
37.5	0.11	31.25	0.33	31.25	0.14
75	0.34	62.5	0.42	62.5	0.29
150	0.59	125	0.75	125	0.50
300	0.81	250	0.89	250	0.65
600	0.86	500	0.86	500	0.74

These combinations were analyzed using CalcuSyn 2.0 and 50% effective doses (ED50) were determined. These doses were the combination of TMZ and RG7388 that produced 50% killing in CSCs. At a ratio of 15, the ED50 is when TMZ is at a concentration of 122.48 μM. At a ratio of 50, the ED50 is when TMZ is at a concentration of 82.83 μM. Finally, at a ratio of 100, the ratio is when TMZ is at a concentration of 153.57 μM. To determine synergy, CalcuSyn 2.0 ran CI simulations at predicted cell responses. These simulations can be seen in Table 4.6. The IC_{50} values were plotted and compared to the effect of the drugs alone. This isobologram in Figure 4.20 shows an additive effect when RG7388 and TMZ are in a molar ratio of

1:15 and synergistic effects when the two drugs are in molar ratios of 1:50 and 1:100. This parallels the CI values that were simulated.

Table 4.6
Combination indexes for TMZ and RG7388 in CSCs

Fa	CI for Ratio of 1:15	CI for Ratio 1:50	CI for Ratio 1:100
0.02	1.058	0.820	0.245
0.05	0.994	0.677	0.308
0.10	0.961	0.586	0.369
0.15	0.948	0.538	0.414
0.20	0.942	0.505	0.453
0.25	0.940	0.481	0.487
0.30	0.939	0.461	0.520
0.35	0.940	0.444	0.552
0.40	0.942	0.429	0.584
0.45	0.945	0.415	0.617
0.50	0.950	0.403	0.652
0.55	0.955	0.391	0.688
0.60	0.962	0.380	0.728
0.65	0.970	0.369	0.773
0.70	0.980	0.358	0.825
0.75	0.993	0.347	0.886
0.80	1.011	0.335	0.964
0.85	1.035	0.322	1.069
0.90	1.073	0.307	1.232
0.95	1.150	0.289	1.565
0.99	1.393	0.266	2.792

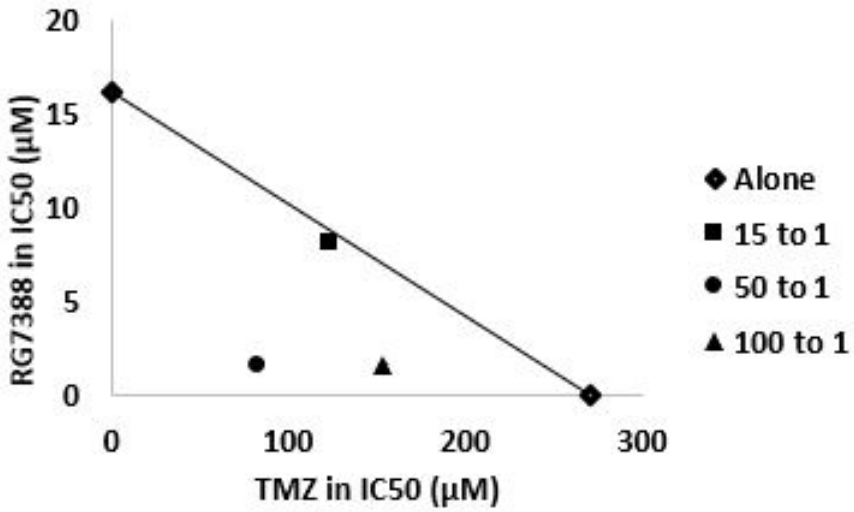

Fig. 4.20 Isobologram of TMZ and RG7388 in CSCs. GBM CSC growth was inhibited when exposed to TMZ in combination with RG7388. RG7388 to TMZ at ratios of 1:50 and 1:100 produced a synergistic effect. Ratio of 1:15 produced an additive effect.

4.4.3 Analysis of treatment with NPs

CSCs received treatments of empty polymer-micellar NPs, TMZ-loaded NPs, TMZ+RG7388-loaded NPs and TMZ+RG7388-loaded NPs conjugated to the anti-CD133 aptamer as the second part of our fifth objective (Figure 2.1.5). Dose curves for empty NPs and TMZ-loaded NPs can be seen in Figure 4.21. These two sets of NPs had minimal cytotoxic effect on the CSCs. Dose curves for dual-drug loaded NPs and dual-drug loaded NPs can be seen in Figure 4.22. These dose curves were unable to be analyzed by CalcuSyn 2.0. However, a similar analysis was conducted to determine an approximate IC_{50} value. Dual-drug loaded NPs had an IC_{50} value of the TMZ concentration of 14.26 μM. The addition of the targeting agent somewhat lowered the IC_{50} value to a TMZ concentration of 11.86 μM.

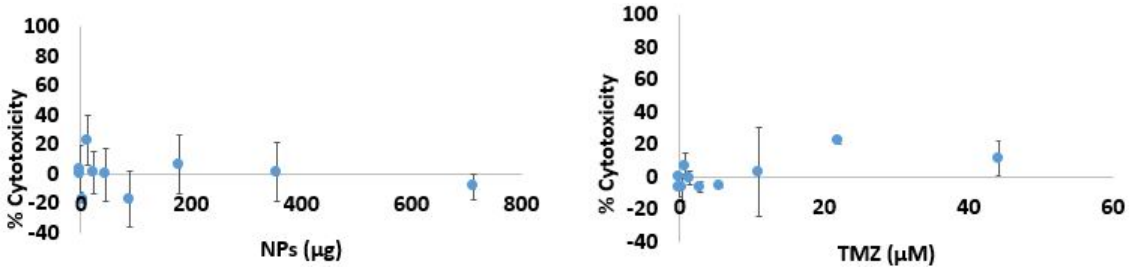

Fig. 4.21 Empty and TMZ-loaded NPs in CSCs. Above represents the dose curves generated from empty polymer-micellar NPs (left) and TMZ-loaded NPs (right). The mass of NPs is the same in each dose curve.

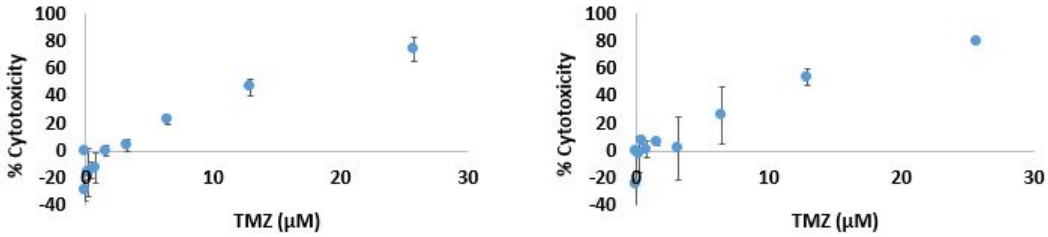

Fig. 4.22 TMZ+RG7388-loaded NPs and targeted TMZ+RG7388-loaded NPs in CSCs. Above represents the dose curves generated from dual-drug NPs (left) and dual-drug NPs conjugated to the anti-CD133 aptamer (right).

5. DISCUSSION

The quest for a cure for GBM has been disappointing since no new drug has significantly impacted patient survival in more than fifteen years [1]. A one disease, one drug approach is unlikely to be a viable option given the high propensity of GBM for recurrence, which is at least partially driven by the highly resistant subpopulation of self-regenerating GBM CSCs [34] [35]. NPs hold great promise for overcoming the limitations of a single drug approach by permitting multi-drug combinations that treat GBM synergistically. In addtion, NPs open the door to utilizing the unique advantages of theranostics since the therapeutic agent can be assessed using an imaging label [72]. The goal of this thesis was to establish the building blocks of a multi-drug therapeutic approach that could systematically dismantle GBM by preferentially targeting and overriding the intrinsic TMZ resistance of GBM CSCs. In addition, we sought to integrate an imaging label that would permit a fully theranostic approach to GBM. We hypothesized that hybrid functionalized PS-*b*-PEO and PLGA NPs could be harnessed to encapsulate two different chemotherapies, TMZ and RG7388, to kill human derived GBM CSCs in a dose dependent manner in vitro. We also hypothesized that a 15 nucleoside CD133 aptamer could be covalently bound to our dual-drug loaded PS-*b*-PEO-PLGA NPs to selectively target the CD133 antigen on the CSC surface. Third, we hypothesized that chelative binding of the ^{89}Zr radiotracer to the surface of the NPs would establish a theranostics application for in vivo PET biodistribution studies. Finally, we set a definitive goal to maintain a size of less than 100 nm and acceptable polydispersity to the final dual-drug loaded, functionalized NP.

We made steady progress in addressing our first hypothesis by constructing PS-*b*-PEO and PLGA NPs that encapsulated both TMZ and RG7388. Our original goal had been to maintain a size of 25-50 nm consistently published by our collaborators from Ohio State (Jessica Winters, Ph.D.) [58].

We achieved close to 50 nm size, but only during the production of NPs without drugs and without functional groups. As we added more components to the NPs in a stepwise fashion, the NPs increased in size above 50 nm, but our final NPs with two drugs and two functional groups stayed below 100 nm. This accomplished our first objective (Figure 2.1.1). This is in contrast to dual drug-loaded mPEG-PLA NPs also encapsulating two drugs (TMZ and PTX), but with a 200 nm size [71]. It is possible that our hybrid approach using both micelles and polymer improved the size of the NPs compared with traditional polymer PLGA particles [58] [73]. In the process of optimizing drug encapsulation, we discovered that a double emulsion technique modified from Xu et al., permitted dual-encapsulation with both TMZ and RG7388 more efficiently than a single emulsification as reported in the literature [58] [20]. As shown in the results, we reduced the size of dual-drug loaded NPs from 260 nm down to 85 nm using this technique. Other published studies utilized sizes of NPs of 275 nm, 300-500 nm, and 206 nm [74] [75] [71]. These results may have been influenced by use of polymer components consisting of PLGA-PEG-PLGA, PCL, and PLGA-mPEG [74] [75] [71]. While NPs fabricated by a double emulsification technique typically result in larger sizes, others have achieved a size as small as 40 nm when co-loading 5-fluorouracil and Chrysin into PLGA-PEG-PLGA NPs [76]. During the production of NPs, we consistently maintained a PDI of 20% or less which is desirable since lower polydispersity indicates a more uniform size distribution [77]. As for charge, we also achieved a slightly negative charge for dual drug-loaded particles, except during addition of the CD133 aptamer, which decreased the zeta-potential from -8 mV to -25 mV. While the ideal charge is not known, there is a general consensus that a neutral or slightly negative charge neither repulses the cell membrane nor binds it too tightly [51]. Finally, dual-drug PS-*b*-PEO+PLGA NPs exhibited a consistent spherical morphology when analyzed by TEM and revealed a low level of clumping even with longer duration in solution. Particles with a more spherical shape can potentially result in better cell uptake compared to cylindrical particles as well as increased circulation time [78]. With successful construction of

TMZ+RG7388 NPs, we sought to assess these NPs compared with blank control NPs and NPs containing only TMZ. We first demonstrated synergistic killing of CSCs using combination therapy of TMZ and RG7388, through an analysis of the CI outlined by the Chou-Talalay method, without using NPs first. Through these results we determined a reduction in the IC_{50} value of TMZ from 270 μM when treating CSCs alone, to 83 μM when in combination with RG7388 at a molar ratio of 50:1. A prior published study from our collaborator (Dr. Karen Pollok) demonstrated a synergistic effect between TMZ and RG7388 in the human derived GBM10 cell line, but to our knowledge, the GBM CSC population has not been treated with this drug combination [37]. We demonstrated that dual-drug loaded NPs produced a higher killing effect than empty NPs and TMZ-loaded NPs to acheive our fifth objective (Figure 2.1.5).

Following our initial cell killing studies with non-targeted NPs, we next sought to address our second hypothesis to develop the CD133 aptamer binding to the TMZ+RG7388 NPs. We achieved a high conjugation efficiency of 86% with the fluorescently-labelled CD133. This accomplished our third objective (Figure 2.1.3). We attempted to validate these stability results using an EMSA. Although the NPs are much larger in size compared to the aptamer, charge also influences the degree to which the compounds will migrate. Both free aptamer and aptamer bound to the NPs travelled the same distance approximately 60% from the starting point creating a single well-defined band without a gradient in the EMSA study. Dissociation of CD133 aptamer from the NPs would produce a non-uniform gradient. A single preliminary study of the stability of CD133 aptamer binding to the NPs revealed 50% aptamer remained bound to the NPs at 3 hours and 60% still bound at 24 hours. These results are difficult to interpret since the experiment was performed only once and needs to be replicated in future trials.

To address the second part of hypothesis two, we sought to demonstrate superior CSC killing with TMZ+RG7388+CD133 NPs compared with TMZ+RG7388 NPs without CD133. There was a trend towards a lower IC_{50} value in CD133 aptamer-

bound NPs compared to those without the CD133 aptamer. Future in vitro and in vivo studies need to be conducted to assess the potential advantages of the CD133-labelled NPs.

Time limited full development of our third hypothesis, but we performed three trials of labeling the NPs with ^{89}Zr using two different methods. In the first method we incubated the NPs in a DFOM solution for 40 minutes and labelled with ^{89}Zr for one hour to achieve 30% labelling. To try to improve labeling, we incubated the NPs in the DFOM solution overnight and labelled with the ^{89}Zr for two hours. Our first method achieved a higher amount of ^{89}Zr labelled to the NPs and had a final radioactivity of 158 μCi on 1.5 mg of NPs. For future in vivo studies, this technique will need to be optimized to meet the 250 μCi minimum in each dose of NPs for our current Indiana University IndyPET preclinical system. These initial steps will help us further acheive our fourth objective (Figure 2.1.4).

One of the main challenges of this work was with the first hypothesis in the development of dual drug-loaded NPs. Encapsulation efficiency of TMZ in the NPs was low, but is higher than reported in the literature. One study extensively analyzed a variety of ways to improve the encapsulation of TMZ and achieved a maximum of 2% encapsulation [20]. To overcome this challenge, a series of studies were conducted to understand the stability and optimal environments for using TMZ in the development of NPs. Even with extensive analysis of TMZ, we were unable to encapsulate TMZ to a clinically relevant concentration as seen by the negligent killing in TMZ-loaded NPs. However, even though the encapsulation of TMZ is low in the dual-drug NPs we are unable to say it does not increase the cytotoxicity in combination with RG7388 until we conduct combination studies at that ratio. Future studies could test delivery of TMZ orally as part of standard therapy, and then deliver two different drugs more feasibly encapsulated into the NPs. Such a system would allow a three drug approach to supplement oral TMZ therapy.

Another barrier to successful TMZ encapsulation was lack of uniformity across the current published literature with regard to improved formulations of NPs or mea-

surement techniques. While some publications report encapsulation efficiencies using a direct measurement of drug content in a pellet of NPs, others use indirect measurements that may result in an apparently higher, although less accurate encapsulation efficiency [71]. To improve data accuracy and minimize unnecessary and repetitive formulation changes, the nanotechnology community has recently proposed more standardized protocols for data reporting [79].

6. CONCLUSION

GBM is a devastating disease with a dismal prognosis and a paucity of effective chemotherapeutic agents. The increased mutation rate, infiltrative nature and high propensity for self-renewal of the CSC population are important reasons for failure of may single drug regimens against GBM. In an attempt to address these, this thesis outlines a strategy for using multi-functional polymer-micellar NPs to target the CSC population and deliver a therapy that overcomes GBM resistance to TMZ. Our polymer-micellar NPs utilized PLGA-NHS and PLGA-NH_2 functional groups to attach a CD133 aptamer and radiotracer while also maintaining a relatively uniform size of less than 100 nm with a slightly negative charge. Preliminary CD133 labeling of NPs demonstrated a trend in higher killing of CSCs in vitro compared with CD133 deficient NPs. Addition of PET radiotracer, ^{89}Zr, to our multi-functional CD133 targetable NPs introduced a potential theranostics application to allow real time in vivo fate mapping.

7. FUTURE WORK

There were limitations we encountered which would ideally be addressed in future work. The most important and time consuming limitation evolved around the difficulty we encountered with encapsulating TMZ. Options would be to either replace TMZ with a suitable anticancer drug or try a different encapsulation approach. For instance, a w/o/o phase separation in a non-aqueous medium could be studied. In this method, both hydrophilic and lipophilic drugs can be encapsulated while avoiding the possibility that aqueous solutions wash away hydrophilic drugs [80]. Instead of emulsifying the components in a larger volume of aqueous solution, the hydrophilic drug is mixed into an organic solvent in the presence of an organic nonsolvent, such as silicone oil, that will not dissolve either drug or the polymers [80]. As the organic solvent evaporates, this forces the polymers to undergo a phase separation and the polymer will adsorb onto the drug [80]. This method may increase the encapsulation of TMZ, but result in a size increase of our NPs.

If we were to eliminate TMZ from the particle system and use it as an oral agent we would develop new dual-drug NPs. Given the much higher potency of RG7388 we encountered in treating CSCs, TMZ encapsulation may need to increase significantly for a combination effect to be discerned. While studying drug effects on CSCs in the absence of NPs, we were able to utilize much higher concentrations of TMZ for comparison with RG7388. Higher amounts of RG7388 and low TMZ may result in predominately RG7388-induced toxicity. We could try to encapsulate RG7388 with another potent hydrophobic drug such as PTX that offers better encapsulation efficiency and greater cell killing. Preliminary data on the effectiveness of PTX in both CSC and GBM43 cell lines can be seen in the results as it seems to act more potently against GBM compared to even RG7388.

Additional studies to show the potential benefit of CD133-targeted NPs need to be conducted. Our current experiments show a slight increase in cytotoxicity with the addition of the CD133 aptamer to the NPs. However, because this increase had not been yet shown to be a significant change, the drugs may be releasing into the wells regardless of whether or not the NPs were bound to the CSCs. First, we need to conduct additional cytotoxicity trials. Next, to better assess the targeting ability of our CD133-labelled NPs we could try two different fluorescent techniques. The first option would be to assess uptake of CD133 targeted and non-CD133 targeted NPs into cells using fluorescence correlation spectroscopy (FCS) which assesses whether particles are taken into cells in vitro by the presence of a diffusion coefficient measured by the fluorescent marker. We conducted initial studies to determine the diffusion coefficient of NPs bound to the fluorescent aptamer by suspending them in water. However, during these studies, we were unable to accurately measure this value as the NPs seemed to produce a flickering effect, which introduced inconsistencies in the correlation analysis not to stabilize. Once the diffusion coefficient is determined, we can treat the aptamer-conjugated NPs in populations of CSCs. These plates would need to be either 24-well or 6-well plates to increase the amount of CSCs plated. These CSCs could be treated for perhaps 24 hours with the aptamer-conjugated NPs, fixed with paraformaldehyde and then analyzed using FCS. If the CSCs take up the NPs bound to the aptamer, we would see an increase in the diffusion coefficient. To compare targeted verses non-targeted NPs, we could label either the PLGA or the PS-*b*-PEO with a fluorescent dye such as Cy5 dye and analyze whether or not more CSCs take up the targeted or non-targeted CSCs. Second, fluorescent imaging microscopy could be performed permitting image acquisition of the Cy5 labelled NPs to assess cell uptake of targeted verses non-targeted NPs. Images could also be taken analyzing the uptake ability of CD133+ CSCs and the CD133- CSCs. To do this, we would need to sort the CSC population using fluorescence-activated cell sorting (FACS) by immunostaining the CD133+ population prior to sorting. We could also conduct this study in a co-culture with CD133+ CSCs and differentiated neuronal stem cells that

are determined to be CD133-. This would account for any non-specific targeting. Finally, differential killing of CD133 and non-CD133 labeled NPs may ultimately be further assessed in vivo since drug is released into the medium and subsequently enters the cells independent of the targeting of the NPs. In vivo may be the best route to fully demonstrate proof of targeting.

Future improvements of the labelling of ^{89}Zr also need to be made. In vivo studies can not be performed until we can label more ^{89}Zr to the NPs. One way to improve the labelling efficiency could be through the use of an alternate chelating agent. Previous work by Veronesi et al. used a derivative of DFO that was attached to a benzyl isothiocyanate (DFO-Bz-NCS) [68]. Furthermore, another study showed an increased in binding and stability using DFO* as part of the above derivative which adds an additional hydroxamic acid function to the chelate chain compared to DFO alone [81].

In summary, important progress was made in vitro towards the formation and initial testing of a multi-functional theranostics nanoparticle that can be used to target and treat the CSC specific cell population with GBM. This thesis comprised a significant portion of the in vitro arm of the project. The second arm of the project will be to test our compound in vivo in a preclinical model of GBM for both therapy efficacy and fate mapping.

REFERENCES

REFERENCES

[1] A. Vasilev, R. Sofi, L. Tong, A. G. Teschemacher, and S. Kasparov, "In search of a breakthrough therapy for glioblastoma," *Neuroglia*, vol. 1, no. 2, pp. 292–310, 2018.

[2] L. Chu, A. Wang, L. Ni, X. Yan, Y. Song, M. Zhao, K. Sun, H. Mu, S. Liu, Z. Wu, and C. Zhang, "Nose-to-brain delivery of temozolomide-loaded plga nanoparticles functionalized with anti-epha3 for glioblastoma targeting," *Drug Delivery*, vol. 25, no. 1, pp. 1634–1641, 2018.

[3] M. E. Davis, "Glioblastoma: Overview of disease and treatment," *Clin J Oncol Nurs*, vol. 20, no. 5 Suppl, pp. S2–8, 2016.

[4] S. K. Singh, C. Hawkins, I. D. Clarke, J. A. Squire, J. Bayani, T. Hide, R. M. Henkelman, M. D. Cusimano, and P. B. Dirks, "Identification of human brain tumour initiating cells," *Nature*, vol. 432, no. 7015, pp. 396–401, 2004.

[5] C. Fang, K. Wang, Z. R. Stephen, Q. Mu, F. M. Kievit, D. T. Chiu, O. W. Press, and M. Zhang, "Temozolomide nanoparticles for targeted glioblastoma therapy," *ACS Appl Mater Interfaces*, vol. 7, no. 12, pp. 6674–82, 2015.

[6] D. Nizamutdinov, E. M. Stock, J. A. Dandashi, E. A. Vasquez, Y. Mao, S. Dayawansa, J. Zhang, E. Wu, E. Fonkem, and J. H. Huang, "Prognostication of survival outcomes in patients diagnosed with glioblastoma," *World neurosurgery*, vol. 109, pp. e67–e74, 2018.

[7] A. Bohn, A. Braley, P. Rodriguez de la Vega, J. Carlos Zevallos, and N. Barengo, "The association between race and survival in glioblastoma patients in the us: A retrospective cohort study," *PLoS One*, vol. 13, no. 6, p. e0198581, 2018.

[8] E. Alphandéry, "Glioblastoma treatments: An account of recent industrial developments," *Frontiers in pharmacology*, vol. 9, pp. 879–879, 2018.

[9] A. Omuro and L. M. DeAngelis, "Glioblastoma and other malignant gliomas: a clinical review," *Jama*, vol. 310, no. 17, pp. 1842–50, 2013.

[10] K. Urbańska, J. Sokołowska, M. Szmidt, and P. Sysa, "Glioblastoma multiforme - an overview," *Contemporary oncology (Poznan, Poland)*, vol. 18, no. 5, pp. 307–312, 2014.

[11] C. J. Vecht, M. Kerkhof, and A. Duran-Pena, "Seizure prognosis in brain tumors: new insights and evidence-based management," *The oncologist*, vol. 19, no. 7, pp. 751–759, 2014. [Online]. Available: https://pubmed.ncbi.nlm.nih.gov/24899645 https://www.ncbi.nlm.nih.gov/pmc/articles/PMC4077452/

[12] M. S. Walid, "Prognostic factors for long-term survival after glioblastoma," *The Permanente journal*, vol. 12, no. 4, pp. 45–48, 2008.

[13] F. Pourgholi, M. hajivalili, J.-N. Farhad, H. S. Kafil, and M. Yousefi, "Nanoparticles: Novel vehicles in treatment of glioblastoma," *Biomedicine & Pharmacotherapy*, vol. 77, pp. 98–107, 2016.

[14] Q. SongTao, Y. Lei, G. Si, D. YanQing, H. HuiXia, Z. XueLin, W. LanXiao, and Y. Fei, "Idh mutations predict longer survival and response to temozolomide in secondary glioblastoma," *Cancer Sci*, vol. 103, no. 2, pp. 269–73, 2012.

[15] J. B. Hsu, T. H. Chang, G. A. Lee, T. Y. Lee, and C. Y. Chen, "Identification of potential biomarkers related to glioma survival by gene expression profile analysis," *BMC Med Genomics*, vol. 11, no. Suppl 7, p. 34, 2019.

[16] J. H. Lee, J. E. Lee, J. Y. Kahng, S. H. Kim, J. S. Park, S. J. Yoon, J. Y. Um, W. K. Kim, J. K. Lee, J. Park, E. H. Kim, J. H. Lee, J. H. Lee, W. S. Chung, Y. S. Ju, S. H. Park, J. H. Chang, S. G. Kang, and J. H. Lee, "Human glioblastoma arises from subventricular zone cells with low-level driver mutations," *Nature*, vol. 560, no. 7717, pp. 243–247, 2018.

[17] M. Da Ros, V. De Gregorio, A. L. Iorio, L. Giunti, M. Guidi, M. de Martino, L. Genitori, and I. Sardi, "Glioblastoma chemoresistance: The double play by microenvironment and blood-brain barrier," *International journal of molecular sciences*, vol. 19, no. 10, p. 2879, 2018.

[18] P. M. Glumac and A. M. LeBeau, "The role of cd133 in cancer: a concise review," *Clinical and translational medicine*, vol. 7, no. 1, pp. 18–18, 2018.

[19] G. Liu, X. Yuan, Z. Zeng, P. Tunici, H. Ng, I. R. Abdulkadir, L. Lu, D. Irvin, K. L. Black, and J. S. Yu, "Analysis of gene expression and chemoresistance of cd133+ cancer stem cells in glioblastoma," *Molecular cancer*, vol. 5, pp. 67–67, 2006. [Online]. Available: https://pubmed.ncbi.nlm.nih.gov/17140455 https://www.ncbi.nlm.nih.gov/pmc/articles/PMC1697823/

[20] C. Y. Lee and I. H. Ooi, "Preparation of temozolomide-loaded nanoparticles for glioblastoma multiforme targeting-ideal versus reality," *Pharmaceuticals (Basel, Switzerland)*, vol. 9, no. 3, p. 54, 2016.

[21] R. Stupp, W. P. Mason, M. J. van den Bent, M. Weller, B. Fisher, M. J. Taphoorn, K. Belanger, A. A. Brandes, C. Marosi, U. Bogdahn, J. Curschmann, R. C. Janzer, S. K. Ludwin, T. Gorlia, A. Allgeier, D. Lacombe, J. G. Cairncross, E. Eisenhauer, and R. O. Mirimanoff, "Radiotherapy plus concomitant and adjuvant temozolomide for glioblastoma," *N Engl J Med*, vol. 352, no. 10, pp. 987–96, 2005.

[22] D. Gramatzki, P. Roth, E. J. Rushing, J. Weller, N. Andratschke, S. Hofer, D. Korol, L. Regli, A. Pangalu, M. Pless, J. Oberle, R. Bernays, H. Moch, S. Rohrmann, and M. Weller, "Bevacizumab may improve quality of life, but not overall survival in glioblastoma: an epidemiological study," *Ann Oncol*, vol. 29, no. 6, pp. 1431–1436, 2018.

[23] S. De Vleeschouwer, *Glioblastoma*. Codon Publications, 2017.

[24] J. D. Lathia, S. C. Mack, E. E. Mulkearns-Hubert, C. L. L. Valentim, and J. N. Rich, "Cancer stem cells in glioblastoma," *Genes & development*, vol. 29, no. 12, pp. 1203–1217, 2015.

[25] A. Arora and K. Somasundaram, "Glioblastoma vs temozolomide: can the red queen race be won?" *Cancer Biol Ther*, vol. 20, no. 8, pp. 1083–1090, 2019.

[26] S. Emamgholizadeh Minaei, S. Khoei, S. Khoee, and M. R. Karimi, "Tri-block copolymer nanoparticles modified with folic acid for temozolomide delivery in glioblastoma," *Int J Biochem Cell Biol*, vol. 108, pp. 72–83, 2019.

[27] M. J. Ramalho, E. Sevin, F. Gosselet, J. Lima, M. A. N. Coelho, J. A. Loureiro, and M. C. Pereira, "Receptor-mediated plga nanoparticles for glioblastoma multiforme treatment," *Int J Pharm*, vol. 545, no. 1-2, pp. 84–92, 2018.

[28] P. P. Di Mauro, A. Cascante, P. Brugada Vilà, V. Gómez-Vallejo, J. Llop, and S. Borrós, "Peptide-functionalized and high drug loaded novel nanoparticles as dual-targeting drug delivery system for modulated and controlled release of paclitaxel to brain glioma," *International Journal of Pharmaceutics*, vol. 553, no. 1, pp. 169–185, 2018.

[29] J. Portnow, B. Badie, M. Chen, A. Liu, S. Blanchard, and T. W. Synold, "The neuropharmacokinetics of temozolomide in patients with resectable brain tumors: potential implications for the current approach to chemoradiation," *Clin Cancer Res*, vol. 15, no. 22, pp. 7092–8, 2009.

[30] E. Ozdemir-Kaynak, A. A. Qutub, and O. Yesil-Celiktas, "Advances in glioblastoma multiforme treatment: New models for nanoparticle therapy," *Frontiers in physiology*, vol. 9, pp. 170–170, 2018.

[31] J. B. Wang, D. F. Dong, M. D. Wang, and K. Gao, "Idh1 overexpression induced chemotherapy resistance and idh1 mutation enhanced chemotherapy sensitivity in glioma cells in vitro and in vivo," *Asian Pac J Cancer Prev*, vol. 15, no. 1, pp. 427–32, 2014.

[32] J. Huang, J. Yu, L. Tu, N. Huang, H. Li, and Y. Luo, "Isocitrate dehydrogenase mutations in glioma: From basic discovery to therapeutics development," *Frontiers in Oncology*, vol. 9, no. 506, 2019. [Online]. Available: https://www.frontiersin.org/article/10.3389/fonc.2019.00506

[33] H. Yan, D. W. Parsons, G. Jin, R. McLendon, B. A. Rasheed, W. Yuan, I. Kos, I. Batinic-Haberle, S. Jones, G. J. Riggins, H. Friedman, A. Friedman, D. Reardon, J. Herndon, K. W. Kinzler, V. E. Velculescu, B. Vogelstein, and D. D. Bigner, "Idh1 and idh2 mutations in gliomas," *The New England journal of medicine*, vol. 360, no. 8, pp. 765–773, 2009. [Online]. Available: https://pubmed.ncbi.nlm.nih.gov/19228619 https://www.ncbi.nlm.nih.gov/pmc/articles/PMC2820383/

[34] T. Glaser, I. Han, L. Wu, and X. Zeng, "Targeted nanotechnology in glioblastoma multiforme," *Front Pharmacol*, vol. 8, p. 166, 2017.

[35] A. Morokoff, W. Ng, A. Gogos, and A. H. Kaye, "Molecular subtypes, stem cells and heterogeneity: Implications for personalised therapy in glioma," *J Clin Neurosci*, vol. 22, no. 8, pp. 1219–26, 2015.

[36] M. E. Hegi, A. C. Diserens, T. Gorlia, M. F. Hamou, N. de Tribolet, M. Weller, J. M. Kros, J. A. Hainfellner, W. Mason, L. Mariani, J. E. Bromberg, P. Hau, R. O. Mirimanoff, J. G. Cairncross, R. C. Janzer, and R. Stupp, "Mgmt gene silencing and benefit from temozolomide in glioblastoma," *N Engl J Med*, vol. 352, no. 10, pp. 997–1003, 2005.

[37] H. Wang, S. Cai, B. J. Bailey, M. Reza Saadatzadeh, J. Ding, E. Tonsing-Carter, T. M. Georgiadis, T. Zachary Gunter, E. C. Long, R. E. Minto, K. R. Gordon, S. E. Sen, W. Cai, J. A. Eitel, D. L. Waning, L. R. Bringman, C. D. Wells, M. E. Murray, J. N. Sarkaria, L. M. Gelbert, D. R. Jones, A. A. Cohen-Gadol, L. D. Mayo, H. E. Shannon, and K. E. Pollok, "Combination therapy in a xenograft model of glioblastoma: enhancement of the antitumor activity of temozolomide by an mdm2 antagonist," *J Neurosurg*, vol. 126, no. 2, pp. 446–459, 2017.

[38] L. T. Vassilev, "Mdm2 inhibitors for cancer therapy," *Trends Mol Med*, vol. 13, no. 1, pp. 23–31, 2007.

[39] Y. Zhao, A. Aguilar, D. Bernard, and S. Wang, "Small-molecule inhibitors of the mdm2-p53 protein-protein interaction (mdm2 inhibitors) in clinical trials for cancer treatment," *J Med Chem*, vol. 58, no. 3, pp. 1038–52, 2015.

[40] M. Zanjirband, R. J. Edmondson, and J. Lunec, "Pre-clinical efficacy and synergistic potential of the mdm2-p53 antagonists, nutlin-3 and rg7388, as single agents and in combined treatment with cisplatin in ovarian cancer," *Oncotarget*, vol. 7, no. 26, pp. 40 115–40 134, 2016.

[41] A. B. Williams and B. Schumacher, "p53 in the dna-damage-repair process," *Cold Spring Harbor perspectives in medicine*, vol. 6, no. 5, p. a026070, 2016. [Online]. Available: https://pubmed.ncbi.nlm.nih.gov/27048304 https://www.ncbi.nlm.nih.gov/pmc/articles/PMC4852800/

[42] D. J. Jerry, L. Tao, and H. Yan, "Regulation of cancer stem cells by p53," *Breast cancer research : BCR*, vol. 10, no. 4, pp. 304–304, 2008. [Online]. Available: https://pubmed.ncbi.nlm.nih.gov/18828866 https://www.ncbi.nlm.nih.gov/pmc/articles/PMC2575544/

[43] N. Dadi, M. Stanley, S. Shahda, B. H. O'Neil, and A. Sehdev, "Impact of nab-paclitaxel-based second-line chemotherapy in metastatic pancreatic cancer," *Anticancer Res*, vol. 37, no. 10, pp. 5533–5539, 2017.

[44] M. T. Branham, S. B. Nadin, L. M. Vargas-Roig, and D. R. Ciocca, "Dna damage induced by paclitaxel and dna repair capability of peripheral blood lymphocytes as evaluated by the alkaline comet assay," *Mutat Res*, vol. 560, no. 1, pp. 11–7, 2004.

[45] S. B. Horwitz, "Taxol (paclitaxel): mechanisms of action," *Ann Oncol*, vol. 5 Suppl 6, pp. S3–6, 1994.

[46] E. Y. Chi, B. Viriyapak, H. S. Kwack, Y. K. Lee, S. I. Kim, K. H. Lee, and T. C. Park, "Regulation of paclitaxel-induced programmed cell death by autophagic induction: A model for cervical cancer," *Obstet Gynecol Sci*, vol. 56, no. 2, pp. 84–92, 2013.

[47] A. Rice, M. L. Michaelis, G. Georg, Y. Liu, B. Turunen, and K. L. Audus, "Overcoming the blood-brain barrier to taxane delivery for neurodegenerative diseases and brain tumors," *J Mol Neurosci*, vol. 20, no. 3, pp. 339–43, 2003.

[48] D. Bobo, K. J. Robinson, J. Islam, K. J. Thurecht, and S. R. Corrie, "Nanoparticle-based medicines: A review of fda-approved materials and clinical trials to date," *Pharm Res*, vol. 33, no. 10, pp. 2373–87, 2016.

[49] V. J. Mohanraj and Y. Chen, "Nanoparticles - a review," *Tropical Journal of Pharmaceutical Research*, vol. 5, no. 1, pp. 561–573, 2007.

[50] S. Bhatia, *Nanoparticles Types, Classification, Characterization, Fabrication Methods and Drug Delivery Applications*. Springer, Cham, 2016, pp. 33–93.

[51] M. C. Veronesi, M. Alhamami, S. B. Miedema, Y. Yun, M. Ruiz-Cardozo, and V. M. W., "Imaging of intranasal drug delivery to the brain," *Am J Nucl Med Mol Imaging*, vol. 10, no. 1, pp. 1–31, 2020.

[52] A. R. Khan, M. Liu, M. W. Khan, and G. Zhai, "Progress in brain targeting drug delivery system by nasal route," *J Control Release*, vol. 268, pp. 364–389, 2017.

[53] V. P. Chavda, *Chapter 4 - Nanobased Nano Drug Delivery: A Comprehensive Review*. Elsevier, 2019, pp. 69–92. [Online]. Available: http://www.sciencedirect.com/science/article/pii/B9780128140291000041

[54] E. R. de Oliveira Junior, T. L. Nascimento, M. A. Salomao, A. C. G. da Silva, M. C. Valadares, and E. M. Lima, "Increased nose-to-brain delivery of melatonin mediated by polycaprolactone nanoparticles for the treatment of glioblastoma," *Pharm Res*, vol. 36, no. 9, p. 131, 2019.

[55] J. Zhu and R. C. Hayward, "Spontaneous generation of amphiphilic block copolymer micelles with multiple morphologies through interfacial instabilities," *Journal of the American Chemical Society*, vol. 130, no. 23, pp. 7496–7502, 2008.

[56] B. Taghipour, M. Yakhchali, I. Haririan, A. M. Tamaddon, and S. M. Samani, "The effects of technical and compositional variables on the size and release profile of bovine serum albumin from plga based particulate systems," *Research in pharmaceutical sciences*, vol. 9, no. 6, pp. 407–420, 2014. [Online]. Available: https://pubmed.ncbi.nlm.nih.gov/26339256 https://www.ncbi.nlm.nih.gov/pmc/articles/PMC4326979/

[57] Y. Wang, P. Li, T. Truong-Dinh Tran, J. Zhang, and L. Kong, "Manufacturing techniques and surface engineering of polymer based nanoparticles for targeted drug delivery to cancer," *Nanomaterials (Basel, Switzerland)*, vol. 6, no. 2, p. 26, 2016.

[58] G. M. Nabar, K. D. Mahajan, M. A. Calhoun, A. D. Duong, M. S. Souva, J. Xu, C. Czeisler, V. K. Puduvalli, J. J. Otero, B. E. Wyslouzil, and J. O. Winter, "Micelle-templated, poly(lactic-co-glycolic acid) nanoparticles for hydrophobic drug delivery," *Int J Nanomedicine*, vol. 13, pp. 351–366, 2018.

[59] G. A. Husseini and W. G. Pitt, "Micelles and nanoparticles for ultrasonic drug and gene delivery," *Advanced drug delivery reviews*, vol. 60, no. 10, pp. 1137–1152, 2008. [Online]. Available: https://pubmed.ncbi.nlm.nih.gov/18486269 https://www.ncbi.nlm.nih.gov/pmc/articles/PMC2490710/

[60] S. Lakkadwala, B. Dos Santos Rodrigues, C. Sun, and J. Singh, "Dual functionalized liposomes for efficient co-delivery of anti-cancer chemotherapeutics for the treatment of glioblastoma," *J Control Release*, vol. 307, pp. 247–260, 2019.

[61] X. Gao, T. Yu, G. Xu, G. Guo, X. Liu, X. Hu, X. Wang, Y. Liu, Q. Mao, C. You, and L. Zhou, "Enhancing the anti-glioma therapy of doxorubicin by honokiol with biodegradable self-assembling micelles through multiple evaluations," *Sci Rep*, vol. 7, p. 43501, 2017.

[62] H. S. Choi, W. Liu, P. Misra, E. Tanaka, J. P. Zimmer, B. Itty Ipe, M. G. Bawendi, and J. V. Frangioni, "Renal clearance of quantum dots," *Nature biotechnology*, vol. 25, no. 10, pp. 1165–1170, 2007. [Online]. Available: https://pubmed.ncbi.nlm.nih.gov/17891134 https://www.ncbi.nlm.nih.gov/pmc/articles/PMC2702539/

[63] S. Bien-Moller, E. Balz, S. Herzog, L. Plantera, S. Vogelgesang, K. Weitmann, C. Seifert, M. A. Fink, S. Marx, A. Bialke, C. Venugopal, S. K. Singh, W. Hoffmann, B. H. Rauch, and H. W. S. Schroeder, "Association of glioblastoma multiforme stem cell characteristics, differentiation, and microglia marker genes with patient survival," *Stem Cells Int*, vol. 2018, p. 9628289, 2018.

[64] K. Gui, X. Zhang, F. Chen, Z. Ge, S. Zhang, X. Qi, J. Sun, and Z. Yu, "Lipid-polymer nanoparticles with cd133 aptamers for targeted delivery of all-trans retinoic acid to osteosarcoma initiating cells," *Biomed Pharmacother*, vol. 111, pp. 751–764, 2019.

[65] S. Shigdar, L. Qiao, S.-F. Zhou, D. Xiang, T. Wang, Y. Li, L. Y. Lim, L. Kong, L. Li, and W. Duan, "Rna aptamers targeting cancer stem cell marker cd133," *Cancer Letters*, vol. 330, no. 1, pp. 84–95, 2013.

[66] M. K. Yu, J. Park, and S. Jon, "Targeting strategies for multifunctional nanoparticles in cancer imaging and therapy," *Theranostics*, vol. 2, no. 1, pp. 3–44, 2012.

[67] F. C. J. van de Watering, M. Rijpkema, L. Perk, U. Brinkmann, W. J. G. Oyen, and O. C. Boerman, "Zirconium-89 labeled antibodies: a new tool for molecular imaging in cancer patients," *BioMed research international*, vol. 2014, pp. 203 601–203 601, 2014. [Online]. Available: https://pubmed.ncbi.nlm.nih.gov/24991539 https://www.ncbi.nlm.nih.gov/pmc/articles/PMC4058511/

[68] M. Veronesi, M. Zamora, M. Bhuiyan, B. Obrien-Penney, C. Chen, and M. Vannier, "Use of a clinical pet/ct scanner for whole body biodistribution of intranasal nanoparticles," 2017, arXiv:1704.00691.

[69] T. C. Chou, "Theoretical basis, experimental design, and computerized simulation of synergism and antagonism in drug combination studies," *Pharmacol Rev*, vol. 58, no. 3, pp. 621–81, 2006. [Online]. Available: http://pharmrev.aspetjournals.org/content/pharmrev/58/3/621.full.pdf

[70] ——, "Drug combination studies and their synergy quantification using the chou-talalay method," *Cancer Res*, vol. 70, no. 2, pp. 440–6, 2010.

[71] Y. Xu, M. Shen, Y. Li, Y. Sun, Y. Teng, Y. Wang, and Y. Duan, "The synergic antitumor effects of paclitaxel and temozolomide co-loaded in mpeg-plga nanoparticles on glioblastoma cells," *Oncotarget*, vol. 7, no. 15, pp. 20 890–20 901, 2016.

[72] J. Xie, S. Lee, and X. Chen, "Nanoparticle-based theranostic agents," *Adv Drug Deliv Rev*, vol. 62, no. 11, pp. 1064–79, 2010.

[73] R. L. McCall and R. W. Sirianni, "Plga nanoparticles formed by single- or double-emulsion with vitamin e-tpgs," *Journal of visualized experiments : JoVE*, no. 82, pp. 51 015–51 015, 2013. [Online]. Available: https://pubmed.ncbi.nlm.nih.gov/24429733 https://www.ncbi.nlm.nih.gov/pmc/articles/PMC4106449/

[74] X. Yu, L. Sun, L. Tan, M. Wang, X. Ren, J. Pi, M. Jiang, and N. Li, "Preparation and characterization of plga-peg-plga nanoparticles containing salidroside and tamoxifen for breast cancer therapy," *AAPS PharmSciTech*, vol. 21, no. 3, p. 85, 2020.

[75] N. Y. Martinez, P. F. Andrade, N. Duran, and S. Cavalitto, "Development of double emulsion nanoparticles for the encapsulation of bovine serum albumin," *Colloids Surf B Biointerfaces*, vol. 158, pp. 190–196, 2017.

[76] S. Khaledi, S. Jafari, S. Hamidi, O. Molavi, and S. Davaran, "Preparation and characterization of plga-peg-plga polymeric nanoparticles for co-delivery of 5-fluorouracil and chrysin," *J Biomater Sci Polym Ed*, pp. 1–20, 2020.

[77] M. Danaei, M. Dehghankhold, S. Ataei, F. Hasanzadeh Davarani, R. Javanmard, A. Dokhani, S. Khorasani, and M. R. Mozafari, "Impact of particle size and polydispersity index on the clinical applications of lipidic nanocarrier systems," *Pharmaceutics*, vol. 10, no. 2, 2018.

[78] Y. Zhao, Y. Wang, F. Ran, Y. Cui, C. Liu, Q. Zhao, Y. Gao, D. Wang, and S. Wang, "A comparison between sphere and rod nanoparticles regarding their in vivo biological behavior and pharmacokinetics," *Scientific Reports*, vol. 7, no. 1, p. 4131, 2017. [Online]. Available: https://doi.org/10.1038/s41598-017-03834-2

[79] M. Faria, M. Björnmalm, K. J. Thurecht, S. J. Kent, R. G. Parton, M. Kavallaris, A. P. R. Johnston, J. J. Gooding, S. R. Corrie, B. J. Boyd, P. Thordarson, A. K. Whittaker, M. M. Stevens, C. A. Prestidge, C. J. H. Porter, W. J. Parak, T. P. Davis, E. J. Crampin, and F. Caruso, "Minimum information reporting in bio-nano experimental literature," *Nature nanotechnology*, vol. 13, no. 9, pp. 777–785, 2018. [Online]. Available: https://pubmed.ncbi.nlm.nih.gov/30190620 https://www.ncbi.nlm.nih.gov/pmc/articles/PMC6150419/

[80] Y. Pathak and D. Thassu, *Drug Delivery Nanoparticles Formulation and Characterization*. Informa Healthcare, 2009.

[81] E. Berg, H. Gill, J. Marik, A. Ogasawara, S. Williams, G. van Dongen, D. Vugts, S. R. Cherry, and A. F. Tarantal, "Total-body pet and highly stable chelators together enable meaningful (89)zr-antibody pet studies up to 30 days after injection," *J Nucl Med*, vol. 61, no. 3, pp. 453–460, 2020.

APPENDICES

A. INDD REVIEW ARTICLE

Am J Nucl Med Mol Imaging 2020;10(1):1-31
www.ajnmmi.us /ISSN:2160-8407/ajnmmi0108227

Review Article

Imaging of intranasal drug delivery to the brain

Michael C Veronesi[1], Mosa Alhamami[1], Shelby B Miedema[1,2], Yeonhee Yun[1], Miguel Ruiz-Cardozo[3], Michael W Vannier[4]

[1]Department of Radiology & Imaging Sciences, Indiana University School of Medicine, USA; [2]Department of Biomedical Engineering, Indiana University-Purdue University Indianapolis, USA; [3]Clinical Research Institute, Universidad Nacional de Colombia School of Medicine, USA; [4]Department of Radiology, University of Chicago School of Medicine, USA

Received January 21, 2020; Accepted February 7, 2020; Epub February 25, 2020; Published February 28, 2020

Abstract: Intranasal (IN) delivery is a rapidly developing area for therapies with great potential for the treatment of central nervous system (CNS) diseases. Moreover, in vivo imaging is becoming an important part of therapy assessment, both clinically in humans and translationally in animals. IN drug delivery is an alIn fact, imaging hasternative to systemic administration that uses the direct anatomic pathway between the olfactory/trigeminal neuroepithelium of the nasal mucosa and the brain. Several drugs have already been approved for IN application, while others are undergoing development and testing. To better understand which imaging modalities are being used to assess IN delivery of therapeutics, we performed a literature search with the key words "Intranasal delivery" and "Imaging" and summarized these findings in the current review. While this review does not attempt to be fully comprehensive, we intend for the examples provided to allow a well-rounded picture of the imaging tools available to assess IN delivery, with an emphasis on the nose-to-brain delivery route. Examples of in vivo imaging, for both humans and animals, include magnetic resonance imaging (MRI), positron emission tomography (PET), single-photon emission computed tomography (SPECT), gamma scintigraphy and computed tomography (CT). Additionally, some in vivo optical imaging modalities, including bioluminescence and fluorescence, have been used more in experimental testing in animals. In this review, we introduce each imaging modality, how it is being utilized and outline its strengths and weaknesses, specifically in the context of IN delivery of therapeutics to the brain.

Keywords: Intranasal drug delivery, theranostics, multimodality imaging, blood-brain barrier

Introduction

The blood-brain barrier (BBB) is highly successful at protecting the brain from entry of potentially detrimental substances. Unfortunately, greater than 99% of potential therapies are also greatly restricted from entering the brain [1, 2]. Therefore, there is an urgent need to develop alternative delivery strategies for getting therapies around the BBB non-invasively. Intranasal (IN) delivery is a promising alternative to systemic administration that uses the direct anatomic pathway between the olfactory/trigeminal neuroepithelium of the nasal mucosa and the brain. Since only small amounts of a drug are delivered to the brain using this route, the mechanism of delivery needs to be better understood and new methods need to be developed to overcome the obstacles facing nose-to-brain delivery of promising therapeutics. The key to overcoming these challenges and furthering the field of IN delivery is to develop informative, non-invasive methodologies to better understand the nose-to-brain delivery pathway. One important tool at our disposal is through the use of in vivo imaging. In fact, imaging has great potential to facilitate the translation of promising IN therapies from animals to humans and improved imaging techniques continue to emerge. Prior to discussing the imaging aspect, we will introduce the concept of IN delivery, explore the latest information regarding the most likely path from nose-to-brain and discuss various types of therapies that would benefit from IN imaging assessment. In particular, we lay the groundwork for the importance of developing theranostic agents for both therapy and diagnosis in one platform.

The nasal cavity is well-suited for therapy delivery since the nasal mucosa has a high relative permeability, thin endothelial membrane and reasonable surface area for absorption of not only small molecules but also macromolecules such as proteins and peptides, nucleotides, viruses and even stem cells [3-5]. In particular, nose-to-brain therapy delivery has garnered high interest given the high failure rate of drugs that are unable to bypass the BBB [6]. Examples of difficult-to-treat central nervous system (CNS) diseases include brain malignancies, neurodegenerative diseases, stroke, seizures and psychiatric diseases, among others [7]. Understanding the mechanism of delivery and fate of drugs that can bypass the BBB is imperative to treating these debilitating and costly diseases [8].

IN delivery offers several advantages over other routes of administration: It is relatively non-invasive, it avoids first-pass metabolism and its side effects can be minimized since other healthy organs are not exposed to the therapeutic compound [4]. Because of its non-invasive nature, there is a reduced risk of infection or disease transmission. Additionally, nasal spray formulations are easy to administer and can be performed at home by the patient. As with any route of delivery, however, there are challenges that must be overcome when using the nasal cavity for therapy delivery. Similar to the BBB, the nasal mucosal barrier poses IN delivery challenges, such as a physical boundaries provided by tight junctions, cellular membranes and enzymes in the mucosal milieu. In addition, certain environmental substances, including pathogens and allergens, can irritate the nasal mucosa and full delivery of a drug may be impaired when a patient has an active upper respiratory infection. Mucociliary clearance can also hinder the delivery of intranasally administered therapeutics. Thus, only a small percentage of the administered drug may arrive at the target site following IN delivery; so, a compound requiring relatively high concentrations for therapeutic efficacy may not be an ideal candidate for this route.

Aside from its purported role as a promising route of drug delivery, the nasal cavity normally serves important roles in respiration and smell while also providing a protective barrier against environmental insults [9]. The nasal anatomy in animals can differ widely relative to humans. For instance, the ratio of surface area to luminal volume in the nasal cavity of a rat is very different from that in humans (i.e., rat is 3350 mm^2/cm^3 and human is 820 mm^2/cm^3) [10]. The relatively larger dedication of olfactory mucosa to smell in rodents allows a particularly strong model for IN delivery, but a lower contribution of olfactory mucosa to smell in humans poses a challenge when interpreting drug efficacy results from rodent data. The anterior vestibule, the respiratory region and the olfactory region serve as three different anatomically distinct areas in the nasal cavity and only the respiratory and olfactory regions are thought to contribute to drug delivery (**Figures 1** and **2**) [9, 10].

The respiratory epithelium is the largest of the three areas, is located more anteriorly within the nasal cavity, and produces the majority of the mucus, which is an additional barrier that intranasally delivered drugs must overcome for CNS delivery [11]. Drugs that overcome mucociliary clearance and make their way across the respiratory epithelium, such as naloxone and zolmitriptan, may be absorbed into the small blood vessels within the lamina propria, where they would avoid first-pass metabolism encountered with orally delivered agents, but would then still need to cross through the BBB from the systemic circulation [12]. The lamina propria of the respiratory epithelium also contains a high surface area of branches of the trigeminal neuron which, along with a multitude of small blood vessels, that provides a significant perineuronal and perivascular pathway for therapeutics to enter the brain [4, 13-15]. For instance, Lochhead et al. used ex vivo fluorescence imaging (FLI) to show that bulk flow within the perivascular space of cerebral blood vessels contributes to the rapid central distribution of small-molecule, fluorescently labeled dextran tracers after IN administration in anesthetized adult rats [15]. Labeled macromolecules, such as interferon gamma [16], insulin-like growth factor [14], and most recently insulin [17], also demonstrated rapid uptake into the brain and cerebral spinal fluid (CSF) spaces along the trigeminal route following IN administration.

The olfactory epithelium is the most posteriorly located epithelium of the nasal cavity (**Figures**

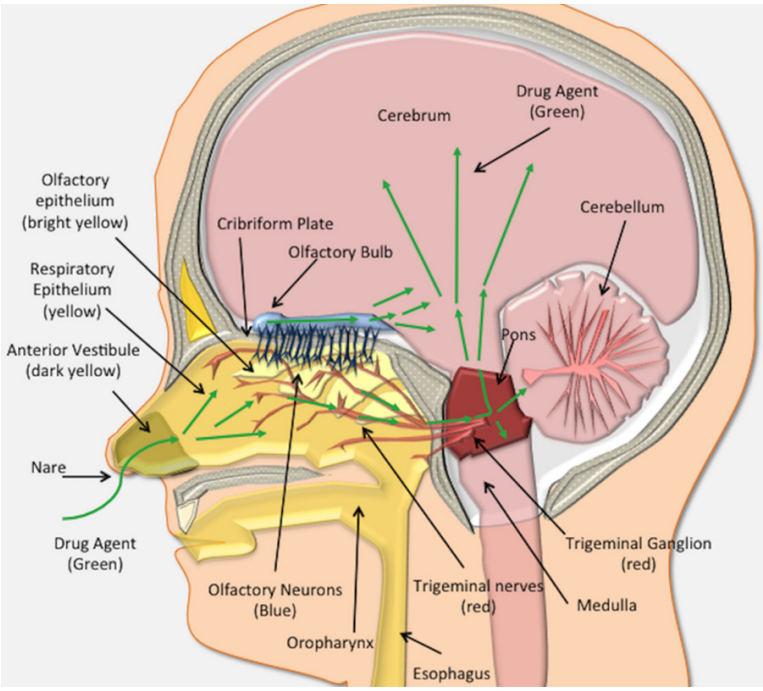

Figure 1. The human nose-to-brain anatomy. In humans, the nasal cavity contains three major regions based on epithelial type. The first most anterior vestibule (dark yellow), is comprised of squamous epithelial cells and does not play a significant role in drug absorption/uptake. Just posterior to the anterior vestibule is the respiratory epithelium (yellow). Drugs (green arrows) absorbed across the respiratory epithelium can be deposited into the lamina propria where they gain access to an extensive pathway to the brain along the branches of the trigeminal nerve. Drugs can travel intraneuronally or in a perineural and perivascular distribution to enter the brain via the trigeminal ganglion (red) and brainstem (red). Finally, posteriorly and dorsally lies the olfactory epithelium (bright yellow), which houses the olfactory neurons (blue), and is situated at the posterior and dorsal aspect of the nasal cavity. These neurons send cilia into the nasal cavity lumen. Drugs can be absorbed into the olfactory receptors or traverse the olfactory epithelium to gain access to the olfactory bulb by transcellular or perineuronal/perivascular routes within the lamina propria. From the olfactory bulb (blue), drugs (purple arrows) gain access to the brain (pink).

1 and **2**), and is structurally different from the respiratory epithelium since it contains bipolar primary receptor neurons necessary for our sense of smell [18, 19]. The olfactory epithelium overlies the cribriform plate and biopsy studies of humans indicate that the olfactory region may cover more of the nasal cavity than previously thought, extending to involve the middle turbinate (**Figures 1** and **2**) [9, 20]. Like the respiratory epithelium, the olfactory neuroepithelium sits atop a highly cellular lamina propria that contains the axon fascicles as well as Bowman's glands, blood vessels, and connective tissue (**Figure 3**) [11]. However, the olfactory epithelium also contains the olfactory receptor neurons and olfactory ensheathing cells, which can serve as a means of direct intra-neuronal transport into the olfactory bulb of the brain. This direct transport is made possible if the cilia aid in cellular uptake of the therapy or provide an additional highway to the brain CSF spaces. The cilia also provide a similar highway along extensive perivascular and perineuronal spaces found with the trigeminal system within the lamina propria. The classically cited example of direct neuronal transport is wheat-germ agglutinin conjugated to horseradish peroxidase, which was visible in neuronal axons and the olfactory bulb following IN delivery in mouse, rat and squirrel monkey [21]. However, intraneuronal transport is slow with studies indicating brain entry via the olfactory nerve taking 1.5-6 hours and even longer via the trigeminal nerve, taking from 17-56 hours [3]. Since several studies have confirmed rapid nose-to-brain delivery within minutes, the intra-neuronal pathway is probably not the primary route.

Intranasal therapies

The various IN therapies that have been attempted and published are extensive. The current review provides only examples to give a flavor of intranasally delivered therapies. For a more detailed description specific to therapies, the reader is referred to the following reviews by Fortuna et al. [22], Erdő et al. [23] and Corrigan et al. [24]. Although more often for systemic or local treatment, examples of therapies currently used clinically through the IN route include nasal sprays for allergic rhinitis (Azelastin Hydrochloride: Astelin, Meda Pharmaceuticals, Inc.), the common cold (Oxymetazoline: Afrin, Merck and Co, Inc), vaccines

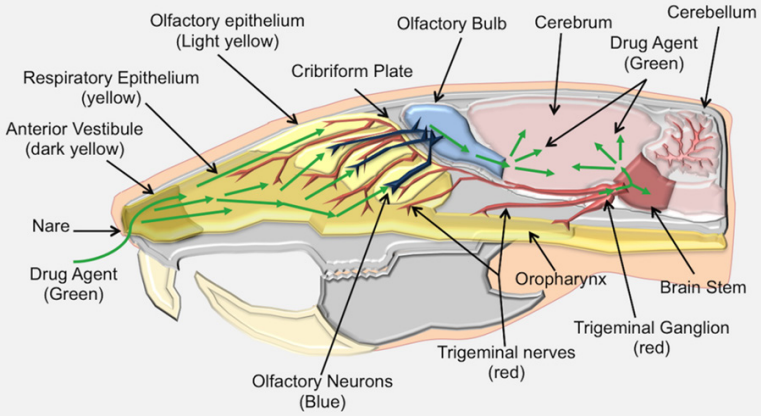

Figure 2. Rat nose-to-brain anatomy. The nose-to-brain anatomy of the rat is similar to the human with a few differences. Compared to the human, the rat nasal cavity has a relatively greater surface area in the olfactory system, making it an ideal animal model for studying IN delivery. The rat nasal cavity consists of the anterior vestibule (dark yellow), respiratory epithelium (yellow), transitional epithelium and olfactory epithelium. Drugs (green arrows) gain access to the brain along the olfactory and trigeminal pathways, similar to human IN delivery.

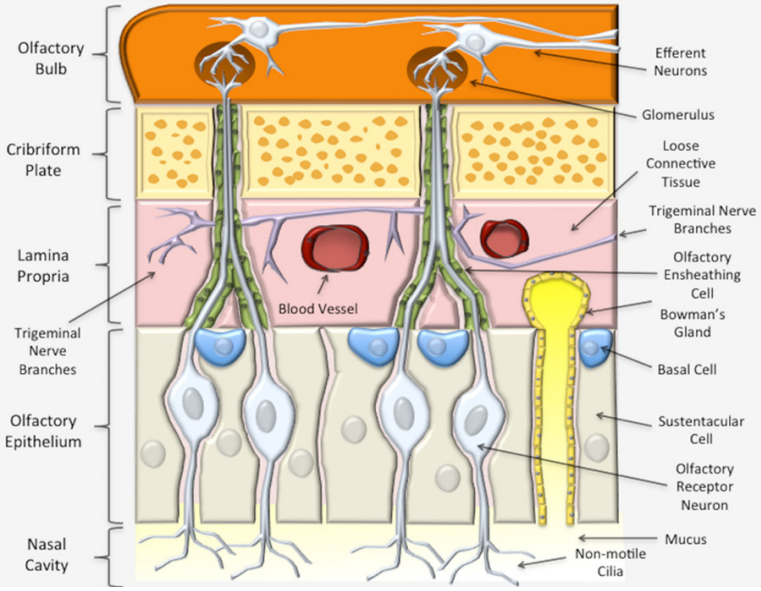

Figure 3. Olfactory nasal mucosa. The olfactory epithelium is mostly comprised of olfactory receptor cells and sustentacular support cells. Deep to the olfactory epithelium is the lamina propria (pink), which contains blood vessels, lymphatics and abundant branches of the trigeminal sensory neurons. Compounds deposited into the lamina propria can travel in a perineural, perivascular or perilymphatic manner to access the brain (orange). The axons of the olfactory cells traverse the lamina propria and form nerve fascicles, called the fila olfactoria. Olfactory ensheathing cells (green) pass through the cribriform plate (yellow) along with the olfactory nerve axons. The olfactory neuron axons synapse in olfactory bulb with second order neurons that then travel to other parts of the brain.

(FluMist Quadrivalent, MedImmune, LLC), and others. Agents currently undergoing clinical trials, many of which take advantage of the nose-to-brain route, include IN insulin for memory (NCT02758691), post-traumatic stress disorder (PTSD) (NCT04044534), mood disorders [25], and Alzheimer's disease [26, 27]; IN glutathione for Parkinson's disease (NCT01398748) [28]; IN oxytocin for autistic spectrum disorder [29, 30], Prader-Willi syndrome [31], attention-deficit/hyperactivity disorder (ADHD) [32] dementia [33], and schizophrenia; IN dexmedetomidine for sedation of patients with autism spectrum disorder (NCT03597477); IN fentanyl for cancer pain management (NCT00994760); nerve growth factors for stroke (NCT03686163) and IN neuropeptide Y for PTSD (NCT01533519) [34]. Clinical trials of IN delivery are often focused in pediatrics because of the relatively greater ease of IN administration compared to intravenous (IV) delivery and better patient comfort for pediatric patients. These include dexmedetomidine for IN anesthesia (NCT03597477), IN ketorolac for pain (NCT02297906), and midazolam for anti-anxiety (NCT03635398). In addition to clinically approved drugs, the number of compounds undergoing experimental evaluation using the IN route in animal models is extensive and beyond the scope of this review.

Therapeutic compounds delivered intranasally vary widely and each type of therapy has important challenges to consider. In this review, we delineate small molecules which are less than 900 Daltons from macromolecular compounds, such as nucleic acids and peptides/proteins. We also discuss two additional cate-

gories: Nanosystems, including nanoemulsions (NEs) and nanoparticles (NPs), as well as therapeutic stem cells [35]. While all of these categories could be adapted to serve as theranostic agents, nanosystems and cellular therapies are particularly suited for this emerging concept, which combines therapy with diagnostic information. Typically, nanosystems and cells have the greatest potential to adapt to become theranostic agents. It should be noted, however, that not every theranostic agent is in the form of a nanosystem.

Small molecules

Small-molecule drugs are among the most common intranasally delivered therapies administered to humans because of their small size (less than 900 Da), which allows for rapid diffusion across cell membranes. Examples of clinically approved small molecules include anesthetic agents [36] as well as drugs that treat migraines [37], treatment-resistant depression [38], seizures [39], pain modulation [40, 41] and antidotes for drug overdose (i.e., naloxone) [42]. More experimental examples at the preclinical level include morphine and oxycodone for the reduction of intentional drug abuse [43, 44] and doxylamine in subjects with sleep impairment [45]. Since many small molecules are already approved for human use via topical, enteric or IV routes of administration, the regulatory burden for approval of IN delivery of small molecules is small [22]. However, most small molecules that can be used intranasally can also be delivered orally. In addition, many of the above-listed small molecules may utilize the nose-to-brain route to some extent, but the majority is likely to become systemically available following absorption across the nasal membrane barrier [46].

Nose-to-brain delivery of drugs occurs through a variety of different pathways; therefore, to optimize a small molecule for maximum delivery, it is important to tailor the molecule to travel through any of the possible pathways rather than focus on any one [47]. Designing the best small molecule would involve balancing a variety of factors including hydrophilicity, polarity, charge, size and molecular interactions. Mucin, which is a glycoprotein constituent of mucus, has both hydrophobic and hydrophilic components. While hydrophilic drugs are very soluble in mucus, leading to high clearance, extremely hydrophobic agents may interact with the mucus and fail to reach the nasal cavity [3, 22]. To achieve the highest probability of transport, a drug needs to exhibit moderate hydrophilic properties to minimize hydrophobic interactions with the mucus and maintain the ability to be dissolved in aqueous medium, all while avoiding clearance. Molecules that are polar tend to have low bioavailability since they are prone to clearance or decomposition by nasal enzymes [22]. In terms of charge, mucin is negatively charged; so, to minimize electrostatic interactions that would cause drug entrapment within the mucous, the drug needs to be neutral or slightly negative at physiological pH [3]. While small molecules are generally not inhibited via size restraints, it is necessary to design these molecules in a way that limits potential molecular interactions that would trap them in the nasal mucosa for clearance and prevent absorption across the mucosa [48].

Macromolecular agents

IN delivery provides a viable route to the CNS for macromolecular agents if they can overcome the anatomic and functional impediments of the nasal mucosal barrier. Examples of macromolecular agents include most drugs that are larger than 900 Da by molecular weight, but more specifically include agents that are not likely to be absorbed following oral delivery such as peptides, proteins, and nucleic acids. These agents are commonly called biologics, which are considered a collection of macromolecular compounds with a high potential for therapy. Most proteins [22] and even therapeutic plasmids [49] and viruses [50] would fall into this category. Therapeutic neuropeptides belong to a class of small peptides. They are promising for IN drug delivery for CNS applications because of their decreased molecular weight compared to larger proteins and macromolecular compounds. A good example in this group is oxytocin, which has been studied extensively as a psycho-modulator of several cognitive responses and social interactions [51, 52] and has been used in clinical trials to treat mental disorders [53-55].

Macromolecules are prone to the same issues as small molecules since these, too, must traverse the aforementioned barriers and abide

by optimization guidelines. Compared to small molecules, macromolecular agents are much more sensitive to size and, as the molecular weight increases, the absorption rate decreases [48]. Given the limitations encountered with delivering small molecules and macromolecules across the nose-to-brain barriers, several absorption-enhancing materials are being investigated and developed, including cell-penetrating peptides (i.e., penetratin [56, 57]), agents that open the tight junctions between cells (i.e., chloramphenicol acetyltransferase and matrix metalloproteinases [58]), and even agents that reversibly destroy the most superficial layer of the nasal mucosa (i.e., methimazole [59]). However, with the implementation of enhancers, there is a risk of a leaky BBB and a risk of CNS infection, potentially leading to brain edema [3]. In addition, macromolecules are subject to other challenges such as higher susceptibility to enzymatic degradation, from lower permeability and shape restraints [22]. Furthermore, it was found that linear molecules seem to have lower absorption than cyclic molecules [22]. The optimization of small and large molecules was outlined by Kumar et al. [48]. Some characteristics to look for include therapeutic effects at lower volumes, appropriate nasal absorptive characteristics, minimal nasal irritation, higher drug stability, and minimized odors or other comfort deterrents with the therapy [48].

Nanosystems

Despite the potential advantages of IN delivery to circumvent the BBB, most small-molecule and macromolecule therapies in solution must still overcome several obstacles in transit to the brain or CSF spaces. It is estimated that 98% of low-molecular-weight molecules and 100% of high-molecular-weight macromolecules fail in entering the CNS due to physiological and physiochemical challenges [48, 60]. The extremely low bioavailability of these molecules challenges their use intranasally. However, concentration levels can be further manipulated by nanotechnology-based systems, nanosystems. Specific examples that can be grouped more broadly into nanosystems would include nanogels, dendrimers, nanosuspensions, NEs, and NPs, to name a few [48, 61]. Drug-loaded nanosystems present various advantages that have potential to overcome the aforementioned challenges. These include improved endothelial permeability and extravasation, enhanced interstitial diffusion and decreased clearance or trapping by phagocytes. Additionally, nanosystems can be decorated with disease-specific ligands that target biomarkers of interest, thereby improving their biodistribution profile and minimizing toxicity to healthy tissues. Incorporating CNS drugs into nanosystems can also preserve the pharmacological action and physicochemical integrity of the drugs and reduce their dilution with body fluids. These advantages can significantly improve the safety profiles of CNS drugs and increase their maximum tolerated doses (MTDs). Overall, to justify an agent's delivery via a nanosystem, its incorporation must overcome the limitations associated with free drug. Furthermore, drugs that are quickly cleared need to have increased absorption and the nanosystem must protect the drug from enzymatic degradation in the nasal cavity. Strong drug candidates would include low water solubility, instability, slow onset of action, and those requiring high dosages that create systemic side effects [60]. Optimal nanosystems would remain less than 200 nm as the diameter of olfactory axons ranges from 100 nm to 700 nm and the mesh size of mucin ranges from 20 nm to 200 nm [3, 60]. To sum up, the benefit of using a nanosystem as a drug carrier and/or solubilizer is the ability to modify and fill in any weaknesses associated with the delivery of free drugs. There are a variety of different materials available to complete this.

Further optimization methods address the challenges discussed above. Each nanosystem has distinct advantages, but NPs and NEs will be described in brief specifically, outlining their role in IN delivery and imaging. For a more detailed information regarding nanosystems, the reader is referred to reviews from Kumar et al. [48], Patra et al. [62], and Chavda [61].

NPs are compact particles with diameters ranging from 1 to 1000 nm [48]. They can be fabricated by a variety of procedures including solvent evaporation, ionic gelation, or precipitation [61, 63]. NPs may be composed of biodegradable and non-biodegradable constituents and can be categorized as polymeric, polymeric micelles, liposomal, and inorganic, among others [64]. Polymeric NPs are often the

simplest type, utilizing single polymer chains. Alteration of polymer molecular weights allows fine tuning of drug release kinetics. Polymeric NPs can be fabricated with a variety of different methods including dispersion of polymers, polymerization of monomers, and ionic gelation [65]. Polymeric micelles are self-assembled polymeric amphiphiles that can deliver hydrophobic drugs, though there have been studies utilizing them to deliver hydrophilic imaging agents which were loaded into micelle's core through polymer-metal complex formation [66]. Liposomal NPs are also self-assembled via methods such as nanoprecipitation [67], thin-film hydration and extrusion [68], and electrospinning [69] and can encapsulate both hydrophobic and hydrophilic drugs and imaging agents. Finally, inorganic NPs offer advantages for both imaging and therapy as they contain materials such as iron oxide, gold and silica, among others. Gold NPs, in particular, are useful as they have also been studied as radiosensitizers for cancer cells [70]. These are non-biodegradable and are very small, less than 100 nm. Several NPs are FDA approved for human use and are extensively outlined by Bobo et al. including polymeric NPs (Copaxone® and Eligard®), polymeric micelles (Estrasorb™), polymer-protein conjugates (e.g., PegIntron®, Somavert), liposomal NPs (Marqibo®, Doxil®/Caelyx® and Onivyde®), and inorganic NPs (Nanotherm®, Ferrlecit®, and Feraheme™) [64]. One example of current research is polycaprolactone polymer NPs prepared by nanoprecipitation. They are being investigated for the nose-to-brain delivery of melatonin for the treatment of glioblastoma. Compared to free drug, melatonin NPs had significantly improved therapeutic efficacy, reducing the amount of drug required [63]. Bioavailability of NPs has been a debatable subject as IN delivery poses the same physical and chemical barriers like other drugs; the difference is that NPs offer more chances to finely tune the delivery system [48]. Furthermore, there are general challenges such as macrophage recognition of surface moieties. A variety of mucoadhesive polymers are incorporated to extend adhesion time in the nasal cavity, thereby preventing clearance. These include chitosan, alginates and cellulose [22]. Increased adhesion time as a mean to promote increased therapy remains controversial. On one side, increased adhesion prevents transport to the brain. On the other, increased adhesion prevents clearance and increases the chance of endocytosis [3]. Other challenges include premature release of drugs, toxicity and achieving desired dose requirements [61].

NEs are nano-sized globules that are biphasic, containing two immiscible liquids (water/oil) and a variety of surfactants and co-surfactants [71]. Some commercially available NEs, not specific to nose-to-brain delivery, include Diazemuls®, Lipuroetomidate® and Diprivan®, etc. Unlike NPs, there is no distinct boundary of each droplet; however, the globule is typically known to have sizes of 100-300 nm or less [60]. NEs are either oil-in-water (O/W) or water-in-oil (W/O) emulsions fabricated by high energy (ultrasonication/homogenization) or low energy (phase inversion by temperature/composition changes) techniques [60]. However, to our knowledge, only an O/W emulsion is used for IN administration of drugs. NEs interact directly with the aqueous environment via Brownian motion of the droplets [48]. NEs, like NPs, allow the transport of hydrophobic drugs into the brain. For example, saquinavir is an anti-HIV drug, but its water insolubility renders it a strong candidate for delivery via a NE. NEs showed an increase in permeation into the brain compared to free drug [60]. Another study by Colombo et al. analyzed the effects of incorporating chitosan into NEs [72]. Chitosan is heralded in NEs for its ability to act as a mucoadhesive to decrease nasal clearance [71]. A NE containing kaempferol was made with and without conjugation to chitosan for the treatment of glioma. It was found, in an ex vivo analysis, that NEs conjugated to chitosan significantly increased permeation across the mucosa because of the electrostatic interaction of positively charged chitosan and negatively charged mucosal layers, while also significantly increasing the amount of drug delivered to the brain [72]. Mucoadhesives appear to be quite critical in avoiding NE clearance and their use optimizes drug delivery [71]. Uniquely, NEs use a high concentration of surfactants that can be chosen from a list of generally regarded as safe (GRAS) agents including polyethylene glycol (PEG) 8 stearate, PEG 400, polysorbate 20 and propylene glycol, to name a few [61, 71]. Such surfactants can provide a fluidizing effect on the barrier endothelial cells, promoting drug permeability within the olfacto-

ry and trigeminal pathways [60]. Despite their advantages, those surfactants need to be monitored for toxicity with repeat dosages. Furthermore, both NPs and NEs are subjected to scale-up challenges. In a laboratory setting, these systems are made using specific material amounts in a specific order, which makes their translatability to industry a challenge.

Cellular therapies

IN delivery of stem cells to the brain overcomes the certain challenges associated with brain drug delivery and is highly amenable to theranostics. Multiple studies have confirmed the localization of various stem cells in the brain following IN delivery, including mesenchymal stem cells (MSCs), neural stem cells (NSCs) and pluripotent stem cells [73, 74]. MSCs were delivered to the brain via the IN route, successfully treating animal models of neurodegenerative diseases, including Parkinson's disease, Alzheimer's disease and Huntington's disease [75-77]. MSCs have also been delivered intranasally for the treatment of stroke [78, 79], including neonatal hypoxia-ischemia [80, 81]. In addition, MSCs delivered via nasal application imparted therapeutic efficacy when expressing tumor necrosis factor (TNF)-related, apoptosis-inducing ligand in a mouse model of human glioma. The increased overall survival was even higher when the mice had been irradiated [82]. The irradiated mice showed higher levels of CXCL12, a lymphatic chemokine, which is possibly related to the mechanism of migration of those cells [83]. Although radiotherapy is a highly effective tool for the treatment of brain cancer, it also causes detrimental effects in surrounding healthy tissues, leading to pernicious neurocognitive side effects. A novel strategy to mitigate the negative effects of radiation in brain tumor treatment involved IN administration of human MSCs, which promoted brain injury repair and improved neurological function following brain irradiation in mice [84]. Stem cells have become carriers of oncolytic agents or drugs due to their capability to target brain tumors when the stem cells and tumor cells express specific cell adhesion molecules. For instance, CXCR4-enhanced NSCs delivered an oncolytic virus to glioma and extended survival of animals when they received concomitant radiotherapy [85]. Moreover, neural stem/progenitor cells (NSPCs) displayed a rapid, targeted tumor tropism with significant accumulation at the intracranial glioma site within 6 hours after IN delivery. This peaked at 24 hours and remained at this level for up to five days. Currently, two clinical trials are assessing IN delivery of stem cells in the brain. One is recruiting to evaluate the use of autologous bone marrow-derived stem cells (BMSC) to improve cognitive function (NCT03724136). Another is also recruiting to study the use of autologous BMSC and its transfer to the vascular system and inferior 1/3 of the nasal passages in order to determine if such treatment will provide improvement in neurologic function for patients with a broad spectrum of neurologic conditions (NCT02795052). Overall, cellular therapies are an emerging therapy that may offer many benefits for IN delivery.

Theranostics

The development of a single platform for the simultaneous delivery of therapeutics and diagnostic imaging agents for pretreatment planning, real-time tracking/monitoring and/or posttreatment assessment provides the basis for the emerging field of theranostics [86]. Molecules such as metaiodobenzylguanidine (MIBG) containing iodine-131 (^{131}I) and iodine-123 (^{123}I), somatostatin peptide analogs labelled with lutetium-177 (^{177}Lu) and prostate-specific membrane antigen (PSMA) labelled with ^{123}I, ^{131}I, gallium-68 (^{68}Ga), ^{177}Lu and yttrium-90 (^{90}Y) have been used as theranostic materials in nuclear medicine [87, 88]. Also, radioactive ^{131}I is used to simultaneously image and treat thyroid diseases [89]. In general, direct imaging of small-molecule and macromolecular therapies following IN delivery in vivo is difficult to do since the addition of an imaging tracer runs the risk of interfering with drug binding site, thereby altering therapeutic efficacy. Imaging labels directly conjugated onto the therapeutic agent may also negatively alter biodistribution and pharmacodynamic/pharmacokinetic profiles. Regardless, direct labeling of drugs would benefit from in vivo imaging to better understand the ultimate fate of therapies after delivery, which includes the route of transit from nose-to-brain. When developing therapies that utilize nanosystems or cells, labeling agents for in vivo imaging becomes more feasible, albeit still technically

challenging. A recent NP-based drug delivery system was formulated for the treatment of glioblastoma by Sukumar et al.; it provides a comprehensive example of the multiple functions NPs can have. Briefly, gold-iron oxide NPs loaded with microRNAs for IN delivery were produced to provide a multi-functional theranostic capability for the treatment of glioblastoma. These NPs were coated with β-cyclodextrin-chitosan (CD-CS) hybrid polymer for the co-loading of the microRNAs. Finally, the NPs were decorated with PEG-T7 peptides to specifically target glioblastoma cells. In vivo analysis showed that these multi-functional NPs provided tumor sensitization, via the microRNAs, to the standard-of-care treatment, temozolomide, improving overall survival. Because of the gold-iron oxide component, the IN delivery of the NPs was monitored via T_2-weighted magnetic resonance imaging (MRI) [90].

Intranasal imaging

In humans, IN imaging studies have thus far been limited mostly to MRI, positron emission tomography (PET) and single-photon emission computed tomography (SPECT), with MRI being the most extensively utilized modality. Gamma scintigraphy, to our knowledge, has been used clinically in the context of IN imaging in one instance. Preclinical studies that utilize imaging offer a great deal of information about the fate of the delivered therapeutic and/or disease progression, which would enable the efficacy of novel IN therapies and their potential for clinical translation. So far, preclinical imaging studies have not only utilized MRI, PET and SPECT but also gamma scintigraphy as well as bioluminescence imaging (BLI) and fluorescence imaging (FLI). Ultrasound imaging, however, has not yet been used for IN imaging by virtue of the difficulties associated with transmitting and receiving acoustic waves across osseous structures using diagnostic ultrasound transducers in the clinical megahertz ranges. Nevertheless, ultrasound waves can be focused using specialized therapeutic focused transducers in order to enhance transmission and enable therapeutic benefits for IN drug delivery; this emerging approach, which is known as focused ultrasound-mediated drug delivery, will be briefly discussed later in this Review. A few CT studies have been used in humans and animals, mostly to study nasal anatomy and nasal flow dynamics. Combined PET and MR has perhaps the highest future potential for the assessment of the nose-to-brain route of drug delivery since they can combine both the high quantitation and sensitivity of molecular imaging with the high tissue contrast and spatial resolution of MRI. However, very few studies have been performed to date using this dual-modality approach which enables understanding of in vivo biological processes at a fundamental level. In subsequent paragraphs, we review each imaging modality and its contribution to understanding IN delivery from both a preclinical and clinical perspective.

Magnetic resonance imaging

MRI is a powerful, non-ionizing imaging technology that utilizes a strong magnet (typically 0.5-3 tesla for humans and up to 21.1 tesla for small animals) to produce three-dimensional detailed anatomical images [91]. MRI has revolutionized medicine because of its ability to generate high spatial resolution images and exquisite soft tissue contrast (**Table 1**). In humans, it is used for disease detection and therapy monitoring. MRI signals are produced through the process of resonance using radiofrequency (RF) coils, which include a transmitter and receiver. The RF transmitter coils generate a secondary magnetic field (B_1) that is perpendicular to the main magnetic field (B_0), whereas the RF receiver coils detect the resulting MR signal. The transmitter and receiver functions are often separated in order to maximize the signal-to-noise ratio (SNR) of a given imaging sequence [92]. Image contrast in MRI is mainly based on inherent properties of biologic tissues; these include proton content (i.e., ^{1}H spin density), longitudinal recovery time (T_1) as well as transverse relaxation times (T_2 and T_2^*) of ^{1}H nuclei [93, 94]. MRI of the brain allows a high level of detail and with the use of higher magnetic fields, animals as small as mice can be imaged. Although MRI is widely available clinically, only certain centers of research have more sophisticated MRI capability at the small-animal, preclinical level. Multimodality, multiparametric imaging in small animals is even less frequently available. Regardless, these technologies are continuously evolving to reduce the costs and scan times as well as improve

Imaging of intranasal delivery

Table 1. Comparison of imaging modalities utilized in intranasal delivery of therapeutics to the brain

Imaging modality	Strength	Weakness	Spatial resolution	Sensitivity
MRI	-No ionizing radiation -Excellent soft-tissue contrast -Superior spatial resolution with multiplanar imaging capabilities -Very versatile and widely available for both preclinical and human imaging studies -Can utilize magnetofection	-Expensive -Gd-based contrast agents can be toxic -Susceptible to patient movement-induced image artifacts -Relatively slow patient throughput -Some patients may experience claustrophobia -Safety hazards for patients with implanted medical devices -Possible thermal injuries in the body and hearing issues	+++++	++
CT	-Provides detailed images of many tissue types, including osseous tissue -Can image soft tissue, bone and blood vessels simultaneously -Relatively inexpensive and fast compared to MRI -Unlike MRI, patients with implanted medical devices are safe inside a CT scanner -CT is less sensitive to patient motion than MRI -Can complement PET or SPECT, both clinically and preclinically -Micro-CT is available for laboratory use	-Involves ionizing radiation -Patients may experience adverse reactions to contrast agents -Generally, not recommended for pregnant women	++++	+
Gamma Scintigraphy	-Easy to use, fast and inexpensive -Provides functional information -Can be used in drug discovery and development to facilitate pharmacokinetic/pharmacodynamic and biodistribution studies -Higher spatial resolution than SPECT	-Involves ionizing radiation -2D images with poor spatial resolution compared to MRI or CT -no CT or MR combination for anatomy overlay -Lower detection sensitivity compared to SPECT -Requires physical collimators that reject photons that are not within a very limited angular range, thereby decreasing sensitivity compared to PET	+++	++
SPECT	-Enables noninvasive visualization of biodistribution of radiolabeled tracers for diagnostic applications and assessment of treatment efficacy -Utilizes common radiopharmaceuticals, like Tc-99m, that are widely available -Relatively inexpensive -Can be employed in a dual-modality system (SPECT/CT) -Can do multi-isotope imaging (i.e., multi-radioisotope resolution) -Can allow for widening observational time window of imaging due to the longer half-life of single photon emitters	-Involves ionizing radiation -Less quantitative than PET -Requires collimation which introduces noise, decreases sensitivity, and increases san time -Relatively poor spatial resolution compared to MRI or CT	++	+++
PET	-More sensitive than SPECT (two to three orders of magnitude) -Many radiopharmaceuticals are available -Short-lived radionuclides used in PET improve detection sensitivity -Quantitatively accurate -Most often as a molecular imaging modality combined with CT and most recently with MRI -Micro-PET is available for animal studies	-Involves ionizing radiation -Expensive -Requires complex equipment -Quantitative data analysis depends on specialized software tools -Relatively poor spatial resolution compared to MRI or CT	++	+++++
Optical	-Safe, sensitive, widely available, inexpensive with high spatial resolution -Nonionizing radiation -Fast (e.g., multiple animals can be imaged at once, reducing imaging operation time and costs) -Can be used to monitor disease progression, therapeutic efficacy and molecular processes	-Unusable for deep tissues -Cannot be performed non-invasively in vivo on brain easily secondary to skill	++++++	++++++

software interfaces for the use of MRI in both the clinical realm and the investigational setting in both humans and animals.

Contrast agents utilized in MRI include gadolinium-based contrast agents (e.g., gadolinium-diethylenetriamine pentaacetic acid (Gd-DTPA)) and iron-containing agents. Gadolinium-based agents allow for contrast enhancement and image brightening by shortening T_1 times of hydrogen nuclei in contrast agent-containing biologic tissues, further delineating regions of interest (e.g., tumors). Iron, on the other hand, is visualized using T_2- or T_2^*-weighted MRI parameters by shortening T_2 times and inducing a hypointense signal. Moreover, by utilizing fluid- or fat-eliminating techniques (e.g., FLAIR, STIR, and T2 fat saturation), the pathology can often be better visualized. Certain sequences, including gradient recalled echo (GRE) and susceptibility-weighted imaging (SWI), detect hemorrhage or calcification through what is known as a blooming artifact. In addition to static imaging, MRI can be used to collect dynamic information such as with various perfusion techniques, which are more commonly utilized in stroke and tumor imaging. Examples of perfusion techniques include dynamic susceptibility contrast, dynamic contrast enhancement and arterial spin labeling. Another MRI technique that can detect the diffusion of water through space is known as diffusion-weighted imaging (DWI). DWI is the clinical workhorse for the detection of stroke and abscesses. Diffusion tensor imaging (DTI) is another diffusion-related sequence which analyses the three-dimensional shape of the diffusion of water in space to generate an image. Similarly, functional MRI (fMRI) indirectly measures oxygen utilization in certain resting states or activated brain regions to generate regional maps of brain activity.

In animals, MRI can be performed at baseline and following therapy to assess changes in the brain compared with the original baseline. Examples include animal models of brain tumors such as glioblastoma [59, 74, 83], stroke [95] autistic spectrum disorder [96], multiple sclerosis [97], and neuroinflammation [98]. Using DTI and metric fractional anisotropy, IN delivery of myelin oligodendrocyte glycoprotein (MOG_{35-55}) was shown to ameliorate progression of disease and reduce brain damage in a mouse model of multiple sclerosis [97]. The neuroprotective peptide, NAP (part of the 8 amino acids in NAPVSIPQ) also called davunetide (CP201), which is derived from activity-dependent neuroprotective protein (ADNP) was pioneered by Dr. Gozes and her team. This promising agent has been shown to be neuroprotective in numerous neurodegenerative animal models of disease, including Alzheimer's disease, Parkinson's disease, frontotemporal dementia and amyotrophic lateral sclerosis [96]. Most recently, the group demonstrated the neuroprotective effects of NAP augmented by the penetration enhancer chorabutanol in ADNP+/- mouse model of autistic-like ADNP syndrome. Using a 7-tesla MRI unit for in vivo imaging of seven eight-month-old mice, NAP protected against abnormal increases in DTI-derived mean diffusion and fractional anisotropy in the hippocampus in the ADNP+/- mice following IN delivery of NAP, demonstrating its translatability to clinical practice. In an interesting study, Zhang et al. utilized DTI-derived fractional anisotropy and other histologic techniques to demonstrate a regenerative role of interleukin-4 (IL-4) beyond its known immunoregulatory functions in an experimentally induced middle cerebral artery occlusion mouse model [95]. IL-4-loaded liposomal NPs were administered intranasally at 1-7 days, 14 days, 21 days and 28 days following middle cerebral artery (MCA) occlusion and was found, using in vivo DTI on a 9.4-tesla MRI system and histologically, to improve white matter integrity. Long-term sensorimotor and cognitive deficits also improved in the IL-4 NP-treated group compared with vehicle-treated mice.

Direct localization of therapeutic agents in MRI have so far been limited to nanosystems and cellular therapies. For instance, a cholera toxin B subunit-derived NP was found in the hippocampus at one hour after IN delivery in a mouse [99]. By tagging the cholera B toxin NPs with Cy5.5 (an internal fluorescence probe that served as a model drug) and Gd^{3+} (an MRI contrast agent), 7-tesla MR images were obtained in vivo followed by ex vivo histologic and fluorescence microscopy of brain sections. Although the authors claimed that the cholera toxin could be a nanosystem for the treatment of Alzheimer's disease and could target the hippocampus, a therapeutic drug was not delivered and a mouse model of Alzheimer's dis-

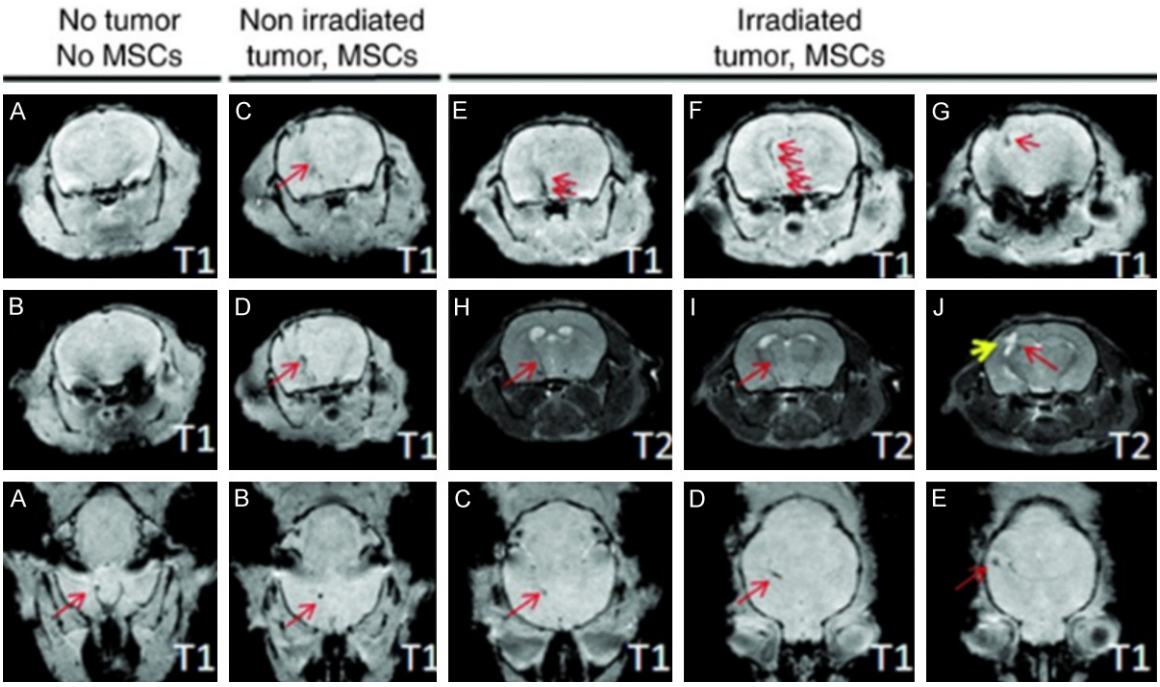

Figure 4. High-resolution T_1- and T_2-weighted MRI of intranasally administered MSCs. (Adapted from Balyasnikova et al., 2014 with permission). High-resolution T_1- and T_2-weighted MRI of intranasally delivered MSCs, loaded with MPIOs, were visualized migrating to the brain of irradiated intracranial glioblastoma-bearing mice to a greater degree than non-irradiated glioblastoma-bearing mice. Top two rows are in the coronal plane and bottom row is an axial plane. Red arrows point to dark signal representing the MPIOs.

ease was not utilized in this study [99]. In another study, MRI was utilized by Balyasnikova et al., to demonstrate the localization of MSCs to the tumor site in an animal model of glioblastoma at 48 hours following IN delivery [83]. The MSCs were engineered to express TNF-related apoptosis-inducing ligand (TRAIL) on the cell membrane for improved therapeutic efficacy in an irradiated glioblastoma mouse model. Additionally, the MSCs were loaded with micron-sized paramagnetic iron oxides (MPIOs) and then delivered intranasally to the brains of irradiated and non-irradiated mice with glioblastoma. The mice were then imaged 48 hours later with MRI utilizing a high-resolution, T_2-weighted rapid acquisition with relaxation enhancement (RARE) spin-echo images and multi-slice, high-resolution, T_1-weighted, fast low-angle shot (FLASH) gradient-echo sequences (**Figure 4**). Importantly, the authors utilized a clinically relevant imaging modality for the first time to demonstrate delivery of MSCs to the brain from the nose. More recently, Spencer et al. intranasally administered NSCs loaded with superparamagnetic iron oxide nanoparticles (SPIONS) with methimazole to a mouse model of glioblastoma [59]. The mice were imaged at 24 hours, 48 hours, and 120 hours following NSC treatment using a 7-tesla Bruker MR scanner. The pre-treatment addition of methimazole delayed mucociliary clearance of the NSCs from the nasal cavity for 24 hours and amplified localization to the tumor site to a greater extent than without a pre-treatment methimazole administration. Another study demonstrated IN delivery of insulin in a rat model of moderate traumatic brain injury (TBI) by MRI, performed at days 3 and 9 post injury, to result in a significant decrease in hippocampus lesion volume [100]. ^{18}F-fluorodeoxyglucose (^{18}F-FDG) PET imaging was also performed on days 2 and 10 to demonstrate reduced inflammation and decreased cerebral glucose uptake, which are additional attestations to the therapeutic efficacy of insulin in TBI following IN delivery in this same animal model.

Furthermore, IN delivery of the anti-inflammatory and neuroprotective agent cyclosporine-A, contained within an oil-based, omega-3 fatty acid-rich flaxseed NE system, demonstrated therapeutic efficacy by inhibiting proinflamma-

tory cytokines in lipopolysaccharide-induced rat model of neuroinflammation as compared to a similar solution formulation without NE [98]. The T_1 MRI contrast agent gadolinium was complexed with the same NE system in place of cyclosporine-A. Using a 7-tesla MRI unit, the authors showed a higher uptake of the NE-gadolinium conjugate in major regions of the brain when dosed intranasally based on changes in T_1 relaxation times. Since cyclosprin-A does not appear to also have been included in the MR-imaged preparation, the results can only be used to indirectly imply that the cyclosprin-A also reached this location in the brain.

A novel theranostic application is to utilize the high magnetic force of MRI to guide magnetic therapeutic agents to the desired location in the brain, a term that has been described as magnetic transfection or magnetofection. For instance, in a mouse model of TBI, chitosan- and polyethyleneimine-coated magnetic micelles were evaluated as a potential MRI contrast agent using a reporter DNA delivered to the brain after mild TBI [101]. Magnetofection was also used to increase the concentration of the chitosan- and polyethyleneimine-coated magnetic micelles in the brain, suggesting the possibility of using these as theranostic delivery vehicles.

With regards to human imaging of IN delivery, a multitude of recent articles have been published to demonstrate the effects of insulin and oxytocin on various CNS conditions (for a recent review of insulin, see Santiago and Hallschmid, 2019 [102] and for recent reviews of oxytocin, see Ding et al. [103], De Cagna et al. [104], and Horta et al. [105]). IN insulin is predominately being studied as a modulator of metabolic control (i.e., obesity and diabetes) and memory (i.e., mild cognitive impairment and Alzheimer's disease) [102]. Oxytocin, on the other hand, is being studied in categories that include stress and anxiety, metabolism and weight, social engagement and bonding and pain and inflammation [105]. In a study examining the effects of insulin on memory in Alzheimer's patients, 3D MRI volumetry using 3D T_1 volumetric magnetization prepared rapid gradient echo (MPRAGE) sequences correlated with improved cognition and daily function following IN delivery of insulin [106]. In particular, for patients who experienced improvement in their memory following IN delivery subregional brain MRI volumes of the middle cingulum, cuneus, hippocampus, superior frontal, and parietal regions, were higher in Alzheimer's patients compared with normal patients. In another study, arterial spin labeling MRI perfusion was utilized to measure central insulin action in the brain following IN delivery in lean, overweight, and obese adults to identify brain regions affected by insulin resistance. Insulin action was selectively impaired in the prefrontal cortex in 23 overweight and obese adults compared to 25 healthy control patients, potentially by promoting an altered homeostatic set point and reduced inhibitory control contributing to an over-eating behavior [107].

Since insulin is one of the most extensively studied agents in clinical trials following IN delivery, an fMRI study was performed to assess three commercially available insulin nasal delivery devices [108]. fMRI revealed a significant decrease in regional blood flow in areas dense in insulin receptors in the intranasally delivered insulin group compared to saline alone. Also, using fMRI, oxytocin (24 IU) or placebo was delivered intranasally to 15 healthy patients in a randomized, double-blind manner to affect the precuneus and amygdala, key brain regions in social cognition and introspective processing [109]. In the nasal oxytocin study, fMRI measuring amygdala activity showed that body dysmorphic patients had higher baseline resting state functional connectivity compared to placebo, which was reversed by oxytocin IN delivery. fMRI identified highly detailed and specifically localized areas of functional connectivity between brain regions [110]. In a separate study in humans, perillyl alcohol was delivered intranasally for the treatment of glioblastoma and lower grade gliomas in patients also receiving surgery, radiotherapy, and chemotherapy. Perillyl alcohol was found to be safe and demonstrated anti-tumor activity as assessed by MRI and CT after six months of treatment [111].

Positron emission tomography

PET is a promising, highly quantitative and sensitive imaging tool used in disease diagnosis as well as the prediction and assessment of therapy response [112]. Being a sensitive imaging

system, PET enables us to quantitatively understand physiological processes and pathways within the body at a fundamental level. From a therapy standpoint, PET holds probably the greatest potential for the development of theranostic agents. PET images depict the distribution of positron (β^+ particle)-emitting radionuclides (e.g., fluorine-18 (^{18}F), rubidium-82 (^{82}Rb), oxygen-15 (^{15}O), nitrogen-13 (^{13}N), carbon-11 (^{11}C), zirconium-89 (^{89}Zr), and copper-64 (^{64}Cu)) in the body. Emitted positron moves within tissue and deposits its kinetic energy. Upon meeting a free electron in tissue, a mutual annihilation occurs, producing two 511 keV gamma photons (511 keV is the energy equivalent to the rest mass of an electron or positron). These two photons are emitted back-to-back, propagating outward from the site of annihilation 180 degrees apart. Therefore, PET scanners detect a pair of 511 keV photons in what is called annihilation coincidence detection (ACD) in order to obtain projections of radioactivity distribution in the patient. With this approach, only simultaneous gamma rays are detected (with multiple rings of detectors surrounding the patient) and declared as events. A time interval (or time window), typically 2-20 nanoseconds for modern scanners, set by the user determines whether two detected photons are declared as "simultaneous" [113].

The majority of PET systems are coupled to CT scanners (PET/CT systems), though there is a growing interest in PET/MRI systems recently for both clinical pre-clinical studies. By detecting the biodistribution of radiopharmaceuticals in the body, PET studies enable the diagnosis of a wide array of clinical conditions, including cancer, dementia, epilepsy, Parkinsonism as well as cerebrovascular and cardiovascular diseases. There are many PET radiopharmaceuticals, with new radiotracers and their associated ligands being developed extensively [114]. Clinically, the most widely used radiopharmaceutical is ^{18}F-FDG, which is a glucose analog that detects elevated metabolism in the body [115]. ^{18}F-FDG PET has also been utilized in the detection of malignant lesions, staging cancer patients as well as assessing tumor treatment response [113]. Typically, the results are reported in the form of a standard uptake value (SUV) which is calculated based on the time of injected dose, the patient or animal's body weight and the radionuclide rate of decay.

Advantages of PET include its high quantitation and sensitivity relative to other modalities and its ability to co-register with CT and MRI. For instance, compared to other radionuclide imaging techniques (e.g., SPECT), PET enables a greater detection sensitivity over a given period of time with its relatively short-lived radionuclides. That is, because PET utilizes radionuclides with shorter physical half-lives compared to SPECT, greater activities can be injected in patients without an increase in the overall radiation. However, PET has several limitations. The most important limitation is poor spatial resolution relative to MRI or CT (**Table 1**). PET also has a relatively high cost with complex equipment, requiring trained personnel and specialized software [116]. Radiation exposure is also a risk to patients [117]. With regard to FDG, one major limitation is that elevated metabolism detected by ^{18}F-FDG is found in both normal and abnormal tissues which reduces background to noise ratio. This is because there is a typically high baseline glucose utilization in the brain. Pathologic entities that would have high metabolism include abnormal inflammation, tumors, cardiovascular disease, and brain disorders including dementia, epilepsy, Parkinson's disease, stroke, and TBI [118].

As described in the MRI section, ^{18}F-FDG PET and MRI were combined to study the effects of IN insulin on cerebral glucose uptake, lesion volume, memory and learning, and inflammation using a controlled cortical impact (CCI) TBI model in rats [100]. A significant reduction in ^{18}F-FDG uptake was observed in the hippocampus on PET imaging along with a significant decrease in the hippocampal lesion volume on MRI, indicating that IN insulin may be a viable therapy for TBI.

Orexin A (hypocretin-1) is one of two isoforms of endogenous neuropeptides produced in the hypothalamus that plays an important role in modulating the sleep/wake cycle, energy and homeostasis, appetite and feeding, drug addiction and cognition [119]. Orexin A can be delivered intranasally with good efficacy [120] and exerts a neuroprotective and anti-inflammatory effect against various CNS disease states [119]. Despite ample evidence that orexin A can be delivered to the CNS intranasally, Van de Bittner et al. was unable to demonstrate CNS delivery following IN administration of

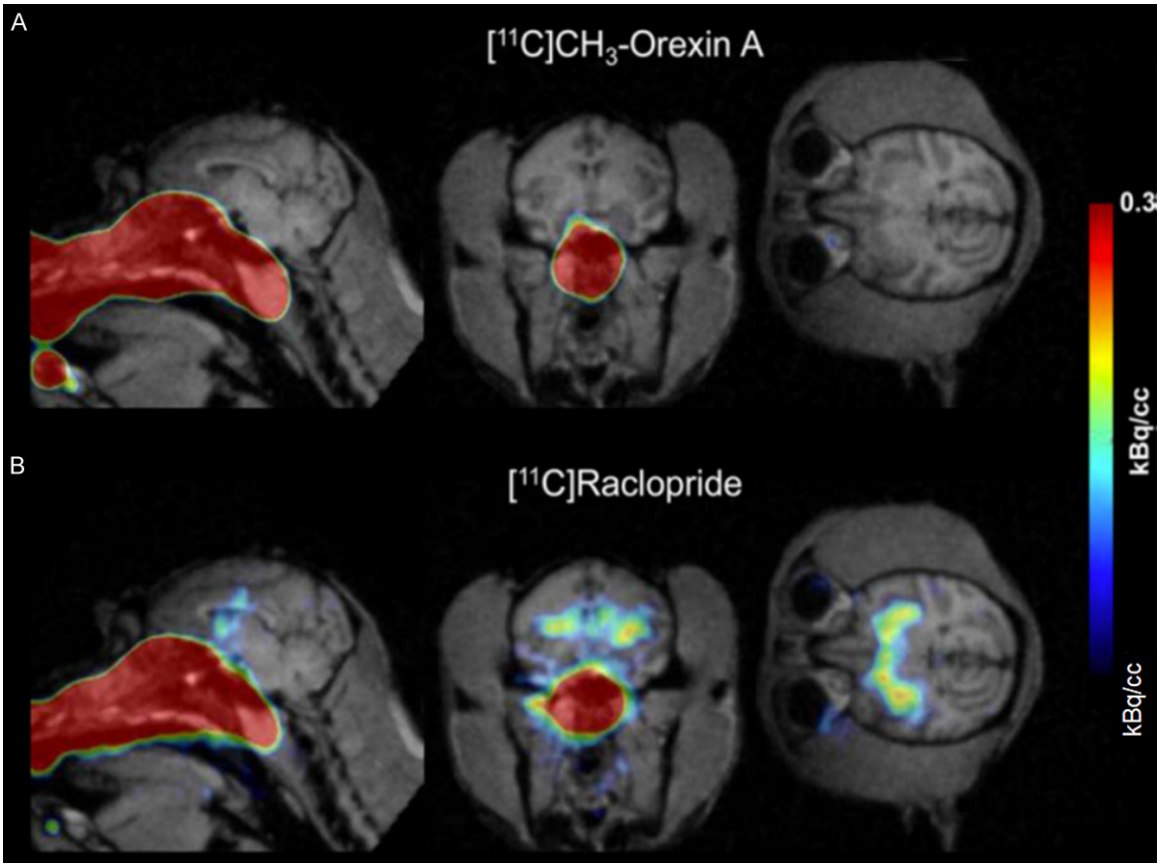

Figure 5. PET/MR of ^{11}C-CH_3-Orexin A and ^{11}C-raclopride in the brain and nasal cavity after intranasal delivery to the neuroepithelium. (Reprinted from ref. 122. Copyright 2018 American Chemical Society) Comparison of ^{11}C-CH_3-Orexin A and ^{11}C-raclopride uptake in rhesus macaque brain after intranasal administration. ^{11}C-CH3-Orexin A (A) and ^{11}C-raclopride (B) were administered using a device for intranasal delivery to the neuroepithelium. At 90 minutes, ^{11}C-CH_3-Orexin A was not visible in the brain using PET/MRI, while ^{11}C-raclopride was readily visible in the basal ganglia.

a ^{11}C-radiolabeled form of orexin A (^{11}C-CH_3-Orexin A) compared with ^{11}C-raclopride using PET/MR in either rats or non-human primates (**Figure 5**) [121]. Furthermore, in a safety and efficiency trial of a nasal vaccine against botulism, PET imaging of the botulinum type A neurotoxin (BoHc/HA), labeled with ^{18}F (i.e., ^{18}F-BoHc/A), did not demonstrate uptake into the cerebrum or olfactory bulb, despite being highly protective against botulism in non-human primates [122]. Nevertheless, PET/CT followed by fusion with MRI was shown in a rat model to be feasible for pharmacokinetic studies using compartmental modeling following IN delivery of the ^{18}F-FDG radiotracer [123]. The authors were able to generate a time-activity curve after acquiring the data in list-mode from 0.5-30 minutes following IN delivery to demonstrate regional differences in permeability of the radiotracer in the nasal cavity. The authors concluded that absorption and distribution of drug in the rat nasal cavity can be quantitated using PET imaging, but FDG was not detected in the brain after IN delivery. These results are similar to another report that assessed IN delivery of FDG in humans [124]. The reason for this may be saturation of local tissues since these too have glucose transporters that would sequester FDG and prevent more distant perfusion for brain entry.

In a recent clinical trial, an increase in brain metabolic activity was found in patients with Alzheimer's disease and mild cognitive impairment after four months of IN insulin when imaged by PET following IV administration of ^{18}F-FDG [125]. There was no change in the placebo group. As mentioned earlier, another therapy that is amenable to IN administration is

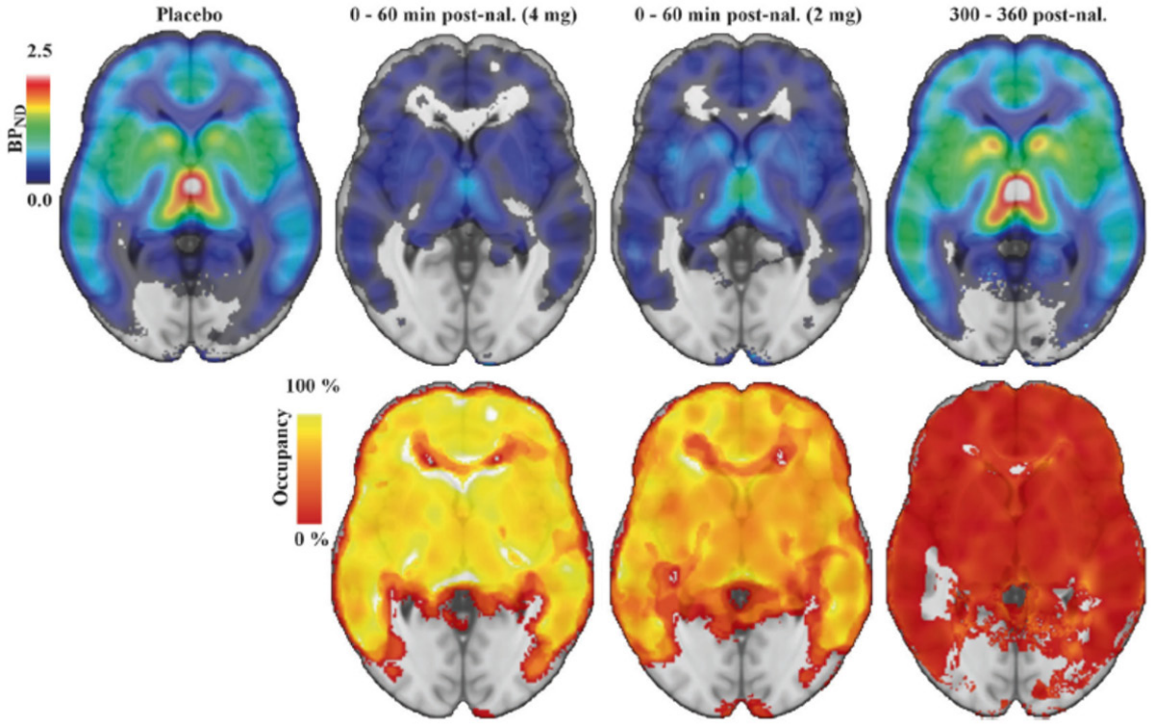

Figure 6. ^{11}C-Carfentanil PET imaging of the brain following intranasal naloxone at 0-60 min or 300-600 min. (Adapted from Johansson et al., 2019). ROI-based binding potential was determined using PET imaging of ^{11}C-Carfentanil superimposed on a brain MRI template without naloxone administration (upper left image), at 0-60 min following 4 mg of naloxone (upper second image from left), at 0-60 min following 2 mg naloxone (upper third image from left), or at 300-360 min following 2 or 4 mg naloxone. The bottom row indicates percent occupancy of naloxone relative to placebo at the doses administered in the upper row. BP_{ND} is the binding potential of [^{11}C] carfentanil relative to the uptake of the tracer in the non-displaceable compartment.

oxytocin. Oxytocin inhibits the amygdala, decreases anxiety and modulates depression and autism when delivered intranasally. Using a radiolabeled partial antagonist to 5-hydroxy-tryptophan-1 receptors and PET/MRI, Mottolese et al. demonstrated in a randomized, double-blind control in humans that oxytocin modulates the serotoninergic system by regulating the 5-hydroxy-tryptophan-1 receptor network, providing an important mechanism of action for oxytocin in humans [126].

Naloxone (Narcan) is a life-saving medication that can rapidly reverse opioid overdose and is available in various forms of administration, including IN [127]. In a study demonstrating the advantages of in vivo imaging, quantitative localization of intranasally delivered naloxone was demonstrated in the brains of 24 healthy male adult human subjects using ^{11}C-Carfentanil PET imaging combined with brain MRI (**Figure 6**) [128]. Rapid mu opioid receptor occupancy of naloxone following IN delivery was demonstrated directly for the first time in this study and fit well with the rapid (< 5 minutes) reversal of opioid overdose. The authors proposed that naloxone's rapid onset and half-life occupancy of mu opioid receptors of about 100 minutes could be useful for other addictive states such as addictive gambling and alcohol dependence in situations where clinical trials of longer acting mu receptor antagonists have been less efficacious [130].

Zolmitriptan is a selective serotonin 5-HT1B receptor agonist that can be delivered orally or intranasally for the treatment of migraine headaches [129]. When delivered intranasally, the onset of action is detectable within 10 minutes and can quickly abolish major migraine symptoms [130]. Drug biodistribution studies in the nasopharynx, brain, lung, and abdomen were conducted using PET following IN administration of ^{11}C labelled zolmitriptan (^{11}C-zolmitriptan) [131]. In phase 1, the group determined the most appropriate times for PET scanning, whereas in phase 2, they validated the distribution, pharmacokinetics, and tolerability of ^{11}C-zolmitriptan. Healthy volunteers, aged 18-28 years, were scanned over sectors covering

one of the nasopharynx, brain, lungs or abdomen for up to 1.5 hours post dose by PET. It was determined that most of the ^{11}C-zolmitriptan was detected in the nasopharynx immediately after IN administration. Moreover, that was a detectable radioactivity within brain tissue, thereby suggesting central penetration of the drug [131].

Single-photon emission computed tomography

SPECT is a nuclear tomographic imaging technique that depicts the distribution of gamma-ray-emitting radionuclides (e.g., technetium-99 (^{99m}Tc), thallium-201 (^{201}Tl), ^{123}I, and ^{131}I), acquiring planar (projection) images from multiple angles. These projection images are combined to reconstruct a 3D image depicting the distribution of radionuclides in patients. It depends on radiopharmaceuticals labelled with radionuclides whose radioactive decay produces gamma photons directly. ^{99m}Tc serves as the workhorse for PET imaging and is the most common radionuclide used due to its short half-life [132]. The most common method of performing SPECT is with a rotating gamma camera mounted on a special gantry that allows up to 360-degree rotation around the patient so that photons are captured in multiple directions. Some recent SPECT systems employ more than one gamma camera head, reducing scan time. In single-head SPECT systems, the gamma camera is rotated either 180 degrees (for most cardiac imaging applications) or 360 degrees (for most non-cardiac imaging applications) so that a standard projection (planar) image is acquired at each angle. Transverse images are reconstructed from the projection data on the system's computer [92]. Like PET, SPECT allows for the freedom to work with other modalities like CT or MRI. Additionally, SPECT scans are far less expensive than PET scans (**Table 1**). However, SPECT is less quantitative than PET. It is also less sensitive than PET because it requires physical collimators that reject photons that are not within a very limited angular range. The collimation requirement in SPECT also introduces noise and increases san time.

At the preclinical level, Esposito et al. tested a ^{99m}Tc-labeled nanostructured lipid carrier (NLC) (based on a tri-block copolymer platform) distribution using SPECT following IN, intraperitoneal, IV and oral administration in a Wistar rat model as a potential therapeutic application for obesity or other metabolic disorders [133]. The in vivo study demonstrated stability of the NLCs, indicating suitability of the system to carry both drugs and radiotracers for both therapeutic and diagnostic applications. Activity was visualized in the nasal cavity but not in the brain [133]. In addition, Mandlik et al. used ^{99m}Tc-labelled, zolmitriptan-loaded nanocarriers for in vivo analysis of efficient drug targeting, biodistribution, and kinetics for the treatment of migraines [134]. The anti-migraine zolmitriptan-loaded into radiolabeled nanostructured polymeric carriers and delivered intranasally to Swiss albino mice. The ^{99m}Tc radiolabelled nanocarriers were efficient in targeting the brain, resulting in higher zolmitriptan-loaded concentrations compared to intranassally delivered unencapsulated free drug solution (i.e., ^{99m}Tc-zolmitriptan) and intravenously delivered ^{99m}Tc-labelled, zolmitriptan-loaded nanocarriers. The authors were able to monitor the biodistribution of each therapy by a coupled bimodal SPECT-CT system. Due to the increased radioactivity found in the brain from analysis of the scintigrams and pharmacokinetic parameters, attesting to a more superior drug targeting, it was concluded that intranasally delivered zolmitriptan-loaded nanocarriers are a much more promising system than free drug solution or intravenously delivered drug-loaded nanocarriers.

There are very few available studies specifically utilizing SPECT to study IN delivery in humans. In one study, the clinically approved radiotracer thallium-201 (^{201}Tl) was administered intranasally in 24 humans in an attempt to visualize the nose-to-brain route using SPECT/CT fused with MR images of the same subjects [135]. ^{201}Tl was visualized in the olfactory bulb at 24 hours following IN delivery through the anterior skull base via the cribriform lamina. More recently, olfactory bulb uptake of ^{201}Tl was demonstrated in healthy human subjects following IN delivery. This was significantly lower in anosmic patients [136] (**Figure 7**). SPECT/MRI with nasal ^{201}Tl is a dual-modality technique that can be used to assess the olfactory nerve function [136]. In another study, SPECT/MRI was used 24 hours post ^{201}Tl injection to assess the olfactory nerve connectivity in post-traumatic patients. There was a significant decrease of ^{201}Tl detection in olfactory-impaired patients [136].

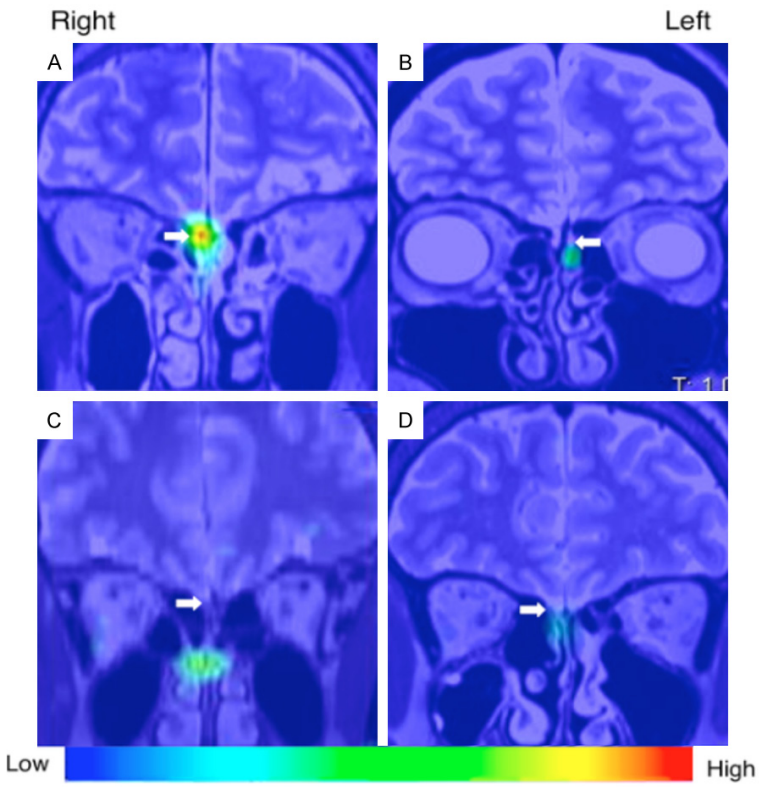

Figure 7. SPECT-MR imaging of ^{201}thallium following intranasal delivery in a human (adapted from Shiga et al., 2013 with permission). Representative SPECT images acquired 24 hours after unilateral intranasal delivery of ^{201}Tl in 10 healthy volunteers and 21 patients with olfactory dysfunction from various causes. The SPECT images were fused with MRI images from the same patients. ^{201}Tl was shown to migrate to the olfactory bulb (white arrows) which was significantly correlated with odor recognition thresholds and volume of the olfactory bulb on MRI.

Gamma scintigraphy

Gamma scintigraphy is a nuclear medicine imaging approach that uses the same gamma-emitting radiotracers used in SPECT such as ^{99m}Tc and ^{201}Tl. The drug-labelled radionuclide (i.e., radiopharmaceutical) emits gamma rays from the organ/tissue where it is localized; these rays are detected by external gamma cameras, forming a 2D projection image which depicts the biodistribution of the gamma-emitting source in the body. Gamma scinitigraphy is often used as an in vivo IN imaging technique preclinically because it is readily available, fast, and inexpensive (**Table 1**). However, some drawbacks include its ability to only produce 2D/planar images, relatively poor spatial resolution compared to MRI or CT, lower detection sensitivity than PET or SPECT, and the deposition of radiation dose.

Recently, ropinerole-loaded mucoadhesive NPs [137], lorazepam-loaded PLGA NPs [138], and risperidone-loaded solid lipid NPs [139], labeled with ^{99m}Tc, demonstrated greater brain concentrations after IN delivery compared to IV delivery. In a proof-of-concept study, Kakkar et al. reported that circumin-loaded lipid NPs could be visualized in a New Zealand rabbit brain at 4 hours following IN delivery using gamma scintigraphy, but was not visualized in the brain following IV delivery [140]. Unfortunately, the images provided show only a dorsal view without correlational, cross-sectional imaging to distinguish between signals in the nasal cavity versus signal in the brain. Gamma scintigraphy in rats was performed following IN administration of ropinerole hydrochloride-loaded chitosan NPs to ascertain the localization of drug in the brain following IN administration of formulations [137]. The brain-to-blood ratios obtained at 30 minutes are indicative of direct nose-to-brain transport, bypassing the BBB. This study, too, suffered from the lack of verifiable anatomic localization since the nasal cavity cannot be delineated from the brain in these images using planar imaging alone.

One key component to efficient nose-to-brain delivery in humans is the development of a nasal drug delivery device that facilitates focal deposition of the drug onto the dorsal nasal epithelium. Various companies market this ability using various technologies, including bidirectional technology (Optinose^{TM}) [141], controlled particle dispersion technology (Kurve Technology) and Precision Olfactory Delivery (POD) technology (Impel Neuropharma) [142]. As an illustration, Optinose developed a breath-powered device with a nasal piece that extends beyond the nasal valve in the nasal cavity. In one study, gamma scintigraphy images were

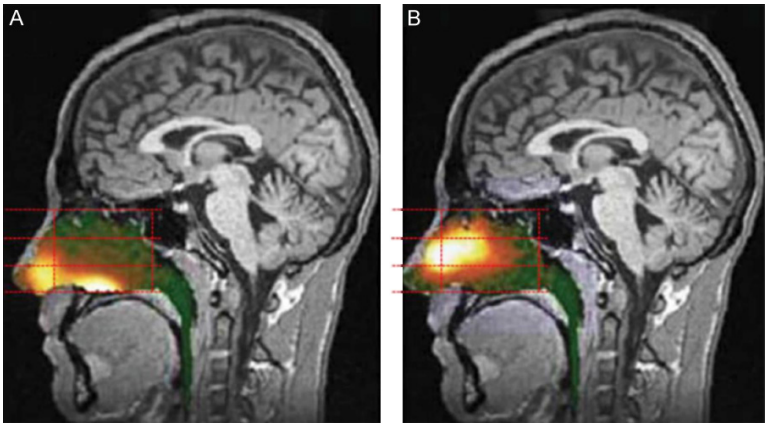

Figure 8. Gamma scintigraphy of an example of a breath-powered nasal spray. (Figure included with permission from Djupesland et al., 2013.) Gamma camera images 2 minutes after delivery using a traditional liquid spray (A) and powder with OptiNose Breath-Powered Device (B) shown with a logrithmic hot iron intensity scale. Initial gamma images from one of the subjects are esuperimposed on a lateral MR image. The red dotted lines indicate the segmentation used for regional quantification.

obtained 2 minutes after the delivery of a traditional spray using an Optinose breath-powered device (**Figure 8**) [142]. Images were superimposed on a lateral MRI image. The Optinose breath-powdered device was superior for demonstrating a broader deposition on ciliated respiratory epithelium in the nasal cavity, especially in the upper and middle posterior regions. There was less deposition in non-ciliated nasal regions, which are thought to be less important in nasal drug delivery.

Computed tomography

Computed tomography has had a limited role in nose-to-brain drug delivery largely because of its lower soft tissue contrast and lower sensitivity of detection compared to MRI and nuclear medicine, respectively. However, CT has been useful in characterizing the nasal anatomy and dynamic airflow in small animals and humans, which are important for testing IN delivery methods [143]. CT utilizes x-rays to generate cross-sectional, gray-scale images with various pixel (or voxel) intensity values Hounsfield Units (HU) [144]. The degree to which soft tissues attenuate x-ray photons and prohibit them from reaching the detectors determines the image characteristics [145]. CT is widely available, relatively inexpensive, and its images can be acquired quickly compared to other imaging modalities such as MRI (**Table 1**). However, the use of CT involves ionizing radiation, which has the potential for deterministic and stochastic side effects to patients [144, 145], making it not recommended for pregnant women. Also, patients may experience adverse reactions to its iodine- and barium-based contrast agents.

While CT has not been utilized as a standalone imaging modality for IN delivery, it has indeed been used as an adjunct anatomical modality along with dynamic imaging such as PET [123] and SPECT [134]. Furthermore, in animals, the upper and lower airway morphology in Sprague-Dawley rats was studied using micro-CT and image segmentation techniques [146]. The combination of high-resolution, static micro-CT scans with dynamic micro-CT scans was used to assess the deposition patterns of inhaled particles for obligate nose breathers like the rat [146]. In another study, three-dimensional CT was used to study the to pography of the nasal and paranasal sinuses, which were compared with corrosion casting and gross and histologic cross-sections [147]. In humans, Warnken et al. utilized CT to create an anatomical 3D-printed model of the nasal cavity for both pediatric and adult patients to evaluate the deposition pattern of several IN agents [148]. CT was also used for an in vitro model of the nasal cavity to determine the penetration of a nasal spray or the deposition of the olfactory nerve [149, 150]. Furthermore, Shang et al. used CT to reconstruct a human nasal cavity model to better understand mucociliary clearance by examining mucus flow patterns [151]. Often, as mentioned earlier, CT is used in conjunction with other modalities to gain a better understanding of the intra-nasal delivery. In fact, CT can be used for anatomic correlation when combined with PET or SPECT since these modalities have inherently poor anatomic spatial resolution. CT also allows attenuation correction, reducing attenuation artifacts and enabling an improvement in the overall diagnostic performance greater than either modality alone [92].

Optical imaging

Optical imaging techniques, particularly BLI and FLI, provide in vivo information at the preclinical level on disease (e.g., tumor) progression [152] and treatment biodistribution [152, 153]. Both BLI and FLI quantify light production for spatial and anatomical information during real-time studies through individual processes [154]. BLI relies on an enzymatic reaction as chemical energy converts into light energy without an excitation source [155]. The complete reaction uses luciferase genes in the presence of a substrate, an energy source and oxygen [154]. Substrates include an endogenous reduced riboflavin phosphate ($FMNH_2$) and long-chain aliphatic aldehyde or exogenous coelenterazine and D-luciferin [152, 154], which can be combined with luciferases such as *Gaussia princeps* luciferase (Gluc) [152, 155] or firefly luciferase (Fluc) [59, 156]. Because of newer cloning and transfection techniques, genes coding for the enzyme and substrate can be introduced into cells for imaging [157]. For example, inserting the *lux* operon into a plasmid or chromosome catalyzes the aldehyde substrate and can be monitored at a wavelength of 490 nm [154]. The absence of required external light makes BLI very favorable since there is a unidirectional full conversion from chemical energy to light [155]. BLI avoids toxic contrast agents, ionizing radiation, high cost, and low throughput associated with other techniques such as MRI or CT [157]. Other advantages include ease of use and little to no background signal except in the abdomen from digested rodent chow-containing chlorophyll [154]. Multiple animals can be imaged at once in a single view, which reduces costs and imaging operation time, and the non-invasiveness of the procedure allows for serial in vivo imaging [157]. A major limitation of BLI, however, is that luciferases often do not permit deep-tissue imaging greater than 1-2 cm [154, 155]. This limitation generally prevents optical imaging from being useful in clinical applications where deeper tissue penetration is a requirement. While optical imaging is one of the most sensitive imaging modalities, improved sensitivity needs to come from imaging advancements as well as modified substrates (**Table 1**). For example, NanoLuc is meant to have improved stability as well as increased luminescence; however, its interaction with mammalian tissues currently challenges its use. One group utilized red-shifted luciferins designed based on the combination of synthetic coelentarazine analogs and NanoLuc mutants to improve such sensitivity [158, 159]. BLI is strongly dependent on substrate administration and, therefore, timing and bioavailability are two important factors [154]. If certain animals require different administration times, cost could become quite expensive. Finally, substrate administration is often via tail vein injection which often requires experienced individuals and could pose a challenge to experiments, especially when working with smaller animals such as mice, if the injection is not done correctly.

In a preclinical model, Fuentes et al. used BLI in order to track the distribution of oncolytic virus-loaded NSCs in the presence of methimazole of fibrin glue as a potential treatment option for glioblastoma [59]. Methimazole and fibrin glue were used to enhance penetration of the olfactory epithelium. NSCs were overexpressed with chemokine receptor type 4 to also facilitate travel to the brain and were modified to be Fluc-expressing for BLI. The cells were administered intranasally and D-luciferin sodium salt was injected intraperitoneally and placed inside each nostril. **Figure 9** represents increased brain localization of NSCs in the presence of methimazole at different time points compared to saline and fibrin glue [59]. In both the saline and the fibrin glue groups, it is clear the NSCs either cleared or remained in the nasal cavity. **Figure 9** has been chosen as a representative BLI image because of its sharp resolution and its change longitudinally. BLI images of the brain are often challenging to acquire in mouse models as it is challenging to discern between the nasal cavity and brain. However, here as time continues, the region of interest shrinks and becomes more concentrated at the brain and this evident shift discerns between the two regions.

FLI is a two-step process as it requires an external light with an appropriate wavelength to excite a fluorescent molecule (fluorophore). This fluorophore is excited to a higher energy state and as the molecule relaxes, light is emitted at a different wavelength than the excitation wavelength [154, 157]. There are a variety of proteins that can be used for FLI including

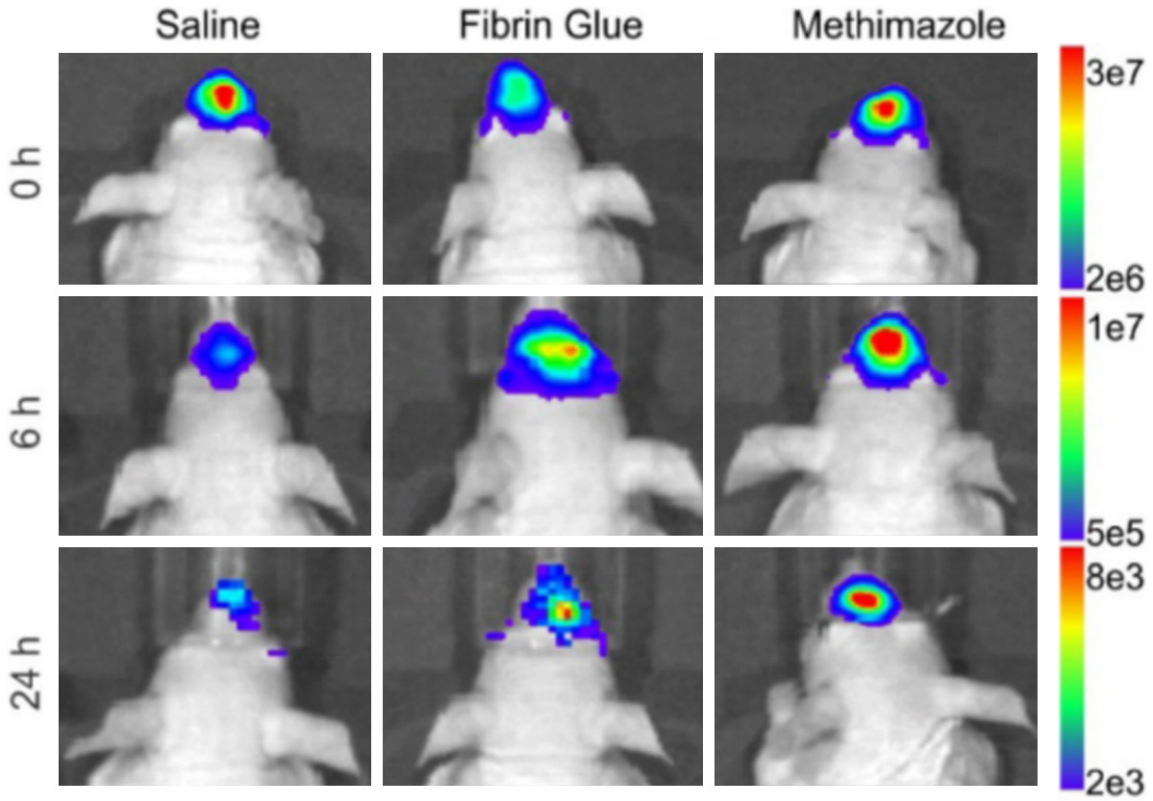

Figure 9. In vivo BLI after IN delivery of NSCs. (Figure adapted, with permission, from Spencer et al., 2019) Oncolytic, virus-loaded NSCs were intranasally delivered in the presence of either fibrin glue, methimazole, or saline. Their distribution was monitored over time using BLI. Methimazole best disrupts the olfactory epithelium to facilitate nose-to-brain transition for the treatment of glioblastoma which is seen from the increased concentration and localized region of interest at the brain.

green fluorescent protein (GFP) [152, 160], Turbo red fluorescent protein (TurboRFP) [154], and mCherry fluorescent protein [152], in addition to metals such as gold [161]. Some advantages of FLI include exquisite sensitivity and specificity, high temporal and spatial resolution, availability, easy to operate and inexpensive (**Table 1**) [157]. FLI also does not involve ionizing radiation and is extremely fast in vivo, with measureable signal available within seconds [154]. On the other hand, FLI has disadvantages such as a smaller limit of detection/penetration depth of only a few millimeters compared to that of BLI and background autofluorescence [154].

Fluorescent molecules can be conjugated to a wide variety of entities, including cells and NPs. For example, Bagheri-Mohammed et al. tagged human endometrium-derived stem cells (HEDSCs) with GFP for a possible treatment of Parkinson's disease [160]. The HEDSCs were administered intranasally and ex vivo fluorescence imaging was performed. It was found that the HEDSCs were able to migrate to the substantia nigra pars compacta and behavior was improved [160]. Another group fluorescently labelled poly(*N*-vinyl pyrrolidone)-based nanogels that were attached to insulin for the treatment of Alzheimer's disease [47]. By fluorescently labelling the nanogel, the group was able to monitor biodistribution and clearance and determine that the mucosa was not altered and brain activity was enhanced [47].

FLI and BLI can be used together to provide more information. In a very interesting study, Carvalho et al. used both FLI and BLI to monitor the distribution of olfactory ensheathing cells (OECs) and their role as a carrier for gene therapy in the treatment of glioblastoma [152]. OECs were modified to carry a fusion protein between cytosine deaminase and uracil phosphoribosyl transferase which converts the pro-

drug 5-fluorocytosine into its cytotoxic metabolite. OECs and OECs labelled with the fusion protein were engineered to express Gluc, while glioblastoma stem cells were modified to express Fluc for an in vitro BLI study measuring viability using two separate substrates, coelenterazine and D-luciferin, respectively. An in vivo BLI study combined with an ex vivo FLI study using the same cell modifications showed a decrease in tumor size in the presence of labelled OECs and 5-fluorocytosine as well as migration of both OECs using the nasal pathway into the glioma site [152]. Briefly, mice were injected with glioma stem cells expressing Fluc and mCherry fluorescent protein and one week later were intranasally administered OECs and labelled OECs expressing Gluc and GFP. The mice were then treated daily with an intraperitoneal injection of 5-fluorocytosine. D-luciferin was injected intraperitoneally at 150 μg per gram of body weight and imaged ten minutes later. The fluorescent proteins were utilized in an ex vivo FLI study to confirm migration to the primary tumor site [152].

Another special type of optical imaging, known as photoacoustic (PA) imaging, takes advantage of short light pulses to excite a region of interest (i.e., absorbing medium), causing a slight temperature rise (in the millikelvin range) and thermoelastic expansion [162]. Consequently, pressure waves emitted at ultrasonic frequencies are recorded by a diagnostic ultrasound transducer that produces a 3D image of the absorbing medium distribution. Compared to traditional optical imaging, this imaging approach provides deeper tissue penetration (up to 5-6 cm) and offers higher resolution due to the weaker tissue scattering of ultrasound waves [162]. By virtue of its capability in visualizing the optical absorption properties of biologic tissues, PA imaging also provides higher tissue contrast than conventional ultrasound imaging (**Table 1**) [163]. Additionally, PA imaging utilizes a nonionizing electromagnetic radiation, similar to BLI and FLI.

Near-infrared (NIR, 650-900 nm) absorptive materials are used as contrast agents to improve PA imaging sensitivity and tissue penetration results [164]. Some studies have used PA with NIR NPs for contrast enhancement, tumor targeting, or multimodal imaging [164]. One study, particularly, incorporated a gold nanorod (GNR) into porous magnetic nanoshells [165]. The highly preserved plasmonic feature of GNRs enabled photothermal-induced PA imaging. Doxorubicin, as a model anticancer drug, was loaded into GNR nanocapsules and, under the guidance of MRI/PA dual-modal imaging and magnetic tumor targeting, a photothermal-chemo synergistic therapy was conducted via NIR laser for a highly efficient tumor eradication. It was shown by H&E stained images, blood parameters, and the bodyweight of treated groups that the NPs were well tolerated [165]; however, the nonbiodegradability and potential long-term toxicity of these nanomaterials impact their clinical translation. Data regarding PA-assisted IN drug delivery remain to be explored.

Conclusions, perspectives and future directions

IN delivery to the brain can be evaluated with in vivo imaging to determine the fate of agents administered through this route and to assess the progression of diseases as well as the effectiveness of therapeutics. Various in vivo imaging techniques have been discussed in this review, highlighting the critical role imaging plays in the assessment of treatment efficacy. This review also discussed the nose-to-brain route as well as preclinical and clinical IN therapies including small molecules, macromolecular agents, nanosystems, cellular therapies and theranostics.

Innovative IN therapies are continuously being developed. Therefore, we believe that there will be an increasingly growing interest and devoted efforts to not only optimize current imaging methodologies but also develop new diagnostic capabilities in order to facilitate the discovery and clinical translation of novel IN therapies to the brain. In particular, molecular and multimodality imaging techniques will likely continue to be at the forefront of development, dominating the aforementioned efforts. PET/MRI, for instance, is an emerging molecular imaging modality that harnesses the strengths of both PET and MRI to produce hybrid quantitative images with exquisite soft tissue contrast. Therefore, we believe, PET/MRI in IN delivery studies is and will continue to be a promising area of research and investigation with a potentially significant clinical impact in the future.

In addition to optimizing and developing imaging capabilities to facilitate IN delivery, future work should investigate strategies that enhance the delivery of drugs across the nasal barriers providing a more localized delivery to specific brain sites. One of these strategies is focused ultrasound (FUS), which is a noninvasive, therapeutic modality that harnesses the mechanical and thermal effects of ultrasonic beams focused at a region of interest in order to induce therapeutic benefits in deep-seated tissues with little or no harm to intervening tissues. FUS, which is FDA approved for certain clinical conditions, has already demonstrated promising initial results supporting its capability in enhancing the efficacy of IN delivery within targeted brain regions [166, 167]. The FUS-mediated transport enhancement of intranasally administered agents utilizes another FDA-approved component, namely microbubbles, in order to induce mechanical effects (cavitation) that facilitate the transport of therapeutics in the brain.

We also believe that combination therapy, delivered intranasally using a NP-based drug delivery system, can bring about significant advantages in treating debilitating brain diseases over single-drug therapies. Moreover, engineering multifunctional NP-based delivery systems that not only incorporate multiple anticancer drugs but also imaging agents as well as targeting moieties would certainly provide added advantages in IN delivery. Such a nanotheranostic platform can enable targeted, image-guided IN delivery to the brain, utilizing one or more of the diagnostic imaging modalities discussed in this review for treatment planning, real-time monitoring and control, as well as posttreatment evaluation of efficacy.

Acknowledgements

The authors would also like to thank Dr. Jason Parker for fruitful discussions. We would also like to thank the Joseph Acchiardo and Philip Marcadis who contributed to reference and data gathering.

Disclosure of conflict of interest

None.

Abbreviations

11C, Carbon-11; 13N, Nitrogen-13; 15O, Oxygen-15; 18F, Fluorine-18; 18F-FDG, Fluorine-18 Fluorodeoxyglucose; 64Cu, Copper-64; 68Ga, Gallium-68; 82Rb, Rubidium-82; 89Zr, Zirconium-89; 90Y, Yttrium-90; 99mTc, Technetium-99; 123I, Iodine-123; 131I, Iodine-131; 177Lu, Lutetium-177; 201Tl, Thallium-201; ACD, Annihilation coincidence detection; ADHD, Attention-deficit/hyperactivity disorder; ADNP, Activity-dependent neuroprotective protein; BBB, Blood-brain barrier; BLI, Bioluminescence imaging; BMSC, Bone marrow-derived stem cell; BoHc/A, 18F-Clostridium botulinum type A neurotoxin; CCI, Controlled cortical impact; CNS, Central nervous system; CSF, Cerebral spinal fluid; CT, Computed tomography; DTI, Diffusion tensor imaging; DWI, Diffusion-weighted imaging; FLASH, Fast low-angle shot; FLI, Fluorescence imaging; Fluc, Firefly luciferase; FUS, Focused ultrasound; Gd-DTPA, Gadolinium-diethylenetriamine pentaacetic acid; GFP, Green fluorescent protein; Gluc, Gaussia princeps luciferase; GNR, Gold nanorod; GRE, Gradient recalled echo; GRAS, Generally regarded as safe; HEDSCs, Human endometrium-derived stem cells; HU, Hounsfield units; IN, Intranasal; IV, Intravenous; IL-4, Interleukin-4; MCA, Middle Cerebral Artery; MIBG, Metaiodobenzylguanidine; MOG, Myelin oligodendrocyte glycoprotein; MPIO, Micron-sized iron oxide particles; MPRAGE, Magnetization Prepared Rapid Gradient Echo; MRI, Magnetic resonance imaging; fMRI, Functional MRI; MSC, Mesenchymal stem cell; MTD, Maximum tolerated dose; NE, Nanoemulsion; NIR, Near-infrared; NLC, Nanostructured lipid carrier; NPs, Nanoparticles; NSC, Neural stem cell; NSPC, Neural stem/progenitor cell; OEC, Olfactory ensheathing cell; PA, Photoacoustic; PEG, Polyethylene glycol; PLGA, Poly(lactic-co-glycolic acid); PET, Positron emission tomography; POD, Precision olfactory delivery; PSMA, Prostate specific membrane antigen (PSMA); PTSD, Post-traumatic stress disorder; RARE, Rapid acquisition with relaxation enhancement; RF, Radiofrequency; SPECT, Single-photon emission computed tomography; SUV, Standard uptake value; SNR, Signal-to-noise ratio; SPION, Superparamagnetic iron oxide nanoparticles; SWI, Susceptibility-weighted imaging; TBI, Traumatic brain injury; Technetium-99, 99m-Tc; Thallium-201, 201Tl; TNF, Tumor necrosis factor; TRAIL, TNF-related apoptosis-inducing ligand; Turbo RFP, Turbo red fluorescent protein.

Address correspondence to: Dr. Michael C Veronesi, Department of Radiology and Imaging Sciences,

Indiana University School of Medicine, Research 2 Building (R2), Room E174, 950 W. Walnut Street, Indianapolis, IN 46202-5181, USA. Tel: 317-278-9848; E-mail: mverones@iu.edu

References

[1] Abbott NJ. Blood-brain barrier structure and function and the challenges for CNS drug delivery. J Inherit Metab Dis 2013; 36: 437-449.
[2] Pardridge WM. CSF, blood-brain barrier, and brain drug delivery. Expert Opin Drug Deliv 2016; 13: 963-975.
[3] Ganger S and Schindowski K. Tailoring formulations for intranasal nose-to-brain delivery: a review on architecture, physico-chemical characteristics and mucociliary clearance of the nasal olfactory mucosa. Pharmaceutics 2018; 10.
[4] Lochhead JJ and Thorne RG. Intranasal delivery of biologics to the central nervous system. Adv Drug Deliv Rev 2012; 64: 614-628.
[5] lochhead J and Thorne RG. Intranasal drug delivery to the brain. Drug delivery to the brain. New York: Springer; 2014. pp.401-431.
[6] Pardridge WM. Drug targeting to the brain. Pharm Res 2007; 24: 1733-1744.
[7] Gilmore JL, Yi X, Quan L and Kabanov AV. Novel nanomaterials for clinical neuroscience. J Neuroimmune Pharmacol 2008; 3: 83-94.
[8] Tosi G, Ruozi B and Belletti D. Nanomedicine: the future for advancing medicine and neuroscience. Nanomedicine (Lond) 2012; 7: 1113-1116.
[9] Clerico DM, To WC and Lanza DC. Anatomy of the human nasal passages. In: Doty RL, editor. Handbook of olfaction and gustation. 3rd edition. Hoboken, New Jersey: Wiley Blackwell; 2015. pp. xviii, 1217.
[10] Harkema JR. Comparative aspects of nasal airway anatomy: relevance to inhalation toxicology. Toxicol Pathol 1991; 19: 321-336.
[11] Ding X DA. Composition, enzymatic location and metabolish. In: Doty RL, editor. Handbook of olfaction and gustation. 3rd edition. Hoboken, New Jersey: Wiley Blackwell; 2015. pp. xviii, 1217.
[12] Ghadiri M, Young PM and Traini D. Strategies to enhance drug absorption via nasal and pulmonary routes. Pharmaceutics 2019; 11.
[13] Ross TM, Martinez PM, Renner JC, Thorne RG, Hanson LR and Frey WH 2nd. Intranasal administration of interferon beta bypasses the blood-brain barrier to target the central nervous system and cervical lymph nodes: a non-invasive treatment strategy for multiple sclerosis. J Neuroimmunol 2004; 151: 66-77.
[14] Thorne RG, Pronk GJ, Padmanabhan V and Frey WH 2nd. Delivery of insulin-like growth factor-I to the rat brain and spinal cord along olfactory and trigeminal pathways following intranasal administration. Neuroscience 2004; 127: 481-496.
[15] Lochhead JJ, Wolak DJ, Pizzo ME and Thorne RG. Rapid transport within cerebral perivascular spaces underlies widespread tracer distribution in the brain after intranasal administration. J Cereb Blood Flow Metab 2015; 35: 371-381.
[16] Thorne RG, Hanson LR, Ross TM, Tung D and Frey WH 2nd. Delivery of interferon-beta to the monkey nervous system following intranasal administration. Neuroscience 2008; 152: 785-797.
[17] Lochhead JJ, Kellohen KL, Ronaldson PT and Davis TP. Distribution of insulin in trigeminal nerve and brain after intranasal administration. Sci Rep 2019; 9: 2621.
[18] Illum L. Is nose-to-brain transport of drugs in man a reality? J Pharm Pharmacol 2004; 56: 3-17.
[19] Djupesland PG, Messina JC and Mahmoud RA. The nasal approach to delivering treatment for brain diseases: an anatomic, physiologic, and delivery technology overview. Ther Deliv 2014; 5: 709-733.
[20] Leopold DA, Hummel T, Schwob JE, Hong SC, Knecht M and Kobal G. Anterior distribution of human olfactory epithelium. Laryngoscope 2000; 110: 417-421.
[21] Balin BJ, Broadwell RD, Salcman M and el-Kalliny M. Avenues for entry of peripherally administered protein to the central nervous system in mouse, rat, and squirrel monkey. J Comp Neurol 1986; 251: 260-280.
[22] Fortuna A, Alves G, Serralheiro A, Sousa J and Falcao A. Intranasal delivery of systemic-acting drugs: small-molecules and biomacromolecules. Eur J Pharm Biopharm 2014; 88: 8-27.
[23] Erdő F, Bors LA, Farkas D, Bajza Á and Gizurarson S. Evaluation of intranasal delivery route of drug administration for brain targeting. Brain Research Bulletin 2018; 143: 155-170.
[24] Corrigan M, Wilson SS and Hampton J. Safety and efficacy of intranasally administered medications in the emergency department and prehospital settings. Am J Health Syst Pharm 2015; 72: 1544-1554.
[25] Chen W, Silverman DH, Delaloye S, Czernin J, Kamdar N, Pope W, Satyamurthy N, Schiepers C and Cloughesy T. 18F-FDOPA PET imaging of brain tumors: comparison study with 18F-FDG PET and evaluation of diagnostic accuracy. J Nucl Med 2006; 47: 904-911.
[26] Claxton A, Baker LD, Hanson A, Trittschuh EH, Cholerton B, Morgan A, Callaghan M, Arbuckle M, Behl C and Craft S. Long acting intranasal

insulin detemir improves cognition for adults with mild cognitive impairment or early-stage Alzheimer's disease dementia. J Alzheimers Dis 2015; 45: 1269-1270.
[27] Ostrom QT, Gittleman H, Xu J, Kromer C, Wolinsky Y, Kruchko C and Barnholtz-Sloan JS. CBTRUS statistical report: primary brain and other central nervous system tumors diagnosed in the united states in 2009-2013. Neuro Oncol 2016; 18: v1-v75.
[28] Kalia LV, Kalia SK and Lang AE. Disease-modifying strategies for Parkinson's disease. Mov Disord 2015; 30: 1442-1450.
[29] Lee SY, Lee AR, Hwangbo R, Han J, Hong M and Bahn GH. Is oxytocin application for autism spectrum disorder evidence-based? Exp Neurobiol 2015; 24: 312-324.
[30] Chien LN, Ostrom QT, Gittleman H, Lin JW, Sloan AE, Barnett GH, Elder JB, McPherson C, Warnick R, Chiang YH, Lin CM, Rogers LR, Chiou HY and Barnholtz-Sloan JS. International differences in treatment and clinical outcomes for high grade glioma. PLoS One 2015; 10: e0129602.
[31] Kromer C, Xu J, Ostrom QT, Gittleman H, Kruchko C, Sawaya R and Barnholtz-Sloan JS. Estimating the annual frequency of synchronous brain metastasis in the United States 2010-2013: a population-based study. J Neurooncol 2017; 134: 55-64.
[32] Ostrom QT, Gittleman H, Kruchko C and Barnholtz-Sloan JS. Primary brain and other central nervous system tumors in Appalachia: regional differences in incidence, mortality, and survival. J Neurooncol 2018; 142: 27-38.
[33] Ostrom QT, Gittleman H, Kruchko C, Louis DN, Brat DJ, Gilbert MR, Petkov VI and Barnholtz-Sloan JS. Completeness of required site-specific factors for brain and CNS tumors in the surveillance, epidemiology and end results (SEER) 18 database (2004-2012, varying). J Neurooncol 2016; 130: 31-42.
[34] Sabban EL, Alaluf LG and Serova LI. Potential of neuropeptide Y for preventing or treating post-traumatic stress disorder. Neuropeptides 2016; 56: 19-24.
[35] Chapman CD, Frey WH 2nd, Craft S, Danielyan L, Hallschmid M, Schioth HB and Benedict C. Intranasal treatment of central nervous system dysfunction in humans. Pharm Res 2013; 30: 2475-2484.
[36] Kim HJ, Shin WJ, Park S, Ahn HS and Oh JH. The sedative effects of the intranasal administration of dexmedetomidine in children undergoing surgeries compared to other sedation methods: a systematic review and meta-analysis. J Clin Anesth 2017; 38: 33-39.
[37] Lipton RB, McGinley JS, Shulman KJ, Wirth RJ and Buse DC. Faster improvement in migraine pain intensity and migraine-related disability at early time points with AVP-825 (sumatriptan nasal powder delivery system) versus oral sumatriptan: a comparative randomized clinical trial across multiple attacks from the COMPASS study. Headache 2017; 57: 1570-1582.
[38] Traynor K. Esketamine nasal spray approved for treatment-resistant depression. Am J Health Syst Pharm 2019; 76: 573.
[39] Benfield J and Musto A. Intranasal therapy to stop status epilepticus in prehospital settings. Drugs R D 2018; 18: 7-17.
[40] Sin B, Jeffrey I, Halpern Z, Adebayo A, Wing T, Lee AS, Ruiz J, Persaud K, Davenport L, de Souza S and Williams M. Intranasal sufentanil versus intravenous morphine for acute pain in the emergency department: a randomized pilot trial. J Emerg Med 2019; 56: 301-307.
[41] Rogriguez D, Urrutia G, Escobar Y, Moya J and Murillo M. Efficacy and safety of oral or nasal fentanyl for treatment of breakthrough pain in cancer patients: a systematic review. J Pain Palliat Care Pharmacother 2015; 29: 228-246.
[42] Ryan SA and Dunne RB. Pharmacokinetic properties of intranasal and injectable formulations of naloxone for community use: a systematic review. Pain Manag 2018; 8: 231-245.
[43] Webster LR, Pantaleon C, Shah MS, DiFalco R, Iverson M, Smith MD, Kinzler ER and Aigner S. A randomized, double-blind, double-dummy, placebo-controlled, intranasal drug liking study on a novel abuse-deterrent formulation of morphine-morphine ARER. Pain Med 2017; 18: 1303-1313.
[44] Webster LR, Iverson M, Pantaleon C, Smith MD, Kinzler ER and Aigner S. A randomized, double-blind, double-dummy, placebo-controlled, intranasal human abuse potential study of oxycodone ARIR, a novel, immediate-release, abuse-deterrent formulation. Pain Med 2019; 20: 747-757.
[45] Allison M and Hale C. A phase I study of the pharmacokinetics and pharmacodynamics of intranasal doxylamine in subjects with chronic intermittent sleep impairment. Drugs R D 2018; 18: 129-136.
[46] Pires A, Fortuna A, Alves G and Falcao A. Intranasal drug delivery: how, why and what for? J Pharm Pharm Sci 2009; 12: 288-311.
[47] Picone P, Sabatino MA, Ditta LA, Amato A, San Biagio PL, Mulè F, Giacomazza D, Dispenza C and Di Carlo M. Nose-to-brain delivery of insulin enhanced by a nanogel carrier. J Control Release 2018; 270: 23-36.
[48] Kumar A, Pandey AN and Jain SK. Nasal-nanotechnology: revolution for efficient therapeutics delivery. Drug Deliv 2016; 23: 681-693.

[49] King DF, McKay PF, Mann JF, Jones CB and Shattock RJ. Plasmid DNA vaccine co-immunisation modulates cellular and humoral immune responses induced by intranasal inoculation in mice. PLoS One 2015; 10: e0141557.
[50] Nyombayire J, Anzala O, Gazzard B, Karita E, Bergin P, Hayes P, Kopycinski J, Omosa-Manyonyi G, Jackson A, Bizimana J, Farah B, Sayeed E, Parks CL, Inoue M, Hironaka T, Hara H, Shu T, Matano T, Dally L, Barin B, Park H, Gilmour J, Lombardo A, Excler JL, Fast P, Laufer DS and Cox JH. First-in-human evaluation of the safety and immunogenicity of an intranasally administered replication-competent sendai virus-vectored HIV Type 1 Gag vaccine: induction of potent T-Cell or antibody responses in prime-boost regimens. J Infect Dis 2017; 215: 95-104.
[51] Kendrick KM, Guastella AJ and Becker B. Overview of human oxytocin research. Curr Top Behav Neurosci 2018; 35: 321-348.
[52] Jones C, Barrera I, Brothers S, Ring R and Wahlestedt C. Oxytocin and social functioning. Dialogues Clin Neurosci 2017; 19: 193-201.
[53] Moeini M, Omidi A, Sehat M and Banafshe HR. The effects of oxytocin on withdrawal, craving and stress response in heroin-dependent patients: a randomized, double-blind clinical trial. Eur Addict Res 2019; 25: 41-47.
[54] Fang A, Lawson EA and Wilhelm S. Intranasal oxytocin modulates higher order social cognition in body dysmorphic disorder. Depress Anxiety 2019; 36: 153-161.
[55] Russell J, Maguire S, Hunt GE, Kesby A, Suraev A, Stuart J, Booth J and McGregor IS. Intranasal oxytocin in the treatment of anorexia nervosa: randomized controlled trial during re-feeding. Psychoneuroendocrinology 2018; 87: 83-92.
[56] Kamei N, Shingaki T, Kanayama Y, Tanaka M, Zochi R, Hasegawa K, Watanabe Y and Takeda-Morishita M. Visualization and quantitative assessment of the brain distribution of insulin through nose-to-brain delivery based on the cell-penetrating peptide noncovalent strategy. Mol Pharm 2016; 13: 1004-1011.
[57] Kamei N, Okada N, Ikeda T, Choi H, Fujiwara Y, Okumura H and Takeda-Morishita M. Effective nose-to-brain delivery of exendin-4 via coadministration with cell-penetrating peptides for improving progressive cognitive dysfunction. Sci Rep 2018; 8: 17641.
[58] Appu AP, Arun P, Krishnan JKS, Moffett JR and Namboodiri AMA. Rapid intranasal delivery of chloramphenicol acetyltransferase in the active form to different brain regions as a model for enzyme therapy in the CNS. J Neurosci Methods 2016; 259: 129-134.
[59] Spencer D, Yu D, Morshed RA, Li G, Pituch KC, Gao DX, Bertolino N, Procissi D, Lesniak MS and Balyasnikova IV. Pharmacologic modulation of nasal epithelium augments neural stem cell targeting of glioblastoma. Theranostics 2019; 9: 2071-2083.
[60] Bonferoni MC, Rossi S, Sandri G, Ferrari F, Gavini E, Rassu G and Giunchedi P. Nanoemulsions for "nose-to-brain" drug delivery. Pharmaceutics 2019; 11: 84.
[61] Chavda VP. Chapter 4 - Nanobased nano drug delivery: a comprehensive review. In: Mohapatra SS, Ranjan S, Dasgupta N, Mishra RK, Thomas S, editors. Applications of Targeted Nano Drugs and Delivery Systems. Elsevier; 2019. pp. 69-92.
[62] Patra JK, Das G, Fraceto LF, Campos EVR, Rodriguez-Torres MDP, Acosta-Torres LS, Diaz-Torres LA, Grillo R, Swamy MK, Sharma S, Habtemariam S and Shin HS. Nano based drug delivery systems: recent developments and future prospects. J Nanobiotechnology 2018; 16: 71.
[63] de Oliveira Junior ER, Nascimento TL, Salomao MA, da Silva ACG, Valadares MC and Lima EM. Increased nose-to-brain delivery of melatonin mediated by polycaprolactone nanoparticles for the treatment of glioblastoma. Pharm Res 2019; 36: 131.
[64] Bobo D, Robinson KJ, Islam J, Thurecht KJ and Corrie SR. Nanoparticle-based medicines: a review of FDA-approved materials and clinical trials to date. Pharm Res 2016; 33: 2373-2387.
[65] Mohanraj VJ and Chen Y. Nanoparticles - a review. Trop J Pharm Res 2007; 5: 561-573.
[66] Mi P, Cabral H, Kokuryo D, Rafi M, Terada Y, Aoki I, Saga T, Takehiko I, Nishiyama N and Kataoka K. Gd-DTPA-loaded polymer-metal complex micelles with high relaxivity for MR cancer imaging. Biomaterials 2013; 34: 492-500.
[67] Zhang L, Chan JM, Gu FX, Rhee JW, Wang AZ, Radovic-Moreno AF, Alexis F, Langer R and Farokhzad OC. Self-assembled lipid--polymer hybrid nanoparticles: a robust drug delivery platform. ACS Nano 2008; 2: 1696-1702.
[68] Belhadj Z, Zhan C, Ying M, Wei X, Xie C, Yan Z and Lu W. Multifunctional targeted liposomal drug delivery for efficient glioblastoma treatment. Oncotarget 2017; 8: 66889-66900.
[69] Eatemadi A, Daraee H, Zarghami N, Yar HM and Akbarzadeh A. Nanofiber: synthesis and biomedical applications. Artif Cells Nanomed Biotechnol 2016; 44: 111-121.
[70] Borran AA, Aghanejad A, Farajollahi A, Barar J and Omidi Y. Gold nanoparticles for radiosensitizing and imaging of cancer cells. Radiation Physics and Chemistry 2018; 152: 137-144.
[71] Chatterjee B, Gorain B, Mohananaidu K, Sengupta P, Mandal UK and Choudhury H.

Targeted drug delivery to the brain via intranasal nanoemulsion: available proof of concept and existing challenges. Int J Pharm 2019; 565: 258-268.
[72] Colombo M, Figueiró F, de Fraga Dias A, Teixeira HF, Battastini AMO and Koester LS. Kaempferol-loaded mucoadhesive nanoemulsion for intranasal administration reduces glioma growth in vitro. Int J Pharm 2018; 543: 214-223.
[73] Galeano C, Qiu Z, Mishra A, Farnsworth SL, Hemmi JJ, Moreira A, Edenhoffer P and Hornsby PJ. The route by which intranasally delivered stem cells enter the central nervous system. Cell Transplant 2018; 27: 501-514.
[74] Li G, Bonamici N, Dey M, Lesniak MS and Balyasnikova IV. Intranasal delivery of stem cell-based therapies for the treatment of brain malignancies. Expert Opin Drug Deliv 2018; 15: 163-172.
[75] Danielyan L, Schafer R, von Ameln-Mayerhofer A, Bernhard F, Verleysdonk S, Buadze M, Lourhmati A, Klopfer T, Schaumann F, Schmid B, Koehle C, Proksch B, Weissert R, Reichardt HM, van den Brandt J, Buniatian GH, Schwab M, Gleiter CH and Frey WH 2nd. Therapeutic efficacy of intranasally delivered mesenchymal stem cells in a rat model of Parkinson disease. Rejuvenation Res 2011; 14: 3-16.
[76] Danielyan L, Beer-Hammer S, Stolzing A, Schafer R, Siegel G, Fabian C, Kahle P, Biedermann T, Lourhmati A, Buadze M, Novakovic A, Proksch B, Gleiter CH, Frey WH and Schwab M. Intranasal delivery of bone marrow-derived mesenchymal stem cells, macrophages, and microglia to the brain in mouse models of Alzheimer's and Parkinson's disease. Cell Transplant 2014; 23 Suppl 1: S123-139.
[77] Yu-Taeger L, Stricker-Shaver J, Arnold K, Bambynek-Dziuk P, Novati A, Singer E, Lourhmati A, Fabian C, Magg J, Riess O, Schwab M, Stolzing A, Danielyan L and Nguyen HHP. Intranasal administration of mesenchymal stem cells ameliorates the abnormal dopamine transmission system and inflammatory reaction in the R6/2 mouse model of huntington disease. Cells 2019; 8.
[78] Wei N, Yu SP, Gu X, Taylor TM, Song D, Liu XF and Wei L. Delayed intranasal delivery of hypoxic-preconditioned bone marrow mesenchymal stem cells enhanced cell homing and therapeutic benefits after ischemic stroke in mice. Cell Transplant 2013; 22: 977-991.
[79] Chau MJ, Deveau TC, Gu X, Kim YS, Xu Y, Yu SP and Wei L. Delayed and repeated intranasal delivery of bone marrow stromal cells increases regeneration and functional recovery after ischemic stroke in mice. BMC Neurosci 2018; 19: 20.
[80] van Velthoven CT, Kavelaars A, van Bel F and Heijnen CJ. Nasal administration of stem cells: a promising novel route to treat neonatal ischemic brain damage. Pediatr Res 2010; 68: 419-422.
[81] Wei ZZ, Gu X, Ferdinand A, Lee JH, Ji X, Ji XM, Yu SP and Wei L. Intranasal delivery of bone marrow mesenchymal stem cells improved neurovascular regeneration and rescued neuropsychiatric deficits after neonatal stroke in rats. Cell Transplant 2015; 24: 391-402.
[82] Reitz M, Demestre M, Sedlacik J, Meissner H, Fiehler J, Kim SU, Westphal M and Schmidt NO. Intranasal delivery of neural stem/progenitor cells: a noninvasive passage to target intracerebral glioma. Stem Cells Transl Med 2012; 1: 866-873.
[83] Balyasnikova IV, Prasol MS, Ferguson SD, Han Y, Ahmed AU, Gutova M, Tobias AL, Mustafi D, Rincon E, Zhang L, Aboody KS and Lesniak MS. Intranasal delivery of mesenchymal stem cells significantly extends survival of irradiated mice with experimental brain tumors. Mol Ther 2014; 22: 140-148.
[84] Soria B, Martin-Montalvo A, Aguilera Y, Mellado-Damas N, Lopez-Beas J, Herrera-Herrera I, Lopez E, Barcia JA, Alvarez-Dolado M, Hmadcha A and Capilla-Gonzalez V. Human mesenchymal stem cells prevent neurological complications of radiotherapy. Front Cell Neurosci 2019; 13: 204.
[85] Dey M, Yu D, Kanojia D, Li G, Sukhanova M, Spencer DA, Pituch KC, Zhang L, Han Y, Ahmed AU, Aboody KS, Lesniak MS and Balyasnikova IV. Intranasal oncolytic virotherapy with CXCR4-Enhanced stem cells extends survival in mouse model of glioma. Stem Cell Reports 2016; 7: 471-482.
[86] Ding H, Wu F and Nair MP. Image-guided drug delivery to the brain using nanotechnology. Drug Discov Today 2013; 18: 1074-1080.
[87] Yordanova A, Eppard E, Kurpig S, Bundschuh RA, Schonberger S, Gonzalez-Carmona M, Feldmann G, Ahmadzadehfar H and Essler M. Theranostics in nuclear medicine practice. Onco Targets Ther 2017; 10: 4821-4828.
[88] Lee DY and Li KC. Molecular theranostics: a primer for the imaging professional. AJR Am J Roentgenol 2011; 197: 318-324.
[89] Nguyen QT, Lee EJ, Huang MG, Park YI, Khullar A and Plodkowski RA. Diagnosis and treatment of patients with thyroid cancer. Am Health Drug Benefits 2015; 8: 30-40.
[90] Sukumar UK, Bose RJC, Malhotra M, Babikir HA, Afjei R, Robinson E, Zeng Y, Chang E, Habte F, Sinclair R, Gambhir SS, Massoud TF and Paulmurugan R. Intranasal delivery of targeted

polyfunctional gold-iron oxide nanoparticles loaded with therapeutic microRNAs for combined theranostic multimodality imaging and presensitization of glioblastoma to temozolomide. Biomaterials 2019; 218: 119342.
[91] Radue EW, Weigel M, Wiest R and Urbach H. Introduction to magnetic resonance imaging for neurologists. Continuum (Minneap Minn) 2016; 22: 1379-1398.
[92] Bushberg JT, Seibert JA, Leidholdt EM and Boone JM. The essential physics of medical imaging. Wolters Kluwer Health 2011.
[93] Hendrick RE and Haacke MM. Basic physics of MR contrast agents and maxmization of image contrast. J Magn Reson Imaging 1993; 3: 137-148.
[94] Okuhata Y. Delivery of diagnostic agents for magnetic resonance imaging. Adv Drug Deliv Rev 1999; 37: 121-137.
[95] Zhang Q, Zhu W, Xu F, Dai X, Shi L, Cai W, Mu H, Hitchens TK, Foley LM, Liu X, Yu F, Chen J, Shi Y, Leak RK, Gao Y, Chen J and Hu X. The interleukin-4/PPARgamma signaling axis promotes oligodendrocyte differentiation and remyelination after brain injury. PLoS Biol 2019; 17: e3000330.
[96] Sragovich S, Malishkevich A, Piontkewitz Y, Giladi E, Touloumi O, Lagoudaki R, Grigoriadis N and Gozes I. The autism/neuroprotection-linked ADNP/NAP regulate the excitatory glutamatergic synapse. Transl Psychiatry 2019; 9: 2.
[97] Levy Barazany H, Barazany D, Puckett L, Blanga-Kanfi S, Borenstein-Auerbach N, Yang K, Peron JP, Weiner HL and Frenkel D. Brain MRI of nasal MOG therapeutic effect in relapsing-progressive EAE. Exp Neurol 2014; 255: 63-70.
[98] Yadav S, Pawar G, Kulkarni P, Ferris C and Amiji M. CNS delivery and anti-inflammatory effects of intranasally administered cyclosporine-A in cationic nanoformulations. J Pharmacol Exp Ther 2019; 370: 843-854.
[99] Chen Y, Fan H, Xu C, Hu W and Yu B. Efficient cholera toxin B Subunit-Based nanoparticles with MRI capability for drug delivery to the brain following intranasal administration. Macromol Biosci 2019; 19: e1900017.
[100] Brabazon F, Wilson CM, Jaiswal S, Reed J, Frey WH Nd and Byrnes KR. Intranasal insulin treatment of an experimental model of moderate traumatic brain injury. J Cereb Blood Flow Metab 2017; 37: 3203-3218.
[101] Das M, Wang C, Bedi R, Mohapatra SS and Mohapatra S. Magnetic micelles for DNA delivery to rat brains after mild traumatic brain injury. Nanomedicine 2014; 10: 1539-1548.
[102] Santiago JCP and Hallschmid M. Outcomes and clinical implications of intranasal insulin administration to the central nervous system. Exp Neurol 2019; 317: 180-190.
[103] Ding C, Leow MK and Magkos F. Oxytocin in metabolic homeostasis: implications for obesity and diabetes management. Obes Rev 2019; 20: 22-40.
[104] De Cagna F, Fusar-Poli L, Damiani S, Rocchetti M, Giovanna G, Mori A, Politi P and Brondino N. The role of intranasal oxytocin in anxiety and depressive disorders: a systematic review of randomized controlled trials. Clin Psychopharmacol Neurosci 2019; 17: 1-11.
[105] Horta M, Kaylor K, Feifel D and Ebner NC. Chronic oxytocin administration as a tool for investigation and treatment: a cross-disciplinary systematic review. Neurosci Biobehav Rev 2019; 108: 1-23.
[106] Craft S, Claxton A, Baker LD, Hanson AJ, Cholerton B, Trittschuh EH, Dahl D, Caulder E, Neth B, Montine TJ, Jung Y, Maldjian J, Whitlow C and Friedman S. Effects of regular and long-acting insulin on cognition and Alzheimer's disease biomarkers: a pilot clinical trial. J Alzheimers Dis 2017; 57: 1325-1334.
[107] Kullmann S, Heni M, Veit R, Scheffler K, Machann J, Haring HU, Fritsche A and Preissl H. Selective insulin resistance in homeostatic and cognitive control brain areas in overweight and obese adults. Diabetes Care 2015; 38: 1044-1050.
[108] Wingrove J, Swedrowska M, Scherließ R, Parry M, Ramjeeawon M, Taylor D, Gauthier G, Brown L, Amiel S, Zelaya F and Forbes B. Characterisation of nasal devices for delivery of insulin to the brain and evaluation in humans using functional magnetic resonance imaging. J Control Release 2019; 302: 140-147.
[109] Kumar J, Völlm B and Palaniyappan L. Oxytocin affects the connectivity of the precuneus and the amygdala: a randomized, double-blinded, placebo-controlled neuroimaging trial. Int J Neuropsychopharmacol 2014; 18.
[110] Grace SA, Labuschagne I, Castle DJ and Rossell SL. Intranasal oxytocin alters amygdala-temporal resting-state functional connectivity in body dysmorphic disorder: a double-blind placebo-controlled randomized trial. Psychoneuroendocrinology 2019; 107: 179-186.
[111] da Fonseca CO, Linden R, Futuro D, Gattass CR and Quirico-Santos T. Ras pathway activation in gliomas: a strategic target for intranasal administration of perillyl alcohol. Arch Immunol Ther Exp (Warsz) 2008; 56: 267-276.
[112] Jones T. The imaging science of positron emission tomography. Eur J Nucl Med 1996; 23: 807-813.
[113] Bushberg JT, Seibert JA, Boone JM and Leidholdt EM. The essential physics of medical imaging. Williams & Wilkins 2012.

[114] Vasdev N and Alavi A. Novel PET radiotracers with potential clinical applications. PET Clin 2017; 12: xi-xii.
[115] Jones T and Townsend D. History and future technical innovation in positron emission tomography. J Med Imaging (Bellingham) 2017; 4: 011013.
[116] Vaquero JJ and Kinahan P. Positron emission tomography: current challenges and opportunities for technological advances in clinical and preclinical imaging systems. Annu Rev Biomed Eng 2015; 17: 385-414.
[117] Nievelstein RA, Quarles van Ufford HM, Kwee TC, Bierings MB, Ludwig I, Beek FJ, de Klerk JM, Mali WP, de Bruin PW and Geleijns J. Radiation exposure and mortality risk from CT and PET imaging of patients with malignant lymphoma. Eur Radiol 2012; 22: 1946-1954.
[118] Zhu A, Lee D and Shim H. Metabolic positron emission tomography imaging in cancer detection and therapy response. Semin Oncol 2011; 38: 55-69.
[119] Couvineau A, Voisin T, Nicole P, Gratio V, Abad C and Tan YV. Orexins as novel therapeutic targets in inflammatory and neurodegenerative diseases. Front Endocrinol (Lausanne) 2019; 10: 709.
[120] Dhuria SV, Hanson LR and Frey WH 2nd. Intranasal drug targeting of hypocretin-1 (orexin-A) to the central nervous system. J Pharm Sci 2009; 98: 2501-2515.
[121] Van de Bittner GC, Van de Bittner KC, Wey HY, Rowe W, Dharanipragada R, Ying X, Hurst W, Giovanni A, Alving K, Gupta A, Hoekman J and Hooker JM. Positron emission tomography assessment of the intranasal delivery route for orexin A. ACS Chem Neurosci 2018; 9: 358-368.
[122] Yuki Y, Nochi T, Harada N, Katakai Y, Shibata H, Mejima M, Kohda T, Tokuhara D, Kurokawa S, Takahashi Y, Ono F, Kozaki S, Terao K, Tsukada H and Kiyono H. In vivo molecular imaging analysis of a nasal vaccine that induces protective immunity against botulism in nonhuman primates. J Immunol 2010; 185: 5436-5443.
[123] Shingaki T, Katayama Y, Nakaoka T, Irie S, Onoe K, Okauchi T, Hayashinaka E, Yamaguchi M, Tanki N, Ose T, Hayashi T, Wada Y, Furubayashi T, Cui Y, Sakane T and Watanabe Y. Visualization of drug translocation in the nasal cavity and pharmacokinetic analysis on nasal drug absorption using positron emission tomography in the rat. Eur J Pharm Biopharm 2016; 99: 45-53.
[124] Singh N, Veronese M, O'Doherty J, Sementa T, Bongarzone S, Cash D, Simmons C, Arcolin M, Marsden PK, Gee A and Turkheimer FE. Assessing the feasibility of intranasal radiotracer administration for in brain PET imaging. Nucl Med Biol 2018; 66: 32-39.
[125] Craft S, Baker LD, Montine TJ, Minoshima S, Watson GS, Claxton A, Arbuckle M, Callaghan M, Tsai E, Plymate SR, Green PS, Leverenz J, Cross D and Gerton B. Intranasal insulin therapy for Alzheimer disease and amnestic mild cognitive impairment: a pilot clinical trial. Arch Neurol 2012; 69: 29-38.
[126] Mottolese R, Redoute J, Costes N, Le Bars D and Sirigu A. Switching brain serotonin with oxytocin. Proc Natl Acad Sci U S A 2014; 111: 8637-8642.
[127] White ND. Increasing Naloxone access and use to prevent opioid overdose death and disability. Am J Lifestyle Med 2019; 13: 33-35.
[128] Johansson J, Hirvonen J, Lovro Z, Ekblad L, Kaasinen V, Rajasilta O, Helin S, Tuisku J, Siren S, Pennanen M, Agrawal A, Crystal R, Vainio PJ, Alho H and Scheinin M. Intranasal naloxone rapidly occupies brain mu-opioid receptors in human subjects. Neuropsychopharmacology 2019; 44: 1667-1673.
[129] Spencer CM, Gunasekara NS and Hills C. Zolmitriptan: a review of its use in migraine. Drugs 1999; 58: 347-374.
[130] Tepper SJ, Chen S, Reidenbach F and Rapoport AM. Intranasal zolmitriptan for the treatment of acute migraine. Headache 2013; 53 Suppl 2: 62-71.
[131] Yates R, Sorensen J, Bergstrom M, Antoni G, Nairn K, Kemp J, Langstrom B and Dane A. Distribution of intranasal C-zolmitriptan assessed by positron emission tomography. Cephalalgia 2005; 25: 1103-1109.
[132] Kwok PCL, Wallin M, Dolovich MB and Chan HK. Studies of radioaerosol deposition in the respiratory tract. Semin Nucl Med 2019; 49: 62-70.
[133] Esposito E, Boschi A, Ravani L, Cortesi R, Drechsler M, Mariani P, Moscatelli S, Contado C, Di Domenico G, Nastruzzi C, Giganti M and Uccelli L. Biodistribution of nanostructured lipid carriers: a tomographic study. Eur J Pharm Biopharm 2015; 89: 145-156.
[134] Mandlik SK, Ranpise NS, Mohanty BS and Chaudhari PR. A coupled bimodal SPECT-CT imaging and brain kinetics studies of zolmitriptan-encapsulated nanostructured polymeric carriers. Drug Deliv Transl Res 2018; 8: 797-805.
[135] Shiga H, Taki J, Yamada M, Washiyama K, Amano R, Matsuura Y, Matsui O, Tatsutomi S, Yagi S, Tsuchida A, Yoshizaki T, Furukawa M, Kinuya S and Miwa T. Evaluation of the olfactory nerve transport function by SPECT-MRI fusion image with nasal thallium-201 administration. Mol Imaging Biol 2011; 13: 1262-1266.

[136] Shiga H, Taki J, Washiyama K, Yamamoto J, Kinase S, Okuda K, Kinuya S, Watanabe N, Tonami H, Koshida K, Amano R, Furukawa M and Miwa T. Assessment of olfactory nerve by SPECT-MRI image with nasal thallium-201 administration in patients with olfactory impairments in comparison to healthy volunteers. PLoS One 2013; 8: e57671.
[137] Jafarieh O, Md S, Ali M, Baboota S, Sahni JK, Kumari B, Bhatnagar A and Ali J. Design, characterization, and evaluation of intranasal delivery of ropinirole-loaded mucoadhesive nanoparticles for brain targeting. Drug Dev Ind Pharm 2015; 41: 1674-1681.
[138] Sharma D, Maheshwari D, Philip G, Rana R, Bhatia S, Singh M, Gabrani R, Sharma SK, Ali J, Sharma RK and Dang S. Formulation and optimization of polymeric nanoparticles for intranasal delivery of lorazepam using Box-Behnken design: in vitro and in vivo evaluation. Biomed Res Int 2014; 2014: 156010.
[139] Patel S, Chavhan S, Soni H, Babbar AK, Mathur R, Mishra AK and Sawant K. Brain targeting of risperidone-loaded solid lipid nanoparticles by intranasal route. J Drug Target 2011; 19: 468-474.
[140] Kakkar V, Mishra AK, Chuttani K and Kaur IP. Proof of concept studies to confirm the delivery of curcumin loaded solid lipid nanoparticles (C-SLNs) to brain. Int J Pharm 2013; 448: 354-359.
[141] Casettari L and Illum L. Chitosan in nasal delivery systems for therapeutic drugs. J Control Release 2014; 190: 189-200.
[142] Djupesland PG, Messina JC and Mahmoud RA. Breath powered nasal delivery: a new route to rapid headache relief. Headache 2013; 53 Suppl 2: 72-84.
[143] Earnest FT, Baker HL Jr, Kispert DB and Laws ER Jr. Magnetic resonance imaging vs. computed tomography: advantages and disadvantages. Clin Neurosurg 1985; 32: 540-573.
[144] Goldman LW. Principles of CT and CT technology. J Nucl Med Technol 2007; 35: 115-128; quiz 129-130.
[145] Srikala Narayanan WAKAaST. In: Elsevier I, editor. Zitelli and Davis' Atlas of Pediatric Physical Diagnosis. 2018. pp. 916-990.
[146] De Backer JW, Vos WG, Burnell P, Verhulst SL, Salmon P, De Clerck N and De Backer W. Study of the variability in upper and lower airway morphology in Sprague-Dawley rats using modern micro-CT scan-based segmentation techniques. Anat Rec (Hoboken) 2009; 292: 720-727.
[147] Casteleyn C, Cornillie P, Hermens A, Van Loo D, Van Hoorebeke L, van den Broeck W and Simoens P. Topography of the rabbit paranasal sinuses as a prerequisite to model human sinusitis. Rhinology 2010; 48: 300-304.
[148] Warnken ZN, Smyth HDC, Davis DA, Weitman S, Kuhn JG and Williams RO 3rd. Personalized medicine in nasal delivery: the use of patient-specific administration parameters to improve nasal drug targeting using 3D-printed nasal replica casts. Mol Pharm 2018; 15: 1392-1402.
[149] Frank DO, Kimbell JS, Cannon D and Rhee JS. Computed intranasal spray penetration: comparisons before and after nasal surgery. Int Forum Allergy Rhinol 2013; 3: 48-55.
[150] Engelhardt L, Rohm M, Mavoungou C, Schindowski K, Schafmeister A and Simon U. First steps to develop and validate a CFPD model in order to support the design of nose-to-brain delivered biopharmaceuticals. Pharm Res 2016; 33: 1337-1350.
[151] Shang Y, Inthavong K and Tu J. Development of a computational fluid dynamics model for mucociliary clearance in the nasal cavity. J Biomech 2019; 85: 74-83.
[152] Carvalho LA, Teng J, Fleming RL, Tabet EI, Zinter M, de Melo Reis RA and Tannous BA. Olfactory ensheathing cells: a trojan horse for glioma gene therapy. J Natl Cancer Inst 2019; 111: 283-291.
[153] Ji G, Liu M, Zhao XF, Liu XY, Guo QL, Guan ZF, Zhou HG and Guo JC. NF-kappaB signaling is involved in the effects of intranasally engrafted human neural stem cells on neurofunctional improvements in neonatal rat hypoxic-ischemic encephalopathy. CNS Neurosci Ther 2015; 21: 926-935.
[154] Thompson JM and Miller LS. Preclinical optical imaging to study pathogenesis, novel therapeutics and diagnostics against orthopaedic infection. J Orthop Res 2019; 37: 2269-2277.
[155] Yan Y, Shi P, Song W and Bi S. Chemiluminescence and bioluminescence imaging for biosensing and therapy: in vitro and in vivo perspectives. Theranostics 2019; 9: 4047-4065.
[156] Tai PA, Liu YL, Wen YT, Lin CM, Huynh TT, Hsiao M, Wu ATH and Wei L. The development and applications of a dual optical imaging system for studying glioma stem cells. Mol Imaging 2019; 18: 1536012119870899.
[157] Gil CJ, Tomov ML, Theus AS, Cetnar A, Mahmoudi M and Serpooshan V. In vivo tracking of tissue engineered constructs. Micromachines 2019; 10: 474.
[158] Yeh HW, Karmach O, Ji A, Carter D, Martins-Green MM and Ai HW. Red-shifted luciferase-luciferin pairs for enhanced bioluminescence imaging. Nat Methods 2017; 14: 971-974.
[159] England CG, Ehlerding EB and Cai W. NanoLuc: a small luciferase is brightening up the field of

bioluminescence. Bioconjug Chem 2016; 27: 1175-1187.
[160] Bagheri-Mohammadi S, Alani B, Karimian M, Moradian-Tehrani R and Noureddini M. Intranasal administration of endometrial mesenchymal stem cells as a suitable approach for Parkinson's disease therapy. Mol Biol Rep 2019; 46: 4293-4302.
[161] Chou LY and Chan WC. Fluorescence-tagged gold nanoparticles for rapidly characterizing the size-dependent biodistribution in tumor models. Adv Healthc Mater 2012; 1: 714-721.
[162] Zhang Y, Yu J, Kahkoska AR and Gu Z. Photoacoustic drug delivery. Sensors (Basel) 2017; 17.
[163] Xu M and Wang L. Photoacoustic imaging in biomedicine. Rev Sci Instrum 2006; 77.
[164] Wang D, Wu Y and Xia J. Review on photoacoustic imaging of the brain using nanoprobes. Neurophotonics 2016; 3: 010901.
[165] Huang L, Ao L, Hu D, Wang W, Sheng Z and Su W. Magneto-plasmonic nanocapsules for multimodal-imaging and magnetically guided combination cancer therapy. Chem Mater 2016; 28: 5896-5904.
[166] Chen H, Chen CC, Acosta C, Wu SY, Sun T and Konofagou EE. A new brain drug delivery strategy: focused ultrasound-enhanced intranasal drug delivery. PLoS One 2014; 9: e108880.
[167] Ye D, Zhang X, Yue Y, Raliya R, Biswas P, Taylor S, Tai YC, Rubin JB, Liu Y and Chen H. Focused ultrasound combined with microbubble-mediated intranasal delivery of gold nanoclusters to the brain. J Control Release 2018; 286: 145-153.

B. CONTROLLED RELEASE SOCIETY (CRS) ANNUAL MEETING AND EXPOSITION ABSTRACT

Controlled Release Society (CRS) Annual Meeting and Exposition, June 27 – July 1 in Las Vegas, NV

Title: CD133+ stem cells targetable dual drug polymer nanocarriers for treatment of glioblastoma

Presenting Author: Shelby Smiley, Indiana University-Purdue University Indianapolis, United States

Co-Authors: Yeonhee Yun, Indiana University School of Medicine, United States; Mosa Alhamami, Indiana University School of Medicine, United States; Pranav Ayagari, Indiana University-Purdue University Indianapolis, United States; Karen Pollok, Indiana University Simon Cancer Center, United States; Sudip Das, Butler University, United States; Michael W. Vannier, University of Chicago Hospitals, United States; Michael C. Veronesi, Indiana University School of Medicine, United States

Introduction: Glioblastoma (GBM) is a lethal brain tumor with a poor prognosis. GBM inevitably recurs in part due to cancer-derived stem cells (CSC) resistant to temozolomide (TMZ), which is the drug of choice for first-line therapy, and radiation therapy. CSCs regenerate rapidly and overexpress a methyltransferase which overrides the DNA alkylating mechanism of TMZ, leading to drug resistance. Multifunctional nanosystems can both target tumor and transport combination therapies to the tumor bed. Idasanutlin (RG7388, RO5503781) is a potent, selective small molecule and MDM2 antagonist that synergistically kills GBM cells when combined with TMZ (1). We developed a multifunctional hybrid polymer micellar nanoparticle containing TMZ and RG7388 that could target the CD133 antigen expressed on the surface of a GBM CSC subpopulation through covalent bonding of an aptamer derived based on the functional site of CD133 antibody (2).

Methods: A nanoparticle encapsulating both TMZ and RG7388 comprised of poly(lactide-*co*-glycolide) (PLGA) and polystyrene-*b*-polyethylene oxide (PS-*b*-PEO) using a modified double emulsification solvent evaporation method. PLGA and PS-*b*-PEO were combined to form a polymer micellar nanoparticle for size reduction (3). An ester-PLGA conjugate was used to permit covalent bonding of a CD133 aptamer. Size, surface charge, drug-loading efficiency and morphology were characterized in vitro using dynamic light scattering, UV-Vis spectroscopy and transmission electron microscopy. Human-derived cancer stem cells were grown in culture and were treated with TMZ and RG7388 or nanoparticles containing both compounds.

Results: The mean size of the TMZ + RG7388-loaded nanoparticles was 88 nm with a polydispersity index of 0.15. The mean nanoparticle charge was -9 mV with spherical morphology. Encapsulation efficiency of 14% for nanoparticles loaded with TMZ only was higher than the traditionally reported 2% in the literature. Preliminary conjugation efficiency studies revealed a 96% aptamer binding confirmed by fluorescent analysis. TMZ and RG7388 achieved 50% cell killing at 268 µM and 12 µM, respectively. Preliminary studies of CSCs treated with TMZ and RG7388 nanoparticles seem to produce a dose response curve. Studies of combination therapy with and without NPs and aptamer are ongoing.

Conclusion: A multifunctional nanosystem containing two potent chemotherapeutic drugs targeted to the GBM stem cell subpopulation with a CD133 aptamer was synthesized and evaluated in vitro.

Learning Objectives:

- Understand the need for novel therapies for the treatment of glioblastoma
- Differentiate the principles behind single and double emulsion techniques and when they should be applied
- Discuss the various measurement techniques utilized in developing a multi-functional nanocarrier

Key Words:

- Route/target of delivery – Tumor/cancer
- Type of delivery agent – Small molecule
- Delivery vehicle – Nanoparticle/nanomaterial
- Delivery vehicle – Targeted

Acknowledgements: This work was supported from the Biomedical Research Grant from the Indiana University School of Medicine and the Radiological Society of North America.

References: (1) Wang H, et al. J Neurosurg. 2017:446-459. (2) Shigdar S, et al. Cancer Lett. 2013: 84-95. (3) Nabar GM, et al. Int J Nanomedicine. 2018: 351-366.

Presenter biography: The presenting author is a current graduate student studying biomedical engineering at Indiana University-Purdue University Indianapolis. She has her bachelor's degree in chemistry and is completing her thesis on the development of novel, multifunctional nanoparticles for the treatment of glioblastoma.

Figures:

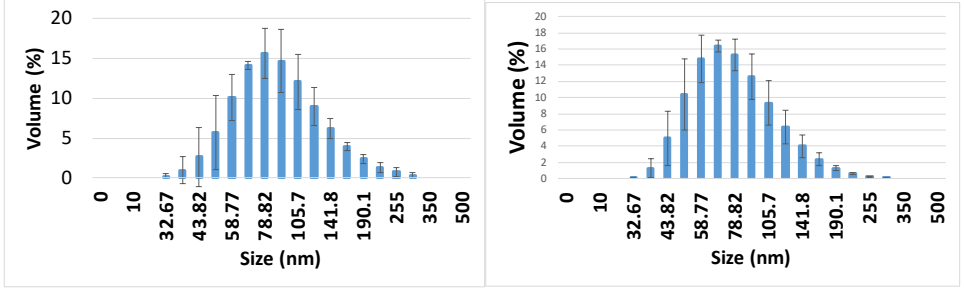

Figure 1: Representative dynamic light scattering measurement of the hydrodynamic distributions of TMZ-loaded nanoparticles (**left**), and TMZ+RG7388 nanoparticles (**right**).

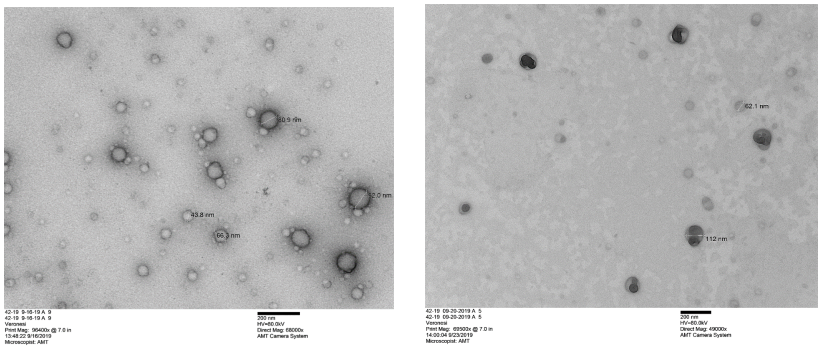

Figure 2: Representative morphology by transmission electron microscopy of TMZ-loaded nanoparticles (**left**), and TMZ+RG7388 nanoparticles (**right**).

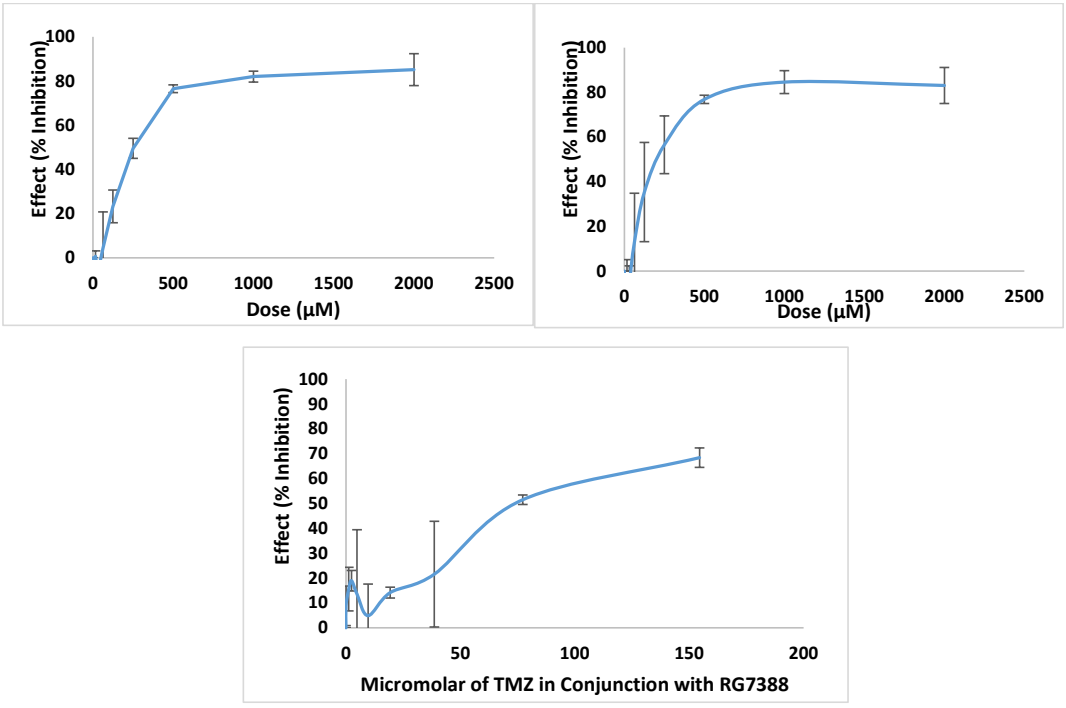

Figure 3: Cytotoxicity tests in GBM cancer stem cells with TMZ treatment (**top left**), RG7388 treatment (**top right**), and TMZ+RG7388-loaded nanoparticle treatment (**bottom**).